

AD-A198 155

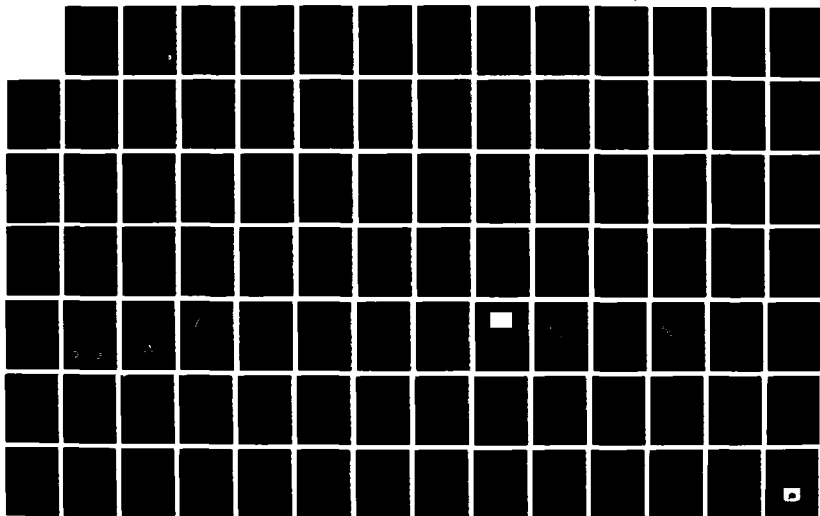
OPENING SWITCH RESEARCH ON A PLASMA FOCUS VI(U)  
ILLINOIS UNIV AT URBANA DEPT OF NUCLEAR ENGINEERING  
8 A GERDIN 26 FEB 88 AFOSR-TR-88-0938 AFOSR-86-0383

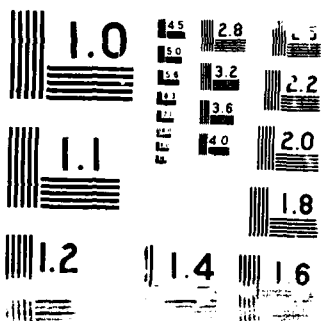
1/2

UNCLASSIFIED

F/G 20/8

NL





UNCLASSIFIED

DTIC FILE COPY

2

SECURITY CLASSIFICATION OF THIS PAGE

## REPORT DOCUMENTATION PAGE

1a. REPORT SECURITY CLASSIFICATION		1b. RESTRICTIVE MARKINGS													
2a. SECURITY CLASSIFICATION AUTHORITY Unclassified		3. DISTRIBUTION/AVAILABILITY OF REPORT Approved for public release; distribution unlimited													
LE		5. MONITORING ORGANIZATION REPORT NUMBER(S) <b>AFOSR-TR. 88-0930</b>													
R(S)		7a. NAME OF MONITORING ORGANIZATION AFOSR/NP													
1. OFFICE SYMBOL (If applicable) University of Illinois		7b. ADDRESS (City, State and ZIP Code) Bldg 410 Bolling AFB DC 20332-6448													
6c. ADDRESS (City, State and ZIP Code) Department of Nuclear Engineering 214 Nuclear Engineering Lab Urbana, IL 61801		9. PROCUREMENT INSTRUMENT IDENTIFICATION NUMBER AFOSR-86-0303													
8a. NAME OF FUNDING/SPONSORING ORGANIZATION AFOSR		8b. OFFICE SYMBOL (If applicable) NP													
8c. ADDRESS (City, State and ZIP Code) Bldg 410 Bolling AFB DC 20332-6448		10. SOURCE OF FUNDING NOS. <table border="1"><tr><td>PROGRAM ELEMENT NO.</td><td>PROJECT NO.</td><td>TASK NO.</td><td>WORK UNIT NO.</td></tr><tr><td>61102F</td><td>2301</td><td>A7</td><td></td></tr></table>		PROGRAM ELEMENT NO.	PROJECT NO.	TASK NO.	WORK UNIT NO.	61102F	2301	A7					
PROGRAM ELEMENT NO.	PROJECT NO.	TASK NO.	WORK UNIT NO.												
61102F	2301	A7													
11. TITLE (Include Security Classification) OPENING SWITCH RESEARCH ON A PLASMA FOCUS VI															
12. PERSONAL AUTHOR(S) Glenn A. Gerdin															
13a. TYPE OF REPORT Final		15. PAGE COUNT 149													
13b. TIME COVERED FROM 9/30/86 TO 9/29/87		14. DATE OF REPORT (Yr., Mo., Day) 2/26/88													
16. SUPPLEMENTARY NOTATION															
17. COSATI CODES <table border="1"><tr><td>FIELD</td><td>GROUP</td><td>SUB. GR.</td></tr><tr><td></td><td></td><td></td></tr><tr><td></td><td></td><td></td></tr><tr><td></td><td></td><td></td></tr></table>		FIELD	GROUP	SUB. GR.										18. SUBJECT TERMS (Continue on reverse if necessary and identify by block number) Dense Plasma Focus) Opening Switch Research, Soft X-ray Spectroscopy, Production of Soft X-rays, (sign) Laser Interferometry, A	
FIELD	GROUP	SUB. GR.													
19. ABSTRACT (Continue on reverse if necessary and identify by block number)  See Other Side															
20. DISTRIBUTION/AVAILABILITY OF ABSTRACT UNCLASSIFIED/UNLIMITED <input checked="" type="checkbox"/> SAME AS RPT. <input checked="" type="checkbox"/> DTIC USERS <input type="checkbox"/>		21. ABSTRACT SECURITY CLASSIFICATION Unclassified													
22a. NAME OF RESPONSIBLE INDIVIDUAL Lt Col Bruce Smith		22b. TELEPHONE NUMBER (Include Area Code) 202-767-4908													
		22c. OFFICE SYMBOL NP													

DD FORM 1473, 83 APR

EDITION OF 1 JAN 73 IS OBSOLETE.

UNCLASSIFIED

SECURITY CLASSIFICATION OF THIS PAGE

The utility of the plasma focus as an opening switch was analyzed on the basis of our previous experimental observations and those on other Mather-type devices. A load resistor has recently been included in the opening switch circuit model and the analysis indicates that the typical pinch resistances measured ( $60.1\Omega$ )<sup>6hm</sup> are too small to drive typical load resistances encountered in pulsed power ( $21\Omega$ ) in terms of % energy transferred (<2%) and the time required for the transfer ( $200\text{ns}$ )<sup>70r</sup>. A scaling law for pinch stability has been derived, which is consistent with our data and that from several other experimental devices; this model predicts that a plasma focus could be designed to permit longer energy transfer times by increasing the anode radius.

As to the progress of the two students supported by the contract, Mr. Frank Venneri, has successfully built and operated a curved-crystal soft-Xray spectrometer and he is in the process of writing his Ph.D. thesis. Mr. Kevin Boulais completed the requirements for the Masters of Science degree in electrical engineering. Mr. Boulais' thesis on laser interferometry of the pinch phase along with Mr. Venneri's spectrometer finally gave us a set of state-of-the-art diagnostics with which to study the plasma physics of the plasma focus. The results of these studies are being prepared for publication.

11-05-72

AFOSR-TR- 88 - 0930

Final Report

30 Sept. 1986 to 29 Sept. 1987

Opening Switch Research on a Plasma Focus UT

~~THE PLASMA FOCUS AS AN OPENING SWITCH VI~~

Glenn A. Gerdin\*

Fusion Studies Laboratory  
Dept. of Nuclear Engineering  
University of Illinois  
Urbana-Champaign Campus  
103 South Goodwin Avenue  
Urbana, Illinois 61801

Accession For	
NTIS GRA&I	<input checked="checked" type="checkbox"/>
DTIC TAB	<input type="checkbox"/>
Unannounced	<input type="checkbox"/>
Justification	
By _____	
Distribution/	
Availability Codes	
Dist	Avail and/or Special
A-1	

\*Present Address  
Dept. of Electrical and Computer Engineering  
Old Dominion University  
Norfolk, VA 23529-0246



#### A. Abstract

The utility of the plasma focus as an opening switch was analyzed on the basis of our previous experimental observations and those on other Mather-type devices. A load resistor has recently been included in the opening switch circuit model and the analysis indicates that the typical pinch resistances measured ( $\sim 0.1\Omega$ ) are too small to drive typical load resistances encountered in pulsed power ( $\sim 1\Omega$ ) in terms of % energy transferred ( $< 2\%$ ) and the time required for the transfer ( $> 200\text{ns}$ ). A scaling law for pinch stability has been derived, which is consistent with our data and that from several other experimental devices; this model predicts that a plasma focus could be designed to permit longer energy transfer times by increasing the anode radius.

As to the progress of the two students supported by the contract, Mr. Frank Venneri, has successfully built and operated a curved-crystal soft-Xray spectrometer and he is in the process of writing his Ph.D. thesis. Mr. Kevin Boulais completed the requirements for the Masters of Science degree in electrical engineering. Mr. Boulais' thesis on laser interferometry of the pinch phase along with Mr. Venneri's spectrometer finally gave us a set of state-of-the-art diagnostics with which to study the plasma physics of the plasma focus. The results of these studies are being prepared for publication .

#### B. Research Objectives

As stated in the proposal, the overall goal of the research was to complete the testing of the plasma focus as an opening switch (PFOS) in the Filippov geometry with sufficient time allotted so the two graduate students could complete the experiments required for thier thesis. Since the utility of the PFOS concept has always been uncertain and since theses must contain successful results for publication and to further careers, the testing of the PFOS concept was not chosen for either thesis.

### C. Status

While I was able to perform considerable analysis as to the merit of the Filippov geometry in the opening switch configuration of the load coupled directly to the anode (Fig. 1), the experiments required to support the student theses tied up the plasma focus device for the entire period of funding. While there is a small chance the Filippov experiment will be performed this spring while Mr. Venneri is writing up his Ph.D. thesis, there are no new experimental results at this time. However, the experiments involving the student theses were enormously successful, being sort of a rite of passage for both students and launching them both on promising careers as experiment research scientists.

In the first section C1 the analysis and prospects for the plasma focus as an opening switch will be presented briefly, with the details supporting the conclusions included as Appendix A. Then the highlights of the Francesco Venneri's and Kevin Boulais' theses are presented in section C2 and C3; Mr. Boulais' Masters's thesis is included as Appendix B. A copy of Mr. Venneri's thesis will be sent to AFOSR as soon as he has completed the requirements for the Ph.D.

# C1. Analysis of the PFOS Concept

An equivalent circuit for the plasma focus load circuit is shown in Fig. 1. The energy is stored in the external circuit inductance  $L_S$  which drives the plasma to a pinch at  $t=0$ . The resistance of the pinched plasma is represented by  $R_0(t)$  taken to be a step function beginning at  $t=0$  when  $S_2$  is closed. For the fast transients considered here, it is assumed the capacitor bank has a negligible effect.

Previous solutions<sup>1</sup> included only a load inductor, but recently the solution was extended to include a series load resistor,  $R_L$ . This permits the model to be applied to more realistic loads including transmission lines, or pulse forming networks which are commonly used<sup>2,3</sup> to match Marx generators with beam diodes. The impedance of these networks are typically  $1\Omega$ .<sup>2,3</sup>

The analytic solution is as follows. The load current,  $I_L$  is given by:

$$I_L = + \frac{I}{(\beta_1 - \beta_2)L_S} \left( (\beta_1 - \alpha)e^{-\beta_2 t} \left( \frac{R_0}{\beta_2} - L_S - L_0 \right) - (\alpha - \beta_2)e^{-\beta_1 t} \left( L_S + L_0 - R_0 \beta_1 \right) \right) \quad (1)$$

where  $\beta_1 = \frac{F_L + \sqrt{F_L^2 - 4R_L R_0 D_\alpha}}{2D_\alpha}$

$$\beta = \frac{F_L - \sqrt{F_L^2 - 4R_L R_0 D_\alpha}}{2D_\alpha}$$

$$F_L = R_L(L_S + L_0) + R_0(L_S + L_L)$$

$$D_\alpha = L_L L_S + L_0(L_S + L_L)$$

and  $\alpha = R_0(L_S + L_L)/D_\alpha$



From this the voltage drop and energy transferred to the load resistor,  $V_L$  and  $E_L$  respectively, can be calculated and the time,  $t_M$ , of the peak power transfer to the load can be found.

From our previous experiments<sup>4</sup>, where the peak load current  $I_L \sim 14\text{kA}$ ,  $L_S = 17\text{nH}$ ,  $L_0 = 29.4\text{nH}$ ,  $L_L = 30\text{nH}$ , and  $R_L = 0.8\Omega$ , one finds that the solution best fits the data if  $R_0 \sim 0.07\Omega$ . This value is in the range observed in other plasma focus experiments.<sup>5</sup>

If one assumes  $R_0 \sim 0.1\Omega$  independent of the device and varies  $R_L$  for the Limeil<sup>6</sup> Filippov plasma focus (which is of more optimal design) where  $L_S = 17\text{nH}$ ,  $L_0 = 21.9\text{nH}$ ,  $L_L = 6\text{nH}$  one can find the peak  $I_L$ ,  $V_L$ ,  $E_L(t_M)$ ,  $E_L(\infty)$  and  $t_M$  for each  $R_L$  from equation 1. This is shown in Fig. 2.

As can be seen, the  $E_L(t_M)$ ,  $E_L(\infty)$  and  $I_{Lpk}$  all suffer a decrease with increasing  $R_L$ , especially for  $R_L > 0.1\Omega$ . While the peak voltage increases with  $R_L$  as desired, these effects are overcome by the decreases in  $I_{Lpk}$  and  $E_L(\infty)$ . The latter being less than 2% of the total inductive energy available  $E_0$  ( $E_0 = 1/2(L_S + L_0)I_0^2 = 63\text{kJ}$ ).

The problem is that the opening resistance of the plasma focus appears to be too low to permit the transfer of a significant portion of the initial energy on a short time scale. This can be seen in the following. If one assumes a fixed  $R_L$  of  $1.0\Omega$  in the previous example and varies  $R_0$  between  $0.1$  and  $10$  ohms one finds the ratio of  $E_L(\infty)/E_0$  increases from  $0.018$  to  $0.276$  and  $t_M$  decreases from  $52\text{ns}$  to  $6.3\text{ns}$  (Fig. 3). The fraction of the initial energy  $E_0$  stored in the inductances  $L_S$  and  $L_0$  ( $E_0 = 63\text{kJ}$  for this example) transferred to the load (by  $t = 4t_M$ ) is  $\sim 0.01E_0$  for  $R_0 = 0.1\Omega$  to  $0.23E_0$  for  $R_0 = 10\Omega$  with  $E_L(4t_M) > 0.1E_0$  for  $4t_M < 92\text{ns}$  for  $R_0 > 1.0\Omega$ . The rest of the energy  $E_0$  is consumed in  $R_0$  during this period.

Thus the plasma focus would be a potentially useful pulsed power device for  $R_0 > 1.0\Omega$  but unfortunately our measurements are consistent with a value of less

than 10% of this. While at best (for  $R_0 = 10\Omega$  over 3/4 of the initial energy is consumed in the switch) the fast energy transfer time ( $4t_M \sim 25\text{ns}$ ) would make it very attractive, for the  $R_0$  observed ( $\sim 0.1\Omega$ ), the transfer times are too long ( $4t_M \sim 200\text{ns}$ ) and the fraction transferred too small ( $E_L(4t_M) \sim 0.01 E_0$ ) to seriously consider the focus as a candidate for an opening switch.

In all this analysis, it was assumed that  $R_0$  was constant for several times  $t_M$ , however in reality the enhanced resistance only occurs over roughly the duration of the pinch (or the period of stability)  $\tau$ . For Mather-type plasma focus devices this period can vary from 10-20ns for a 1kJ device to  $\sim 150\text{ns}$  for a device of a few hundred kilojoules. Through considerable analysis of our experimental data and that from other devices, we have developed a scaling law to predict this period. This analysis is useful to determine whether the energy transfer could actually occur or be interrupted prematurely if  $\tau < 4t_M$ . Thus it would be essential in developing the plasma focus as an opening switch especially if  $R_0 > 1.0\Omega$  and is included here as Appendix A.

Basically in the analysis it is found that the stability period  $\tau = \alpha r_0/V_r$  where  $r_0$  is the pinch radius,  $V_r$  is the radial collapse velocity and  $\alpha$  is a constant of proportionality; this is consistent with experiment.<sup>1</sup> Since empirically  $r_0 \propto r_A^{1-3}$  where  $r_A$  is the anode radius. Longer  $\tau$  and hence transfer periods may be obtainable by increasing  $r_0$ .

## C.2 Francesco Venneri's Ph.D. Thesis Project

In order to measure the electron temperature during the pinch to determine the Spitzer resistivity and the speed of sound, a dispersive element is necessary to avoid errors due to contamination of the spectrum due to line radiation caused by impurities. For example, using a filter technique and assuming a free-free bremsstrahlung-type spectrum, plasma focus researchers have tended to estimate the electron temperatures to be in the multi keV range

whereas using laser scattering they tend to be in the sub-keV range.<sup>7</sup> In our device using filters and assuming a bremsstrahlung spectrum, we have measured electron temperatures to be in the 300-500eV<sup>8</sup> range but the presence of line radiation can not be ruled out.

A dispersion element, such as a crystal spectrometer, permits the dispersion of the radiation as a function of a wavelength so the spectrum can be observed photographically and the regions of line radiation and bremsstrahlung can be identified and separated. Thus the radiation can be analyzed using the proper model for that region of the spectrum and an accurate value of the electron temperature determined.

For Mr. Venneri's thesis project, it was decided to construct a state-of-the-art curved-crystal spectrometer<sup>9</sup> for this purpose. In the following subsections the spectrometer will be described and some typical experimental results presented. How these results have been applied to the project is illustrated in Appendix A.

#### A. Curved Crystal Spectrometer

A crystal spectrometer uses the diffractive properties of crystals to isolate wavelength in a distribution of x-rays, so that they can be detected individually. Due to the regularities of crystal lattices, x-rays of the same wavelength, scattered from different crystalline planes, experience constructive or destructive interference, depending on the differences in their path lengths.

The interference is such that, for crystals with a sufficiently large number of parallel planes, only the x-rays with wavelengths obeying the simple Braggs' rule are constructively diffracted (reflected) at a certain angle ( $\theta$ ) (Fig. 4):

$$n\lambda = 2d\sin(\theta)$$

Where:  $n$  = Order of the diffracted beam (equal to the number of the first plane under the surface from which the wavelength is constructively diffracted).  
 $d$  = interplanar spacing of the crystal.  
 $\lambda$  = diffracted x-ray wavelength.  
 $\theta$  = angle of diffraction.

When analyzing a pulsed source such as a pinched plasma, a plane crystal can offer only a limited range of diffraction angles to an incoming (diverging) x-ray beam, and no range at all if the beam is collimated parallel. To detect a wider portion of the spectrum a curved crystal should be employed.<sup>9</sup>

In the x-ray spectrometer developed for the Dense Plasma Focus, the curved crystals are elliptically bent with the plasma filament (pinch) at the far focus of the ellipse. The curvature in the crystal produces a continuous range of incidence angles between the incoming beam and the crystal planes. Different frequencies are constructively diffracted at different angles, then converge to a common crossover point (the near focus of the ellipse) and finally diverge towards the detection circle.

The beam is unrestricted (diverging) in the horizontal plane, but collimated in the vertical direction (pinch axis) to exclude viewing of the electrode region. At the crossover point, a collimating vertical slit (parallel to the pinch) is placed to reduce the background radiation from regions outside the far focal axis of the ellipse (location of the pinch).

On the detection circle, an array of solid state detectors (PIN diodes) provides time resolved, space averaged readings of the X-ray emission at selected spectrum locations.

An aluminized Kinfol vacuum window (0.1u aluminum deposited on 2u Kimfol) filters visible and UV light out of the spectrometer, which is kept under oil-free vacuum to prevent attenuation of the x-rays, contamination of the detectors and breakdown of their bias.

Different crystals can be used in the spectrometer, each with its own different interplanar spacing and useful frequency range, not to mention bending and mounting techniques. The geometric resolution of the spectrometer depends on the match of detector and crystal geometry. At a detection circle of 15 cm in radius the resolution is between .5 and 2 eV/mm, depending on the eccentricity of the crystal ( $dE/E = 1/1000$  for KAP and PET,  $1/20000$  for LiF).

#### B. Temperature Measurements

The electron temperature of our DPF was determined as a function of time, using the curved crystal spectrometer (Fig. 5).

After a line-free region of the spectrum was located (energy regions above the highest line), the bremsstrahlung emission was monitored with three PIN diode detectors. This allows to determine the temperature as a function of time in the pinch.

The temperature is in fact proportional to the logarithmic slope of the bremsstrahlung spectrum and the use of three detectors allows the verification of the effective thermal nature (as opposed to beam target) of the monitored continuum.

This method is applicable (with high efficiency crystal geometries) even to pure hydrogen or deuterium discharges. There is no need to use a seed gas to enhance the x-ray emission, unless it is of course desired to investigate the spectrum of such seed gas.

For hydrogen and deuterium discharges the temperature was determined using a 100 mm x 20 mm PET crystal of eccentricity 0.806 placed at a focal length of 65 cm from the Plasma Focus pinch. The energy bands selected for this application were 1468 eV ( $\pm 5$  eV) and 1670 eV ( $\pm 6$  eV). The spectrometer was independently calibrated using a foil filter technique (filtered detectors mounted at the end of a 4 m collimating tube) and a second crystal spectrometer (flat PET crystals at 1592 eV and 2006 eV). The relative efficiencies of the PIN diode detectors

were also determined employing the long collimating tube to view the same region of the plasma pinch during a series of calibration discharges.

The measure temperatures range between 200 eV and 400 eV (Fig. 6).

The temperature obtained using this technique is very nearly the maximum temperature obtained at the most dense part of the pinch, as it develops as a function of time. In fact the dependence of the bremsstrahlung radiation on the square of the density and exponentially on the temperature heavily weighs the hottest and most dense regions of the pinch as the radiation is averaged over the viewed emitting region.

These results are the first using this type of spectrometer on a plasma focus and generated considerable interest during two presentations at plasma physics meetings.<sup>10-11</sup>

### C.3. Kevin Boulais' Masters Thesis

Although we have been operating our plasma focus since 1978, we had no measurement of the plasma density or its profile until this year when Mr. Boulais' laser interferometer came on line. With such an instrument, one can obtain a snapshot of the density profile in the plasma focus (see both appendices) at one instant ( $\Delta t < 5\text{ns}$ ) per shot. Through a series of runs, we have determined that the dynamics of the plasma (as opposed to the neutron yield) are reproducible enough, so that a reasonable understanding of the events taking place can be obtained. This is clearly shown in Appendix A where the decay in the number of particles per unit length can be used to obtain an estimate of the magnitude of the axial flow velocity. This velocity appears to be great enough to explain the stability of the pinch. Before Mr. Boulais' interferometer came on the scene, we could only speculate about this.

Mr. Boulais' achievement is clearly remarkable since no one on campus had any experience in this area and he only interacted with experts briefly at a few meetings. Never-the-less the interferograms obtained are remarkable for their clarity.

Mr. Boulais is now pursuing his career investigating microwave generation by relativistic electron beams at the Naval Surface Weapons Laboratory in Silver Spring, Maryland and hopes to continue toward a Ph.D. in electrical engineering at the University of Maryland next fall (1988).

For the details of his achievement, his M.S. thesis is reproduced as Appendix B.

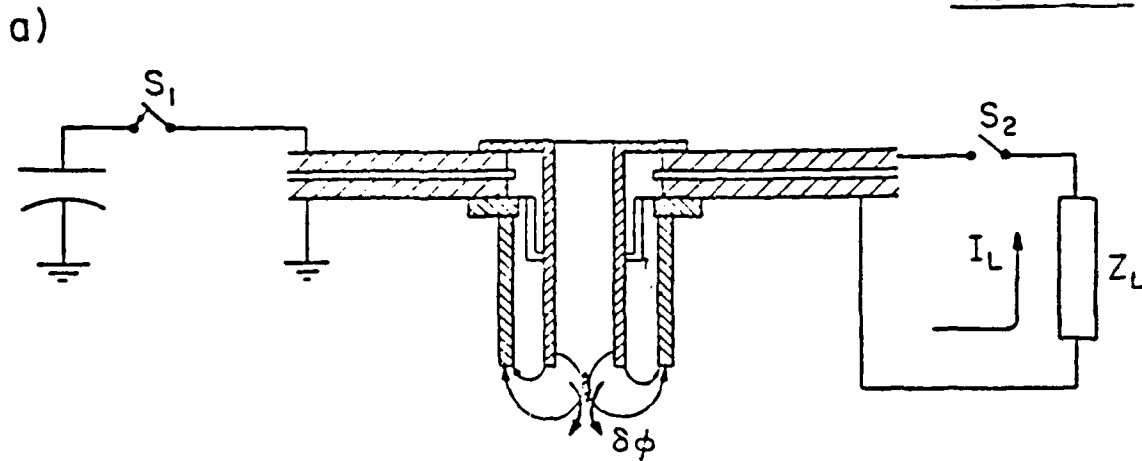


Figure 1a. The operation of a plasma focus-load configuration with a load tap behind the anode. The switch  $S_2$  is closed at pinch time trapping the magnetic flux associated with plasma focus inductance ( $L_0$ ) in the load circuit. When the flux  $\delta\phi$  subsequently leaks out the current  $I_L$  is driven through the load impedance  $Z_L$ .

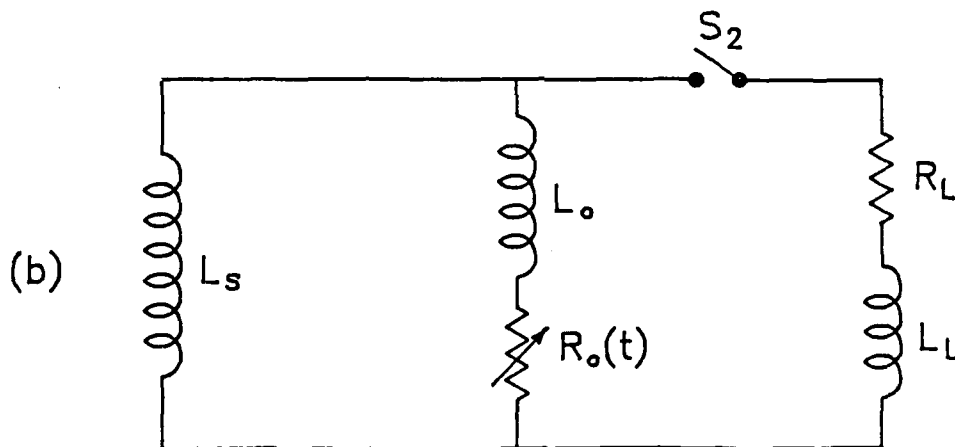


Figure 1b. The circuit modeled in the calculations presented in this section where the plasma focus resistance is represented by  $R_o(t)$ . The load resistor  $R_L$  has been added to generalize the model so it may be more readily compared with the experiment.



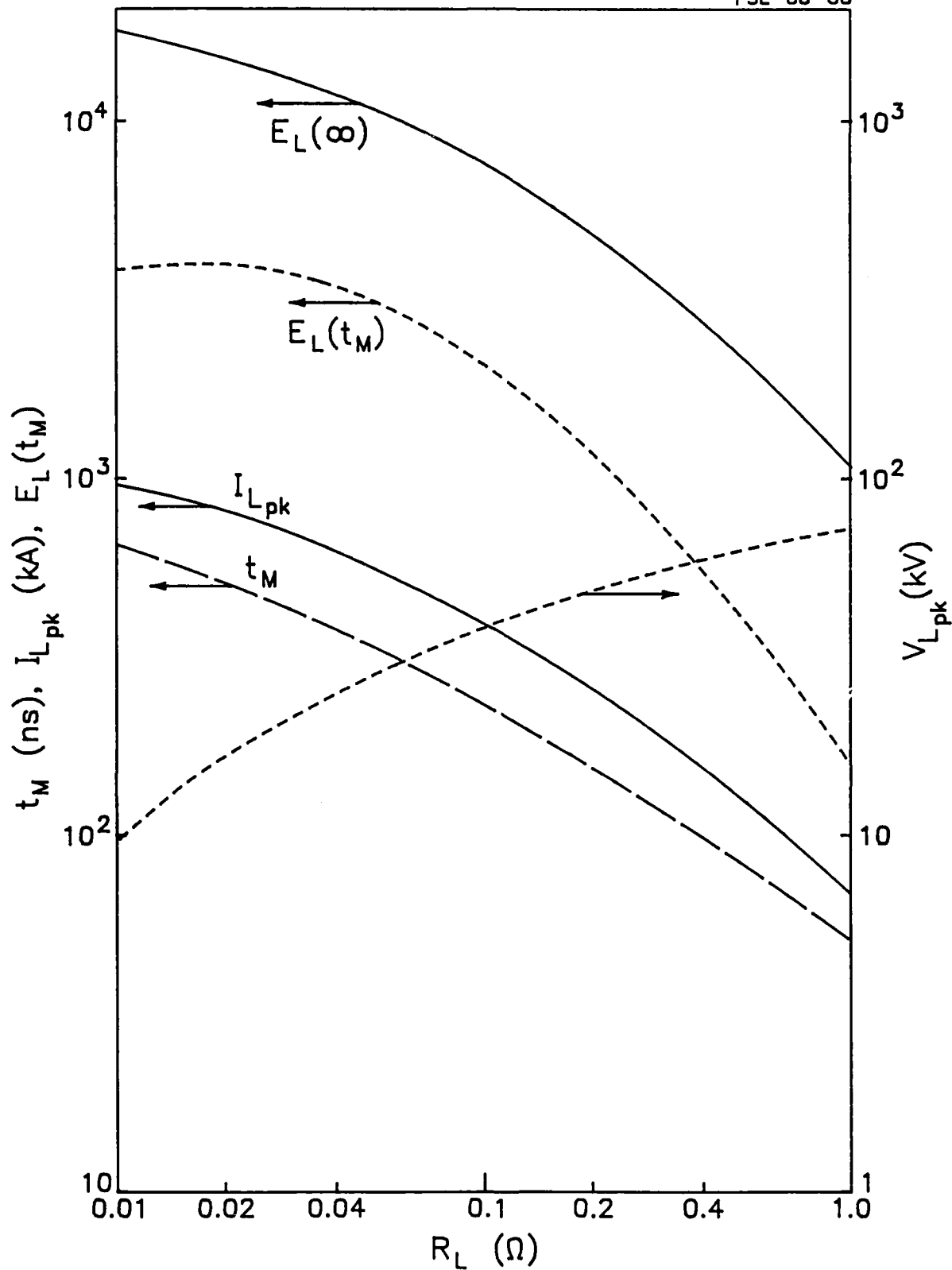


Figure 2. Effect of varying the magnitude of the load resistor,  $R_L$ , for the Limeil<sup>6</sup> Filippov plasma focus where  $R_0 = 0.1\Omega$ ,  $L_s = 17\text{nH}$ ,  $L_0 = 21.9\text{nH}$ ,  $L_L = 6\text{nH}$  and  $E_0 = 63\text{kJ}$  (Fig. 1).  $E_L(\infty)$ ,  $I_{Lpk}$ ,  $t_M$ ,  $E_L(t_M)$  and  $V_L$  are the maximum energy transferred to  $R_L$ , the peak current in  $R_L$ , the time of the current peak, the energy transferred to  $R_L$  by  $t_M$  ( $R_0$  is a step function beginning at  $t=0$  when  $I_L = 0$ ).  $V_{Lpk}$  is the peak load voltage.

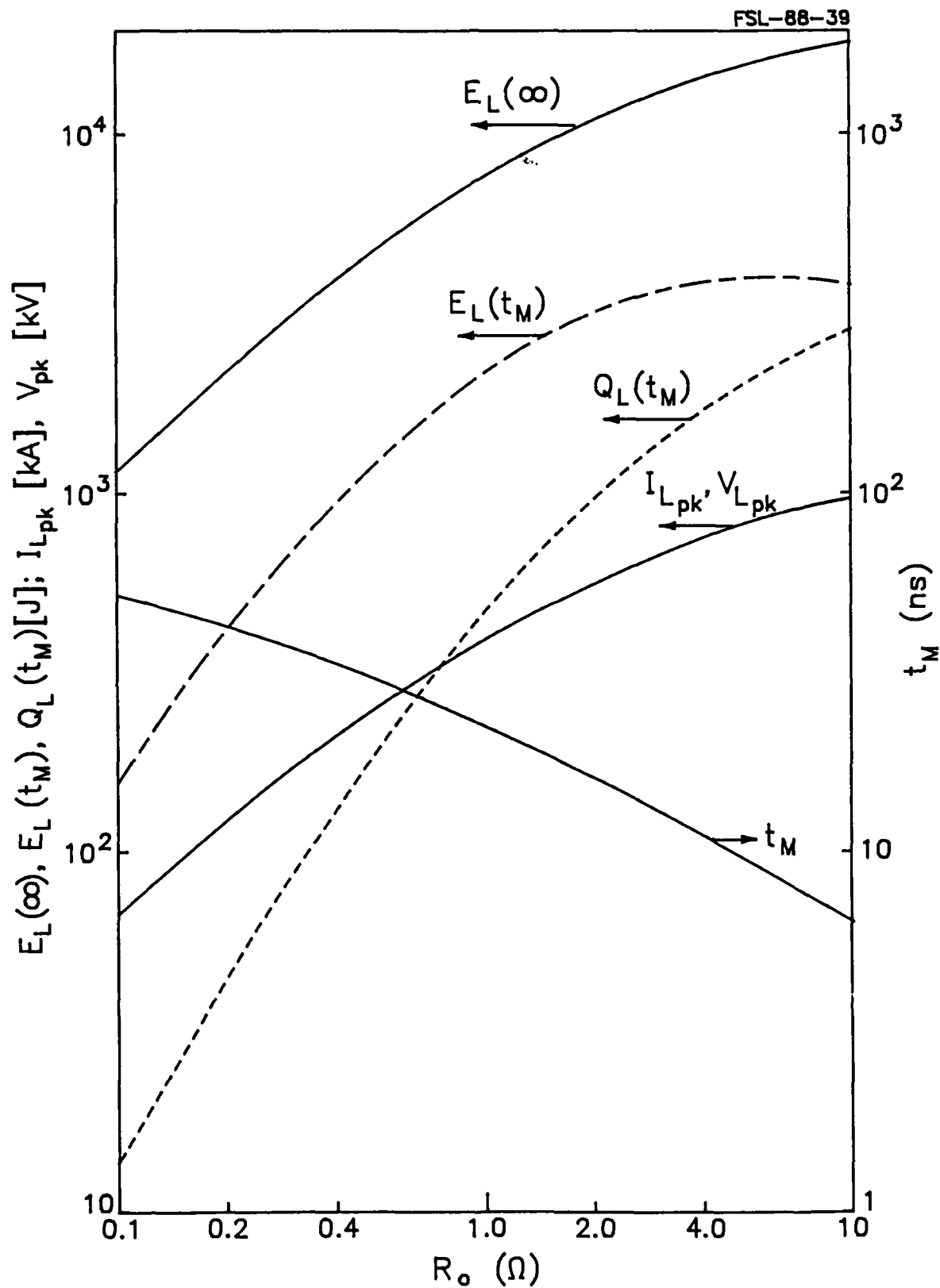


Figure 3. Effect of varying  $R_o$  on  $E_L(\infty)$ ,  $E_L(t_M)$ ,  $Q(t_M)$ ,  $I_{pk}$ ,  $V_{pk}$ , and  $t_M$  for  $R_L = 1.0\Omega$ .  $Q(t_M)$  is the reactive energy stored in the load at  $t_M$ . The rest of the circuit parameters are the same as in Fig. 2.

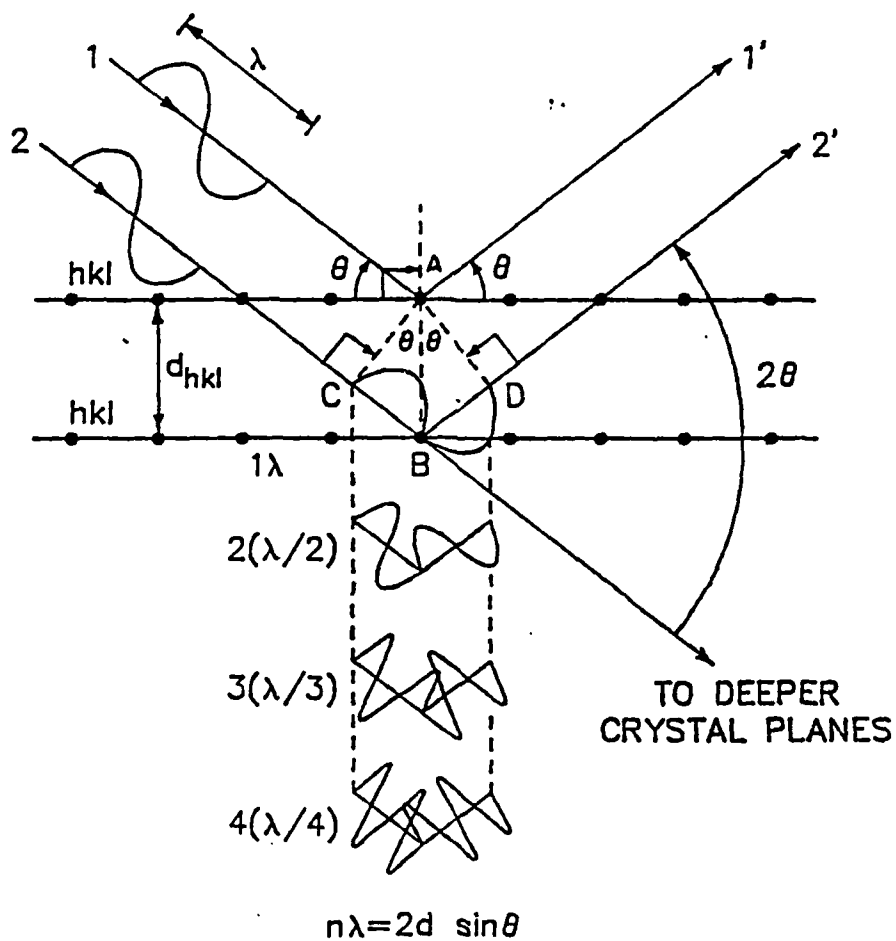


Figure 4. Illustration of Bragg's dispersion law for a crystal spectrometer. By choice of different  $d$  (i.e. different crystal types) different regions of the soft x-ray spectrum may be investigated.

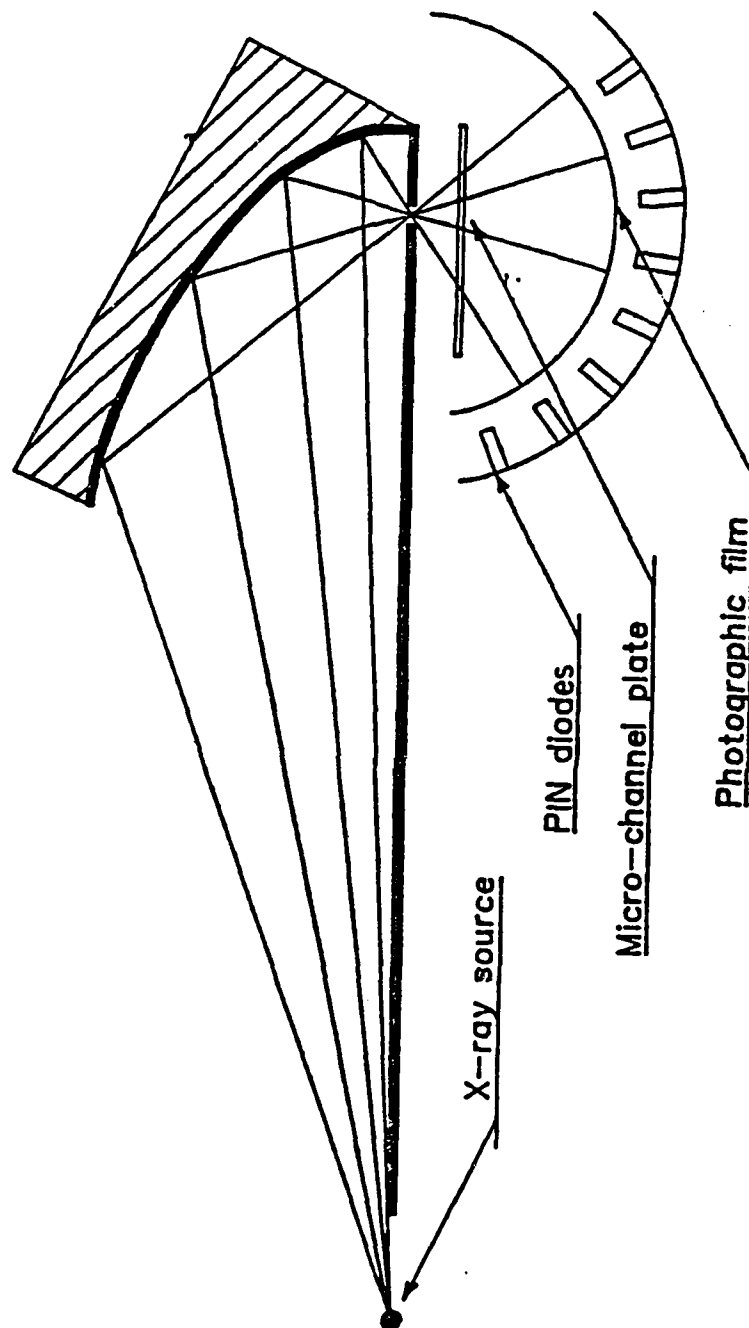


Figure 5. Elliptical curved crystal spectrometer used to determine the electron temperature. The plasma column is at one focus of the ellipse and the cross over point at the other. Pin diodes and/or photographic film on the detection circle are used to detect different spectral bands of the soft x-ray emission.

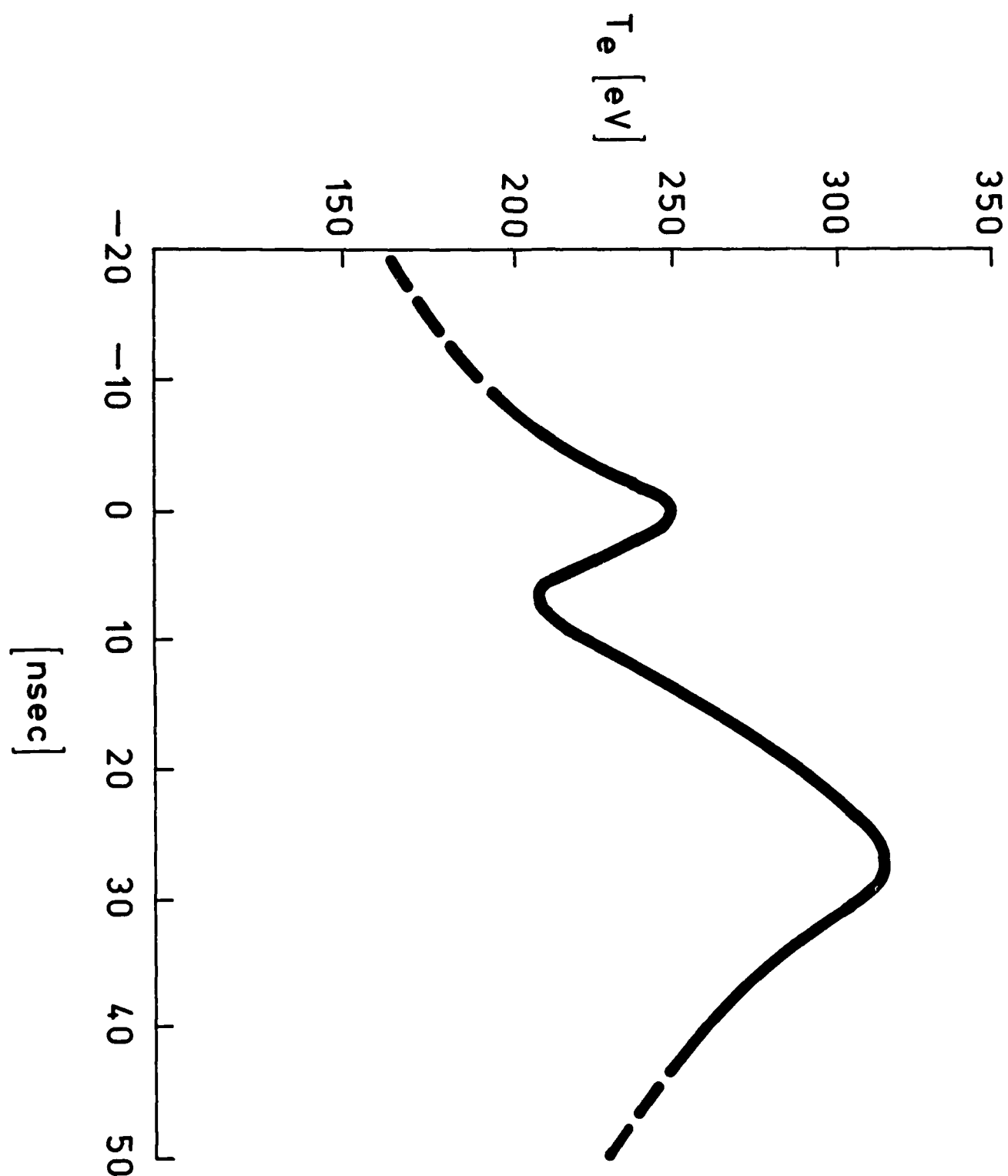


Figure 6. Typical time dependence of the electron temperature of the pinched plasma obtained with the curve crystal spectrometer for  $p_0 = 3$  torr (deuterium and  $I = 550$  kA. Comparison with simultaneous laser interferograms indicates the first peak corresponds to first compression, the dip to radial expansion and the second peak to second compression.

D. Cumulative Chronological List of Publications (AFOSR-86-0303):

G. Gerdin, F. Venneri, and K. Boulais, "A Scaling Law for Macroscopic Stability of the Mater-type Plasma Focus," submitted to Plasma Physics and Controlled Nuclear Fusion and reproduced here as Appendix A.

E. List of Professional Personnel Associated with the Research Effort

Personnel

Dr. Glenn Gerdin, Principal Investigator  
2317 Kaufman Duckworth Hall(Present address)  
Dept. of Electrical and Computer Engineering  
Old Dominion University  
Norfolk, VA 23529-0246

Mr. F. Venneri, Ph.D. candidate  
Dept. of Nuclear Engineering  
University of Illinois  
214 Nuclear Engineering Lab  
103 S. Goodwin Ave.  
Urbana, IL 61801

Mr. K. Boulais  
Naval Surface Weapons Center  
Silver Spring, MD 20902-5000

Advanced Degrees

Mr. K. Boulais, Degree of Master of Science in Electrical Engineering,  
Sept. 1987.

Mr. F. Venneri is in the process of writting his Ph.D. thesis in Nuclear Engineering at this time. He has accepted a position with the Max Planck Institute in Garching, West Germany starting in the fall of 1988.

F. Interactions: Conference Papers

K. Boulais, G. Gerdin, and F. Venneri, Bult. Amer. Phys. Soc. 31, 1456 (1986).

F. Venneri and G. Gerdin, Bult. Amer. Phys. Soc. 31, 1461 (1986).

F. Venneri and G. Gerdin, IEEE Int. Conf. on Plasma Sci. Arlington VA. Conf.-Record-Abstracts, IEEE Catalog No. 87CH2451-3,44 (June, 1987).

G. Gerdin, F. Venneri, and K. Boulais, IEEE Int. Conf. on Plasma Sci. Arlington VA, Conf.-Record-Abstracts, IEEE Catalog No. 87CH2451-3,44 (June 1987).

K. Boulais, F. Venneri, and G. Gerdin, Bult. Amer. Phys. Soc. 32, 1759 (1987).

F. Venneri, K. Boulais, and G. Gerdin, Bult. Amer. Phys. Soc. 32, 1778 (1987).

### References

1. F. Venneri, J. Mandrekas, G. Gerdin, Proc. 4th IEEE Pulsed Power Conf., Albuquerque, NM, June 1983, IEEE Catalog No. 83CH1908-3, 350.
2. G. B. Frazier, S. R. Ashby, D. M. Barrett, M. S. DiCapua, L. J. Demeter, R. Huff, D. E. Osias, R. Ryan, P. Spence, D. F. Strachan, and T. S. Sullivan, Proc. 3rd IEEE Pulsed Power Conf., Albuquerque, NM, June 1981, IEEE Catalog No. 81CH1662-6, 8.
3. K. Imasaki, S. Miyamoto, T. Ozaki, S. Higaki, S. Nakai, and C. Yamenaka, Proc. 3rd IEEE Pulsed Power Conf., Albuquerque, NM, June 1981, IEEE Catalog No. 81CH1662-6, 2.
4. F. Venneri, H. Krompholz, J. Mandrekas, G. Gerdin, and M. Tanis, Bult. of Amer. Phys. Soc. 28, 1171 (1983).
5. A. Bernard, A. Coudeville, J. P. Garconnet, A. Jolas, J. de Mascureau, C. Nazet, 6th Intern. Conf. on Plasma Phys. and Centr. Nucl. Fusion Res., Berchtesgaden, FRG, III, 471 (IAEA, Vienna, 1976).
6. A. Bernard, A. Coudeville, A. Jolas, J. Launspach, and J. de Mascureau, Phys. Fluids 18, 180 (1975).
7. J. P. Rager, private communication 1984.
8. F. Venneri, and G. A. Gerdin, Proc. Int. Conf. on Plasma Sci., St. Louis, MO, 104 (1984).
9. B. L. Henke, H. T. Yameda, and T. J. Tanaka, Rev. Sci. Instr. 54, 1311 (1983).
10. F. Venneri and G. Gerdin, IEEE Int. Conf. on Plasma Sci., Arlington, VA, Conf. Record-Abstracts, IEEE Catalog No. 87CH2451-3, 44 (1987).
11. F. Venneri, K. Boulais, and G. Gerdin, Bult. Amer. Phys. Soc. 32, 1778 (1987).

APPENDIX A

A Scaling Law for Macroscopic Stability  
of the Mather-type Plasma Focus<sup>+</sup>

G. Gerdin<sup>\*</sup>, F. Venneri, and K. Boulais<sup>\*\*</sup>

Dept. of Nuclear Engineering  
University of Illinois  
Urbana, IL 61801

<sup>+</sup> Work supported in part by a grant from the Air Force Office of Scientific Research, Grant No. AFOSR-86-0303

<sup>\*</sup> Present Address: Dept. of Electrical and Computer Engineering, Old Dominion University, Norfolk, VA 23529-0246.

<sup>\*\*</sup> Present Address: Naval Surface Weapons Center,  
Silver Spring, MD 20903-5000



### Abstract

By use of a streak camera aligned either along the axis of the pinched plasma or at  $90^\circ$  to it, the distance along the axis between first and second compression,  $h$ , and the minimum radius of the pinch,  $r_0$ , have been measured as a function of the plasma current,  $I$ , and filling pressure,  $p_0$ . The plasma current was measured by magnetic-pickup loops calibrated to 35MHz with Helmholtz coils. The results are that  $h \propto I^x p_0^y$  where  $x = -0.02 \pm 0.12$  and  $y = 0.26 \pm 0.13$  and that  $r_0 \propto I^a p_0^b$  where  $a = -0.18 \pm 0.11$  and  $b = 0.2 \pm 0.03$ . Thus within the experimental uncertainties  $h = \alpha r_0$  where  $\alpha = 8.6 \pm 2.4$ . These results may be correlated to the stability period  $\tau$  by use of the zippering effect; the latter predicts the radial collapse velocity  $v_r$  should be directly related to the speed  $v_c$  of the compression wave traveling along the column. These latter two quantities are found to exhibit the same dependences with  $I$  and  $p_0$  within less than 10% experimental uncertainties in their power-law slopes. The empiracle scaling of  $\tau$  with  $p_0$  and  $I$  found here is consistent with results of other plasma focus devices and is consistent with ideal MHD stability theory. Experimentally,  $\tau$  is found to be enhanced over that of a straight cylinder by a factor  $\alpha' = 2.7 \pm 0.6$ . Two simple models consistent with ideal MHD theory could explain this enhancement.

A Scaling Law for Macroscopic Stability  
of the Mather-type Plasma Focus  
G. Gerdin, F. Venneri, and K. Boulais

I.) Introduction

Stability of the plasma focus<sup>1,2</sup> or non cylindrical Z pinch is of interest for both theoretical and practical reasons. Theoretically the stability of the Z pinch represents a classic problem in magnetohydrodynamic (MHD) theory, which predicts the column should be unstable to the MHD equivalent of the Rayleigh-Taylor modes<sup>3,4</sup> and thus presents an opportunity for a direct comparison between theory and experiment. From a practical point of view Z pinches, both compressional and gas-embedded, could represent a relatively inexpensive approach to thermonuclear fusion if the period of stability can be made long enough.<sup>5</sup> The plasma focus represents a cross between these two approaches to Z pinches being formed in a similar manner to the compressional Z pinch<sup>6,7</sup> but having higher plasma densities<sup>1</sup> such as those of the gas-embedded Z pinch. In addition the discharge currents in the plasma focus<sup>8</sup> are also much higher, which reduces finite larmor radius (FLR) effects. Hence understanding the stability of the plasma focus could have applications to other types of Z pinches especially in the classical MHD limit of small ratios of ion gyroradius ( $r_{ci}$ ) and mean free path ( $\lambda_{ii}$ ) to plasma radius ( $r_0$ ; i.e.  $r_{ci}/r_0 \leq 0.1$  and  $\lambda_{ii}/r_0 \leq 0.1$ ).

Besides the similarities to Z pinch approaches to controlled fusion, understanding the plasma focus is of interest in its own right. Until 1978 the plasma focus held the record for the most fusion neutrons produced per shot.<sup>9</sup> It has been observed in large plasma focus devices that the majority of the neutron production occurs during the stable pinch phase<sup>10</sup>; hence determining the physics behind the stability of the plasma focus could lead to a viable controlled fusion

concept. Secondly, soft x-rays are produced during the pinch phase which may be used in soft x-ray lithography and microscopy<sup>11</sup>; the duration of the soft x-ray pulse could be optimized by the understanding of plasma focus stability. Finally the voltage pulse and peak current interruption generated by the device occur during the pinch phase,<sup>12</sup> hence investigating the stability of this device could lead to important applications in pulsed power.

Experimentally the plasma focus discharge is observed<sup>13</sup> to be terminated by a Rayleigh-Taylor-like  $m=0$  (or sausage) instability. However the period of the stable phase is typically<sup>1</sup> several times the inverse of the classical growth rate<sup>3,4</sup> for this instability. In this paper experimental evidence is presented for an empirical scaling law for the period of stability or more directly the scaling law for  $h$ , the distance along the plasma column between the site of the  $m=0$  instability and the end of the column. Then the theoretical basis for such scaling is reviewed and these scaling laws (both empirical and theoretical) are applied to predict the period of stability in other Mather-type<sup>1</sup> plasma focus devices.

In the next section the phenomena of the plasma focus discharge related to the macroscopic stability (such as current sheath dynamics) are described. In Section III the experimental apparatus is described and the experimental results governing the current sheath dynamics and the scaling of  $h$  and  $r_0$  with plasma current and filling pressure are presented. In Section IV the theoretical models are formulated to predict the scaling of  $h$  and the period of stability,  $\tau$ , with  $r_0$ , pinch current and filling pressure and compared with the empirical laws presented in Section III. Also in Section IV these theoretical and empirical laws are applied to predict  $\tau$  in other Mather-type plasma focus devices and compared with experiment.

## II.) Relationship of h to stability

After the current sheath of a Mather-type plasma reaches the end of the center electrode (Fig. 1) the current sheath collapses radially into a pinch along the device axis. On reaching the axis the current sheath compresses, radially expands and then recompresses.

The second compression is associated with  $m=0$  instabilities<sup>13</sup> which occur at the end of the radial expansion phase.<sup>14,15</sup> The results reported here are in agreement with those findings. The predicted period of stability<sup>3,4</sup> for a cylindrical column  $\tau \approx r_0/v_s$  is about 5ns (where  $v_s$  is the velocity of sound) whereas the observed stable periods are typically 10 times this.<sup>13</sup> For compressional Z pinches the enhancement factor is at least 20 which is usually explained by finite Larmor radius (FLR) effects.<sup>5</sup> But due to the higher magnetic fields present in the plasma focus this mechanism should be ineffective.

Alternatively, the pinch column is observed to be stable as long as the column length  $\ell$  is less than a certain number  $\alpha$  of column diameters  $d$  where  $2 < \alpha < 100$  experimentally and most typically about ten.<sup>16</sup> Since the current sheath is radially concave during the radial implosion phase, the pinch first occurs in the midplane and then lengthens as the trailing portions farther and farther off the mid-plane reach the axis in the so-called zippering effect (Fig. 2).<sup>17</sup> Thus the apparent speed of the lengthening of the column,  $v_c$ , is related to the radial velocity of the implosion,  $v_r$  (which is roughly a constant in the midplane, Fig. 3). Therefore one might expect the period of stability,  $\tau$ , to scale as:

$$\tau \approx \frac{\ell}{2 v_c} \approx \frac{\alpha d}{2 v_c} \approx \frac{\alpha r_o}{f v_r} \quad \text{II.I)}$$

where  $f$  is a constant on the order of 2 to 3 taken from experiment.

Since  $h \approx \ell/2$

$$\tau \approx \frac{h}{v_c} \approx \frac{\alpha r_o}{f v_r} \quad \text{II.2)}$$

$$\text{or} \quad h \approx \frac{\alpha}{f} \frac{v_c}{v_r} r_o = \alpha' r_o \quad \text{II.3)}$$

so if  $v_c \propto v_r \propto v_s$  then one would expect  $\tau \approx \alpha' r_o / v_s$ , where  $\alpha' = \alpha(\gamma/2)^{1/2}/f$  for  $\beta = 1$ .

To illustrate how  $v_c$  and  $v_r$  could be related geometrically consider the following simple model. Instead of a cylinder, consider the radially collapsing current sheath as a concave hyperbola of revolution (Fig. 2) moving radially inward with a uniform  $v_r$ . As the first compression occurs on the midplane the surface of the column may be represented by:

$$r^2 = \kappa Z^2 + r_o^2 \quad \text{II 4.)}$$

where  $Z$  is the distance along the axis from the midplane and  $r$  is the radial position of the current sheath at height  $Z$  (Fig. 2). For  $Z, r \gg r_o$  one has  $v_c = \kappa^{1/2} v_r$  where  $v_c = \dot{Z}$ . Thus one would expect  $v_c$  and  $v_r$  to be directly related, where  $f = \kappa^{1/2}$  in equations II 1.) to II 3.). This zippering effect occurs in all Mather-type plasma focus devices and has been reported previously.<sup>18</sup>

Thus this elementary model predicts  $h$  should be directly related to  $r_o$  if  $v_c$  and  $v_r$  are also directly related. In the next section the experimental evidence to support this model will be examined.

### III. Experimental Procedures and Results

#### IIIa. Experimental Apparatus and Diagnostic Tool

The dense plasma focus (DPF) used in the measurements reported here is a Mather-type<sup>19</sup> (Fig. 1). The center electrode is hollow and has an outer diameter of 5.08 cm. the inner diameter of the outer electrode is 10.2 cm and the center electrode extends 14 cm beyond a lavite insulator. The input energy on the capacitor bank (40 $\mu$ F) was varied between 6 and 18 kJ in these measurements and the filling pressure varied between 1 and 8 torr of deuterium.

The velocities of the plasma edge and the occurrence of macroscopic instabilities were recorded with a streak camera either lined up with a vertical slit to observe events along the axis of the pinch (z streak, Fig. 4) or horizontally to observe the radial motion of the plasma column. The minimum radius,  $r_0$  was also taken from the radial streak pictures, whereas h was taken from the axial streak pictures (Fig. 5). The plasma current was measured with magnetic-pickup loops 1mm in diameter placed in a quartz tube with an outer diameter of 3 mm. The loops were calibrated with Helmholtz coils out to 35MHz and placed midway between the inner and outer electrodes a few centimeters below the top of the center electrode. Plasma density and density gradient scale lengths of the pinched plasma were measured for some discharges by use of a Mach-Zehnder interferometer and a nitrogen laser ( $\lambda=337\text{nm}$ ).<sup>20</sup>

Using a curved crystal spectrometer<sup>21,22</sup> (Fig. 6), the electron temperature of our DPF was determined as a function of time. After a line-free region of the spectrum was located (energy regions above the highest line), the bremsstrahlung emission was monitored with three PIN diode detectors. This allows the determination of the temperature as a function of time in the pinch. The temperature is proportional to the logarithmic slope of the

bremsstrahlung spectrum and the use of three detectors permits the verification of the effective thermal nature (as opposed to beam target) of the continuum.

This method is applicable (with our high efficiency crystal geometries) even to pure hydrogen or deuterium discharges. There is no need to use a seed gas to enhance the x-ray emission, unless it is of course desired to investigate the spectrum of such seed gas.

For hydrogen and deuterium discharges the temperature was determined using a 100 mm x 20 mm PET crystal of eccentricity 0.806 placed at a focal length of 65 cm from the Plasma Focus pinch. The energy bands selected for this application were 1468 eV ( $\pm 5$  eV) and 1670 eV ( $\pm 6$  eV). The spectrometer was independently calibrated using a foil filter technique (filtered detectors mounted at the end of a 4 m collimating tube) and a second crystal spectrometer (flat PET crystals at 1592 eV and 2006 eV). The relative efficiencies of the PIN diode detectors were also determined employing the long collimating tube to view the same region of the plasma pinch during a series of calibration discharges.

The temperature obtained using this technique is very nearly the maximum temperature obtained at the most dense part of the pinch, as it develops as a function of time. In fact the linear dependence of the bremsstrahlung radiation intensity with the square of the density heavily weighs the most dense regions of the pinch, since the radiation is averaged over the viewed emitting region.

### III b.) Experimental Results

#### Scaling of $h$ and $r_0$

The experimental scaling and magnitude of  $h$  and  $r_0$  for the Illinois DPF as a function of plasma current and filling pressure are shown in Figs. 7 to 10. As

can be seen, the power law least squares fits to the data reveal that  $h$  depends on the plasma current,  $I$ , and filling pressure  $p_0$  as:

$$h \propto I^x p_0^y \quad \text{III 1)}$$

where  $x = -0.02 \pm 0.12$  and  $y = 0.26 \pm 0.13$

The dependence of plasma radius,  $r_0$ , with these quantities as

$$r_0 \propto I^a p_0^b \quad \text{III 2)}$$

where  $a = -0.18 \pm 0.11$  and  $b = 0.2 \pm 0.03$

Thus within the uncertainties  $h$  and  $r_0$  have the same dependence on these quantities and hence are proportional to each other within the experimental error.

There is a shift between the current scaling value for  $r_0$  with  $r_0 = 1.7 \pm 0.2$  mm, and the pressure scaling value with  $r_0 = 1.26 \pm 0.8$  mm. Although within experimental uncertainties, the discrepancy may be due to slight differences in the camera alignment since these data sets were taken on two separate occasions. A typical value of  $r_0$  obtained from the Mach-Zehnder interferometer <sup>20</sup> (half-width half-maximum of the density profile) is  $1.5 \pm 0.1$  mm (Fig. 11), which is within the uncertainties of both sets of data obtained from the streak camera.

#### Relationship Between $v_r$ and $v_c$

The streak camera was lined up horizontally to view the region  $0.27 \pm 0.05$  cm above the top of the center electrode. The current flowing in the plasma was monitored by a magnetic-pickup loop whose center was 2.4 cm below the top of the center electrode and 3.4 cm from the device axis. Typical results are presented in Fig. 3 showing that the radial collapse velocity achieves a roughly



constant value. The results of the scaling of the radial velocity at a given radial position as a function of plasma current and filling pressure are shown in Figs. 12 and 13. For the scaling of  $v_r$  with current, the prediction of the "M" theory<sup>23</sup> adapted to the Illinois DPF<sup>24</sup> is also shown.

The results versus current do not go through zero as predicted by theory, according to which  $v_r$  should scale as:<sup>23</sup>

$$v_r = v_A / \sqrt{2} = \frac{\mu_0 I}{2 \pi r_A (2 \mu_0 m_i n_0)^{1/2}} \quad \text{III 3.)}$$

where  $v_A$  is the Alfven speed at the outer edge of the center electrode ( $r=r_A$ ),  $I$  is the plasma current,  $n_0$  is the fill density and  $m_i$  is the ion mass. The deviation of the data from the theory may be due to a velocity dependent drag of the current sheath on the anode but this is only speculation on our part.

$v_c$  was measured from the axial streak pictures (Fig. 5) and is plotted as a function of  $I$  and  $p_0$  in Figs. 14 and 15. To see if  $v_r$  and  $v_c$  are related we compare the least square fits to the data presented in Figs. 12 to 15.

For the dependence of  $v_r$  and  $v_c$  with plasma current the two data sets were fitted to a power law relationship, i.e.

$$v_r = B I^R \quad \text{III 4.)}$$

$$\text{and} \quad v_c = B_F I^F \quad \text{III 5.)}$$

where  $R = 0.71 \pm 0.07$ , and  $F = 0.78 \pm 0.07$

Thus within the uncertainties (less than 10%) these two velocities have the same dependence on the plasma current as would be expected in the zippering effect.

For the variation in pressure  $v_r$  and  $v_c$  were fit to a power law:

$$v_r \propto p_o^r \quad \text{III 6.)}$$

$$\text{and } v_c \propto p_o^c \quad \text{III 7.)}$$

where  $r = -0.41 \pm 0.04$ , and  $c = -0.46 \pm 0.04$

Thus within the 10% experimental uncertainties  $v_r$  and  $v_c$  have the same dependence on filling pressure.

#### Plasma Electron Temperature

The electron temperature is useful in calculating the speed of sound in the plasma for comparison with theory. The soft x-ray measurements involve an average over a few millimeters along the pinch column. For pure hydrogen or deuterium filling gases (Fig. 16), the electron temperatures<sup>22</sup> typically rises to 250eV at the peak of first compression, cools to about 200eV at the end of the radial expansion (about 16ns later) and rises back up to over 300eV during the peak of second compression (about 27ns after first compression).

The results presented in this section will be discussed in the following section.

#### IV) Discussion of Results

In this section the experimental results are summarized and then compared with theory. Since the stability period appears to be enhanced, two simple models are discussed which could account for such stability and still scale as

$r_0/v_s$ . Finally the  $\tau \approx a'_0/r_0$  scaling is compared to data from other devices to check its validity.

#### IVa) Summary of Experimental Results

From the discussion of section II it is seen that is  $h \propto r_0$  and that if  $v_c \propto v_r$ , the scaling would be consistent with the classical result that  $\tau \approx a'_0/v_s$ .  $h$  (the distance between the point the  $m=0$  stability occurs and the end of the pinched column) is a convenient parameter to measure from axial streak pictures. The experimental test of these relationships was to vary the plasma current,  $I$  and filling pressure (deuterium),  $p_0$ , over as wide a parametric range possible to see how each of these quantities varied with these parameters.

For variations of the pair  $h$  and  $r_0$  with  $p_0$ , and for variations of the pair  $v_r$  and  $v_c$  with both  $p_0$  and  $I$  the same scaling is found (see eqns. III 1 to III 7).

The  $v_r$  and  $v_c$  scaling with  $p_0$  and  $I$  give support to the zippering model of the relation between these two quantities.  $h$  scales the same way as  $r_0$  with  $I$  within the uncertainties which are large with respect to the mean value (eqn. III 1 and 2) but which are at most less than twice those of the  $v_r$ ,  $v_c$  data in the absolute sense. Since the mean values of the exponents are close to zero this merely implies that the dependence of  $h$  and  $r_0$  on  $I$  is weak. While this does not prove that  $h$  and  $r_0$  are related, the demonstrated correlation between  $v_c$  and  $v_r$  supports the classical scaling model:

$$\frac{h}{v_c} = \frac{a'_0 r_0}{v_r} = \tau \quad \text{IV 1)}$$

and the weak dependence of  $h$  and  $r_0$  with  $I$  is at least consistent with this.

Also the small but significant trend in the scaling of  $h$  and  $r_0$  with  $p_0$  (i.e.  $h \propto p_0^{0.26 \pm 0.13}$  and  $r_0 \propto p_0^{0.2 \pm 0.03}$ ) indicates that  $h$  and  $r_0$  are directly related.

$\alpha$ , the ratio  $h/r_0$ , is  $8.6 \pm 2.4$  experimentally and related to  $\alpha' = \tau v_s / r_0$  by (section II)

$$\alpha' = \alpha(\gamma/2)^{1/2}/f. \quad \text{IV 2.)}$$

where  $f = v_c/v_r$ .  $f$  is  $2.6 \pm 0.8$  for  $p_0$  variations and  $1.4 \pm 0.7$  for  $I_p$  variations making the mean value  $f \approx 1.9 \pm 0.9$ . Thus  $\alpha' \approx 4 \pm 2$  from the experimental results of  $h/r_0$  and  $v_c/v_r$  and this model.

This will be compared with  $\alpha'$  taken from other experimentally determined quantities and theoretical models for  $\alpha'$  in the next subsection.

#### IV b) Comparison of Experiment with Theoretical Models of the Sausage Instability in the Plasma Focus

In this section the classical Kruskal-Schwarzschild<sup>3</sup> theory for the sausage mode is applied to the pinch phase of the plasma focus and used to predict the growth rate and wavelength of the instability. Then three additional models for enhanced stability based on 1) the shape of the pinch, 2) axial flow of plasma, and 3) self-generated magnetic fields are also presented.

#### The Kruskal-Schwarzschild Theory

The classical mhd theory for the  $m=0$  mode in a plasma supported by a magnetic field against gravity; this is the well-known Kruskal-Schwarzschild instability.<sup>3</sup> If the gravitational acceleration vector,  $g$ , points away from the fluid the plasma is unstable and the growth rate of the instability,  $\Gamma$ , is related to the

wave number  $k$  by:

$$\Gamma = (kg)^{1/2} \quad \text{IV.3)}$$

for the case  $\vec{k} \cdot \vec{B} = 0$ . The gravitational acceleration vector pointing out of the plasma is equivalent to the plasma being accelerated by the magnetic field or a convex curvature of the magnetic field with respect to the plasma; the latter causes the centripetal acceleration vector of the fluid to point into the plasma.<sup>25</sup> Thus during first compression, the plasma is being decelerated by its own compression, the acceleration vector points out of the plasma, and hence is stable<sup>26</sup>. However toward the end of the radial expansion phase the plasma is being decelerated by the magnetic field and hence should be unstable.

Although equation IV.2 predicts an infinite growth rate as the wavelength of the perturbation approaches zero, two phenomena: finite ion gyroradius,  $\rho$  and finite density scale length,  $\eta^{-1}$ , can give a lower bound to the wavelength. When one considers the effect of field line curvature for a cylinder  $g$  can be given by:<sup>4</sup>

$$g = \kappa T / m_i r_0 \quad \text{IV.4)}$$

(here  $T$ ,  $m_i$  and  $r_0$  are the ion temperature, ions mass and the plasma radius respectively), one finds:<sup>27-28</sup>

$$\Gamma = \left( \frac{\kappa T}{m_i r_0} \eta \right)^{1/2} \sim 1/\tau \quad \text{IV 5.)}$$

for  $\rho = 0$ .

From our experiment during first compression, where  $p_0 = 3$  torr ( $D_2$ ),  $I = 550$  kA,  $T \sim 330$  eV<sup>29</sup>,  $r_0 \sim 1.5$  mm and  $\eta \sim (1.2 \pm 0.2 \text{ mm})^{-1}$  (Fig. 11)  $\tau \sim 1/\delta \sim 11 \pm 2$  ns. This compares with the experiments period between first and second compression of  $27 \pm 3$  ns so  $\alpha'$  for our experiment from the classical model is  $2.5 \pm 0.5$  which is consistent with the data from the  $h, r_0, v_c, v_r$  scaling results.

#### IV c) Effects of Curvature

During the radial collapse phase the plasma experiences an acceleration just prior to first compression (Fig. 3) which could cause  $m = 0$  modes. While perturbations in the current sheath are commonly observed during this period (indeed there is evidence of such in the upper right portion of the interferogram in Fig. 11), they don't cause a column disruption as in second compression. Since the column is concave during radial collapse it is possible that the growth of these perturbations is suppressed by curvature effects considered by Comisar<sup>30</sup>. Later, during the radial expansion phase, the plasma column is cylindrical near the midplane, so the effect of curvature would be reduced. Therefore some other mechanism must provide stability during this phase.

#### IV d.) Stability induced by Axial Flow

During first compression the plasma is stabilized by its own deceleration but during the radial expansion this mechanism is no longer effective. However there is considerable evidence of axial fluid flow during this phase which could provide stabilizing effects.

Besides the radial motion of the plasma during these phases, strong axial flow is also implicit due to the lack of confinement at the ends of the pinch. Downing and Eisner<sup>31</sup> using laser scattering during the pinch of a 15 kJ

Mather-type plasma focus observed a roughly constant density during the last stages of the radial collapse through first compression. Since the radial velocity was  $\sim 3 \cdot 10^7$  cm/sec during this period, an axial velocity of  $2.4 \cdot 10^8$  cm/sec was implied to conserve particles. They also analyzed other laser scattering observations of the plasma focus<sup>32,33</sup> and concluded high axial velocities were probably present in these devices as well. Also there is evidence of high velocity ( $\sim 10^8$  cm/sec) axial flow from x-ray framing camera pictures.<sup>34</sup> The presence of a high axial velocities during the first compression and radial expansion phases is supported by computer simulations of these phases as well.<sup>35-37</sup>

In our device, evidence of high speed axial flow can be seen in the rapid decrease in particle number per unit length,  $N$ , during the three phases of the pinch as measured using the Mach-Zehnder interferometer. The interferograms reveal that for the standard case:  $p_0 = 3$  torr deuterium and  $I = 550$  kA,  $N$  falls from about  $10^{18}$ /cm at first compression to  $\sim 6 \cdot 10^{17}$ /cm during the radial expansion and down to  $10^{17}$ /cm during second compression. Thus the rate of decay of  $N$  is roughly constant of over this period.

Taking a simple axial outflow model:

$$\ell \frac{dN}{dt} = 2Nv_Z \quad \text{IV 6.)}$$

where  $\ell$   $v$  are the length of the pinch area and the axial flow velocity respectively. Since  $\ell = 2h$  and taking an average  $h \sim 1$  cm during radial expansion, one finds  $v_Z \sim 6 \cdot 10^7$  cm/sec for the entire pinch period.

The stability critirion may be expressed<sup>38</sup> by  $v_Z > v_A$ ; perturbations are swept at out of the column before they can grow. However as the mass flows

out the ends,  $v_A$  increases until the instability is triggered. For  $I \sim 550\text{kA}$  and  $p_0 \sim 3$  torr, analysis of the interferograms reveals that  $v_A \sim 4.6 \cdot 10^7$  cm/sec at the time of second compression. The speed of sound on the other hand, since 200eV, is  $\sim 1.4 \cdot 10^7$  cm/sec through out the pinch phase, thus the flow is supersonic with a Mach number of  $\sim 4$ .

In this model the stable period scales as a loss time for mass  $\tau_f$ :

$$\tau_f = h/v_Z$$

Theoretically  $v_Z$  can be related to  $v_r$  as follows. Because of particle conservation during the radial collapse, the axial flow velocity  $v_Z$  for a cylinder of length  $l$  and radius  $r$  would be  $\sim l v_r / r$  where  $v_r$  is the radial velocity. This flow velocity appears to persist well into the radial expansion phase. This may be seen theoretically as follows: If one assumes potential flow, then Bernoulli's equation holds and one has:

$$p/\rho + 1/2 v_Z^2 = \text{constant} \quad \text{IV 7.)}$$

The first term in IV 7.) is just  $v_s^2/\gamma$ , where  $\gamma$  is the ratio of specific heats. Since, as shown above,  $v_s \ll v_Z$ ,  $v_Z$  would be approximately constant during the entire pinch as consistent with the above discussion.

From these considerations appears that  $v_A \leq v_Z$  during radial expansion, but this reverses at 2nd compression due to mass loss. The scaling, since  $v_Z \propto v_r$  would be essentially classical:

$$\tau \sim h/v_Z \sim \frac{\alpha r_0}{(l/r) v_r} \sim \alpha' \frac{r_0}{v_s} \quad \text{IV 8.)}$$



with about the enhancement factor,  $\alpha' = \alpha / \left( \frac{\gamma}{2} \right)^{1/2} \frac{1}{\bar{r}}$  being somewhat smaller ( $\sim 2.6$ ) since  $v_Z \gtrsim v_c$ . Thus this model also appears to give results consistent with the data.

#### IV e) Enhanced Stability from a Self Generated Magnetic Field

A self generated axial magnetic field could provide column stability. The addition of an external axial magnetic field has been shown to provide stability to the plasma focus;<sup>39</sup> the elementary theory of the Kruskal-Schwarzschild instability<sup>25,40</sup> also supports this. Filamentary structures, observed in the discharge from the beginning<sup>41,42</sup> and found in the pinch<sup>43</sup> could be force-free configurations<sup>44</sup> hence providing an axial magnetic field. Evidence for such a field has been reported from measurements using magnetic pick-up loops<sup>41,45</sup> and Faraday rotation.<sup>46</sup> However in ref. 41 the filamentary fields were found to alternate between inwardly and outwardly pointing radial fields during the rundown phase whereas in ref. 45 they were found to point only in one direction radially. Also in ref. 42 the filamentary structures were reported to disappear later in the discharge whereas in ref. 41 they were reported to persist into all phases. Thus the nature of filamentary structures is somewhat ambiguous.

A possible model to take into account the magnetic shear introduced by the axial magnetic field of such filaments could be as follows. The shear limits the wave number of the maximum growth rate,  $k_{MAX}$  to be<sup>25</sup>:

$$k_{MAX} = \frac{kT}{m_i r_o} \frac{\mu_o \rho_o}{2 B_z^2} \quad \text{IV 9.)}$$

where  $B_z$  is the axial magnetic field. Assuming  $\beta = 1$ , the wavelength of the maximum growth rate,  $\lambda_{MAX}$ , is now given by:

$$\lambda_{MAX} = \frac{16 \pi r_o B_z^2}{B_\phi^2 - B_z^2} \quad \text{IV 10.)}$$

where  $B_\phi$  is the azimuthal magnetic field.

As the column lengthens the instability would occur, when:

$$L = 2h > \lambda_{MAX}/2 \quad \text{IV 11.)}$$

or

$$h > \frac{4 \pi r_o B_z^2}{B_\phi^2 - B_z^2} \quad \text{IV 12.)}$$

For comparison with our experiment,  $\alpha = h/r_o \sim 8.6$ ,  $B_z/B_\phi \sim 0.6$ . The magnitudes of the  $B_r$  and  $B_z$  and  $B_\phi$  magnetic fields reported in ref. 41,45 and 46 would make  $B_z/B_\phi$  of this order or greater so this effect cannot be ruled out. However, the observed wavelength of the instability is at least an order of magnitude smaller than  $\lambda = 4h$  as predicted by the model, possibly due to its simplicity. This model is only presented here as an illustration of one effect filamentary structures could have on stability. A more sophisticated treatment<sup>44</sup> is beyond the scope of this work.

Computer simulations of the plasma focus dynamics using a two-fluid model reveal<sup>47</sup> that current filamentation should occur in the pinch phase which could explain the structures observed by Sadowski et al.<sup>43</sup> and provide a stabilizing  $B_z$  as well. The results of these simulations also show that the period of stability

should scale as the plasma current,  $I$ , to the three-halves power.<sup>47</sup> Because of the complicated nature of these calculations, it is not obvious that there is a single mechanism involved in the enhanced stability.

IV f) Comparison of the Empirical Scaling with the Results from other Mather-type Plasma Focus Devices.

So far evidence has been presented to indicate that  $h = \alpha r_o$  and  $\tau = \alpha' r_o / v_r$  in our Mather-type plasma focus but is this result unique to this device? Since the scaling is classical, enhanced by a factor of  $\alpha'$ , it seems reasonable that it should apply to other DPFs. We have gathered data on pinch current, fill pressure (i.e. equivalent in mass density of that of pure deuterium), pinch radius, and  $\tau$  from the literature and scaled  $v_r \propto I^{0.745} / p_o^{0.435}$  where the exponents are the mean values from our  $v_c$ ,  $v_r$  data to be consistent with the zippering effect.

The results are shown in Table IV 1.) and Fig. 17. The scaling relations for the stability period is given by

$$\tau_s = \tau_{\epsilon} \frac{r_o}{r_{o\epsilon}} \left[ \frac{I_{\epsilon}}{I} \right]^{0.745} \left[ \frac{p_o}{p_{o\epsilon}} \right]^{0.435} \quad \text{IV 13.)}$$

where the quantities subscripted by  $\epsilon$  are those for our device (U. of I.) and are listed in Table VI 1.) along with those parameters from the other devices. The data follow the linear-least square fit fairly well with less than a 20% uncertainty in the slope ( $1.3 \pm 0.2$ ). All those listed but the Frascati device have hollow cathodes which could effect  $v_r$  if drag on the center electrode is an important effect. That is, with a hollow cathode, the drag force is farther away from the constricting region during collapse than with a solid anode and hence the effects of drag would be reduced. This could explain the deviation of the Frascati point (F) from the  $\tau_x = \tau_s$  line but not that of the Poseidon point (P). In any case the agreement with a linear relationship between  $\tau_s$  and  $\tau_x$  is evidence that the

scaling relation IV 13.) is on the right track. The values of  $h_s$  were scaled simply from:

$$h_s = h_e \left[ \frac{r_o}{r_e} \right] \quad \text{IV 14.)}$$

however fewer values of  $h_x$  can be found in the literature (Table IV 1). However, those that are found are in fair agreement with the predictions of IV 14. Thus this enhanced classical scaling appears to hold for several other Mather-type plasma focus devices as well.

Although the scaling equations IV 13.) and IV 14. are useful to test consistency between devices, they are not very useful in design since one has to know  $r_o$  before one can predict  $\tau$ . If, however, one plots  $r_o$  versus  $r_A$ , the anode radius, for the same devices of Table IV 1.) one finds (Fig. 18):

$$r_o = (6 \pm 1.6) \cdot 10^{-2} r_A^{1.3 \pm 0.2} \quad \text{IV 15.)}$$

both  $r_o, r_A$  in cm.

If the radial collapse phase were adiabatic and one-dimensional, one would predict: (since  $V \propto r^2$ )

$$r_o/r_A = \left[ \frac{T_A}{T_o} \right]^{\frac{1}{2(\gamma-1)}} \quad \text{IV 16.)}$$

Since it has been noted that the pinch temperatures  $T_0$  do not change significantly over a wide range of devices<sup>55</sup>, the near linearity between  $r_0$  and  $r_A$  is not too surprising.

Thus it appears one could use the scaling relation IV 15.) along with IV 13.) and IV 14.) to predict  $\tau$  and  $h$  for a given design. However due to the scatter in the data, (the uncertainties in these predictions approach 50 percent) only rough estimates can be obtained and the relations strictly apply only to devices with a hollow anode.

Finally the empiracle scaling of  $\tau$  with  $I$  from eqn. IV 13.) would appear to be at odds with the four-fluid model developed at the University of Stuttgart which predicts<sup>47</sup>  $\tau \propto I^{3/2}$ . However, if  $r_0$  is plotted verses  $I$  for the various devices listed in table IV 2.) one finds that:

$$r_0 \propto I^{1.44 \pm 0.2} \quad \text{IV 17.)}$$

from a least-square power law fit so the overall empiracle scaling is:

$$\tau = \frac{\alpha r_0}{v_r} \propto I^{0.7 \pm 0.3} p_0^{0.435 \pm 0.04} \quad \text{IV 18.)}$$

While this is still not within the experimental uncertainties of the computational results<sup>47</sup>, the disagreement is not nearly as severe as IV 13.) would indicate.

Table IV 1  
Scaling of  $h$  and/or  $\tau$  to other Mather-type  
Plasma Experiments Focus Devices: Comparison  
with Experiments

Location of Device	$r_A$ (cm)	$I$ (kA)	$p_0$ (torr)	$r_0$ (cm)	Exp	Exp	Empirical Scaling	
					$\tau$ (ns)	$h$ (cm)	$\tau$ (ns)	$h$ (cm)
U. of Illinois	2.5	550	3.0	0.15	27	1.3	27	1.3
Frascati <sup>14,46</sup>	8.0	1300	3.0	1.0	130	—	95	8.7
Stuttgart								
Poseidon <sup>10,45,48</sup>	6.7	1200	2.3	0.78	100	—	70	6.8
Nessi <sup>49</sup>	3.3	290	1.5	0.15	40–60	2	32	1.3
Swierk <sup>50†</sup>	5.0	1000	"	0.38	75	2–2.5	71	3.3
Darmstadt <sup>52,53</sup>	0.8	200	2.6*	0.04	16	0.25	14.4	0.35
Stevens <sup>54</sup>	1.7	400–500	8	0.2	60±20	1.0–1.5	64±6	1.7

\* Equivalent pressure in deuterium of 4 torr  $H_2$  + 4% Ar in terms of mass density

† Earlier data reported from Swierk<sup>51</sup> gave a somewhat greater plasma radius as measured using a streak camera. The data reported in ref. 50 are taken from Schlieren pictures and laser interferograms and hence are more accurate.

## VI Conclusions

The experimentally observed constancy of the ratio of the distance between first and second compression along the axis of the pinch,  $h$ , and the minimum plasma radius,  $r_0$ , is evidence that the stability of the Mather-type plasma focus is behaving in a manner as predicted by ideal MHD theory. The scaling of these parameters with plasma current and filling pressure are reported here for the first time. Although the ratio  $\alpha = h/r_0$  is about a factor of three above that predicted for a straight cylinder, two simple models, both consistent with ideal MHD theory, can be used to explain this enhancement. The models include either the effect of axial flow, or the effect of a self-generated axial magnetic field. However neither of these models is necessarily unique.

The empirical scaling laws developed from the experimental results found in this experiment were used to predict both  $h$  and the period of stability  $\tau$  in other plasma focus devices. The agreement between the scaled parameters and those reported from the other experiments (table IV 1) indicates that the empirical scaling relations for  $h$  and  $\tau$  found ~~in~~ this study could be used to predict the performance of other devices. Thus if enhanced stable lifetime of the pinch is desired at higher plasma currents, one could design a device with an anode of larger radius (egns. IV 13-15).



# References

1. J. W. Mather, Methods of Exp. Physics 9B, (Academic Press, 1971) 187.
2. N. V. Filippov, T. I. Filippova, and V. P. Vinogradov, Nucl. Fusion Suppl. Pt. 2, 577 (1962).
3. M. Kruskal and M. Schwarzschild, Proc. Phys. Soc. (London) A223, 348 (1954).
4. R. J. Tayler, Proc. Phys. Soc. (London) B70, 31 (1957).
5. M. G. Haines, Phil. Trans. R. Soc. (London) A300, 649 (1981).
6. P. Choi, A. E. Dangor, A. Folkiński, E. Kahan, D. E. Potter, P. D. Slade and S. J. Webb, Plasma Phys. and Control. Nucl. Fusion Res. 1978, Vol. 2, 69 (Vienna, IAEA, 1979).
7. M. G. Haines, A. E. Dangor, A. Folkiński, P. Baldock, W. G. Bessell, D. J. Bond, C. D. Challis, P. Choi, M. Coppins, M. B. Favre-Dominquez, D. A. Hammer, E. L. Lindman, J. R. Liu, G. Nave, O. G. Parfenov, G. Rickard, and J. Westlake, Plasma Phys. and Control. Nucl. Fusion Res. 1984, Vol. 2, 647 (Vienna, IAEA, 1985).
8. T. Oppenlaender, G. Pross, G. Decker and M. Truck, Plasma Phys. 19, 1075 (1977).
9. D. L. Jassby, Trans. Amer. Nucl. Soc. 30, 61 (1978).
10. H. Herold, L. Bertalot, K. Hirano, U. Jaeger, H. J. Kaeppler, M. Sadowski, H. Schmidt, R. Schmidt, M. Shakhatre, A. Shyam, G. Boeckle, K. Matl, N. Wenzel, R. Wolf, R. Baetzner, H. Hinsch, K. Huebner in Plasma Physics and Controlled Nuclear Fusion Research 1984 (Proc. 10th Int. Conf. London, 1984), Vol.2, 579 (IAEA, Vienna, 1985).
11. M. Howells, J. Kirz, D. Sayre, and G. Schmahl, Phys. Today, 39 [8] 22 (1985).
12. F. Venneri, H. Krompholz, J. Mandrekas, G. Gerdin, and M. Tanis, Bult. Am. Phys. Soc. 28, 1171 (1983).
13. J. W. Long, N. J. Peacock, P. D. Wilcock, and R. J. Speer, Paper C5, Proc. Amer. Phys. Soc. Topical Conf. on Pulsed High-Density Plasmas, Los Alamos Rep. LASL-3770 (Sept. 1967). Also N. J. Peacock, M. G. Hobby and P. D. Morgan in Plasma Phys. and Control Nucl. Fusion Res. 1971 (Proc. 4th Int. Conf., Madison, 1971), Vol 1, 537 (IAEA, Vienna, 1971).
14. J. P. Rager, L. E. Bilbao, H. A. Bruzzone, C. Gouylan, U. Guidoni, H. Kroegler, S. Podda, B. V. Robouch, and K. Steinmetz, in Plasma Physics and Controlled Fusion Research 1980 (Proc. 8th Int. Conf. Brussels, 1980), Vol. 2, 209 (IAEA, Vienna 1981).

15. S. Czekai, S. Denus, A. Kasperczuk, R. Miklaszewski, M. Paduch, T. Pisarczyk, and Z. Wereszczynski, Proc. 4th Int. Workshop on Plasma Focus and Z-Pinch Research, Warsaw, Sept. 1985 (Inst. Plasma Phys. and Laser Microfusion, Warsaw, 1986) 124.
16. V. V. Vikrev, Sov. J. Plasma Phys. 3, 539 (1977).
17. W. W. Hsing, J. L. Porter, B. A. Hammel, D. L. Hanson, M. A. Palmer and A. Widman, IEEE Int. Conf. on Plasma Sci., Arlington, VA, 1987, Conf. Record-Abstracts, IEEE Catalog No. 87CH2451-3, 22 (1987).
18. W. H. Bostick, L. Grunsberger, V. Nardi, and W. Prior, Proc. 5th Symp. on Thermophysical Properties, (Amer. Soc. Mech. Eng., Ed. C. F. Bonilla, New York 1970), 495.
19. W. Stygar, G. Gerdin, F. Venneri, and J. Mandrekas, Nucl. Fusion 22, 1161 (1982).
20. K. Boulais, M. S. Thesis, Electrical Engineering. Dept., University of Illinois Urbana-Champaign, 1987.
21. B. L. Henke, H.T. Yamada, and T.J. Tanaka, Rev. Sci. Instr. 54, 1311 (1983).
22. F. Venneri and G. Gerdin, IEEE Int. Conf on Plasma Sci., Arlington, VA, 1987, Conf. Record-Abstracts, IEEE Catalog No. 87CH2451-3, 44 (1987).
23. M. Rosenbluth's "M" theory is described in J. D. Jackson, Classical Electrodynamics (J. Wiley, 1962), 322.
24. J. Mandrekas, M. S. Thesis, Nucl. Eng. Program, University of Illinois Urbana-Champaign, 1984.
25. G. Schmidt, The Physics of High Temperature Plasmas (Academic Press, 2nd Ed., 1979) 126
26. F. L. Curzon, A. Folkierski, R. Latham, and J. A. Nation, Proc. Roy. Soc. (London) A257, 386 (1960).
27. Rosenbluth, N. A. Krall, and N. Rostoker, Nucl. Fus. 1962 Suppl. Part I, 143 (IAEA, Vienna, 1963).
28. K. V. Roberts and J. B. Taylor, Phys. Rev. Lett 8, 197 (1962).
29. Taking  $T_i = 4/3 T_e$  which is the result from laser scattering measurements on a plasma focus during the pinch phase where the gas fill was pure deuterium: M.J. Forrest and N.J. Peacock, Plasma Phys 16, 489 (1974).
30. G. G. Comisar, Phys. Fluids 12, 1000 (1969).
31. J. N. Downing and M. Eisner, Phys. Fluids 18, 991 (1975).
32. J. P. Baconnet, G. Cesari, A. Coudeville and J. P. Watteau, Phys. Lett 29A, 19 (1969).

33. A. Bernard, A. Coudville, J. P. Garconnet, A. Jolas, J. De Mascureau and J. P. Watteau, *Phys. Lett* 35A, 7 (1971).
34. V. I. Agafonov, G. V. Golub, L. G. Golubchikov, V. F. D'yachenko, V. D. Ivanov, V. S. Imshennik, Yu. A. Kolesnikov, E. B. Svirsky, N. V. Filippov and T. I. Filippova, *Nucl. Fusion Spec. Suppl.* 1969, *Plasma Phys. and Control Nucl. Fusion Res.*, 121 (IAEA, Vienna, 1969).
35. V. F. D'yachenko and V. S. Imshennik, *Sov. Phys. JETP* 29, 947 (1969).
36. D. E. Potter, *Phys. Fluids* 14, 1911 (1971).
37. V. F. D'yachenko and V. S. Imshennik, "Two-Dimensional Magnetohydrodynamic Model, for the Dense Plasma Focus of a Z Pinch," *Rev. of Plasma Physics* 8, (Consultants Bureau, Ed. M. A. Leontovich, 1980). 199 (1974).
38. N. V. Filippov, V. D. Ivanov, M. P. Moiseeva, M. M. Stepanenko and M. K. Sukhareva, *Nucl. Fusion Suppl.* 1975, *Plasma Phys. and Control. Nucl. Fusion Res. Conf. Proc.* (Engl. transl. to Russian papers) 5th Int. Conf. Tokyo 1974, 163 (IAEA, Vienna, 1975).
39. J. W. Mather, P. J. Bottoms, J. P. Carpenter, A. H. Williams, and K. D. Ware, *Phys. Fluids* 12, 2343 (1969).
40. O. A. Anderson, W. R. Baker, S. A. Colgate, J. Ise, and R. V. Pyle, *Phys. Rev.* 110, 1375 (1958).
41. W. H. Bostick, W. Prior, L. Grumberger, and G. Emmert, *Phys. Fluids* 9, 2078 (1966).
42. J. W. Mather and A. H. Williams, *Phys. Fluids* 9, 2080 (1966).
43. M. Sadowski, H. Harold, H. Schmidt and M. Shakhatre, *Phys. Lett* 105A, 117 (1984).
44. V. Nardi, *Phys. Rev. Lett.* 25, 718 (1970).
45. F. Gratton, see ref. 5.
46. J. P. Rager, *Proc. 10th European Conf. on Plasma Phys. and Cont. Fusion Res.* (Moscow, Sept. 1981).
47. H. Herold, L. Bertalot, R. Deutsch, W. Grauf, U. Jaeger, H. J. Kaeppler, F. Lepper, T. Oppenlaender, H. Schmidt, R. Schmidt, J. Schwarz, K. Schwoerer, M. Shakhatre, A. Hayd, M. Maurer, P. Meinke, in *Plasma Phys. and Contr. Nucl. Fusion Res* 1982 (Proc. 9th Int. Conf. Baltimore, 1982), Vol. 2, 405 (IAEA, Vienna 1983).
48. H. Schmidt and Poseidon-team, *Proc. of the 3rd Int. workshop on Plasma Focus Res.*, *Plasma Res. Institute, Univ. of Stuttgart Rep.* (IPF-83-6, Sept. 1983) 63.

49. G. Decker, B. Nahrath, T. Oppenlaender, G. Pross, B. Rueckle, H. Schmidt, M. Shakhatre and M. Trunk, in Plasma Phys. and Control. Nucl. Fusion Res. 1976 (Proc. 6th Int. Conf. Berchtesgaden, 1976) Vol. 3, 441 (IAEA, Vienna, 1976).
50. A. Jerykiewicz, M. Bielik, L. Jakubowski, Z. Jankowicz, K. Kociecka, J. Kucinski, E. Rydygier, M. Sadowski, J. Zebrowski, M. Borowiecki, S. Czeka, S. Denus, A. Kasperczuk, M. Paduch, T. Pisarczyk, W. Skrzeczanowski in Plasma Phys. and Contr. Nucl. Fusion Res 1984 (Proc. 10th Int. Conf. London 1984), Vol. 2, 591 (IAEA, Vienna, 1985).
51. A. Jerzkiewicz, M. Bielik, Z. Jankowicz, K. Kociecka, L. Kocinski, J. Kucinski, B. Lipinski, M. Sadowski, J. Witkowski, W. Wyszynski, M. Borowiecki, S. Czeka, S. Denus, W. Skrzeczanowski, Proc. of the 3rd Int. Workshop on Plasma Focus Res., Plasma Res. Institute, Univ. of Stuttgart Rep. (IPF-83-6, Sept. 1983) 119.
52. R. Haas, H. Krompholz, L. Michel, F. Ruehl, K. Schoenbach, and G. Herziger Phys. Lett. 88A, 403 (1982).
53. K. H. Schoenbach, L. Michel and Heniz Fischer, Applied. Phys. Lett. 25, 547 (1974).
54. W. H. Bostick, V. Nardi, and W. Prior, Proc. Conf. on Cosmic Plasma Phys. 175 (ed. Karl Schindler, Plenum Press, N. Y., 1972).
55. J. P. Rager, private communication, 1984.

### Figure Captions

- Fig. 1 Schematic of a Mather-type plasma focus showing the successive positions of the current sheet and the pinch plasma at the end of the center electrode.
- Fig. 2 The relationship between the radial velocity and the apparent vertical speed of first compression. If the shape of the current sheath and the radial velocity prior the arrival on the axis are held constant in space and time first compression would appear to move along the axis as in b). The relationship between radius and height of the current sheath is taken to be hyperbolic.
- Fig. 3 A comparison between the predictions of "M" theory<sup>23,24</sup> and experimental observations using radial streak pictures and magnetic pickup loops. The width of the vertical bars on the data are the experimental ranges of uncertainty.
- Fig. 4 Alignment of the slit for the streak camera for the z streak pictures.
- Fig. 5 Examples of z streak camera pictures (top and middle) and the corresponding  $dI/dt$  waveform.  $h$  the distance between first and second compression when second compression occurs is defined in the middle figure.
- Fig. 6 Elliptical curved crystal spectrometer used to determine the electron temperature. The plasma column is at one focus of the ellipse and the cross over point at the other. Pin diodes on the detection circle are used to detect different spectral bands of the soft x-ray emission.
- Fig. 7 The dependence of  $h$  (Fig. 5) on plasma current. The deuterium filling pressure was 3.0 torr.
- Fig. 8 The dependence of  $h$  (Fig. 5) on deuterium filling pressure. The initial energy on the capacitor bank was 12kJ.
- Fig. 9 The dependence of the minimum plasma radius,  $r_0$ , on plasma current. The deuterium filling pressure was 3.0 torr.
- Fig. 10 The dependence of the minimum plasma radius,  $r_0$ , on plasma current. The initial energy on the capacitor bank was 12kJ.
- Fig. 11 Top: Typical interferogram of the first compression phase obtained from the nitrogen laser interferometer ( $\lambda=337$  nm,  $\Delta\tau<5$ ns). Bottom: Abel inversion of interferogram yields this electron density distribution.<sup>20</sup>

- Fig. 12 The radial velocity during the collapse phase at a radius of 1.1 cm and a filling pressure of 3 torr  $D_2$  as a function of plasma current. The dashed line and solid line are the least-squares power-law fit to the data and the predictions of "M" theory<sup>23,24</sup> respectively.
- Fig. 13 The radial velocity during the collapse phase at a radius of 0.8cm and a bank energy of 12kJ as a function of deuterium filling pressure.
- Fig. 14 Apparent axial speed of first compression about 1 cm above the midplane as a function of plasma current. The deuterium filling pressure was 3.0 torr. The line is a least squares power fit to the data.
- Fig. 15 Apparent axial speed of first compression about 1 cm above the midplane as a function of deuterium filling pressure. The initial energy on the capacitor bank was 12kJ.
- Fig. 16 Typical time dependence of the electron temperature of the pinched plasma obtained with the curve crystal spectrometer for  $p_0 = 3$  torr (deuterium) and  $I = 550$ kA. Comparison with simultaneous laser interferograms<sup>20</sup> indicates the first peak corresponds to first compression, the dip to radial expansion and the second peak to second compression.
- Fig. 17 A comparison of the experimental period of stability,  $\tau_x$ , with that predicted from eqn. IV 16.). The solid line is the least squares linear fit to the data Key: F = Frascati, P = Stuttgart Poseidon, N = Stuttgart Nessi, D = Darmstadt, St = Stevens Inst., Sw = Swierk, and I = Univ. of Illinois (Table IV-1).
- Fig. 18 A plot of the final pinch radius,  $r_0$  versus the radius of the anode,  $r_A$ , for the devices listed in Table IV-1. The line is the least squares power law fit to the data.

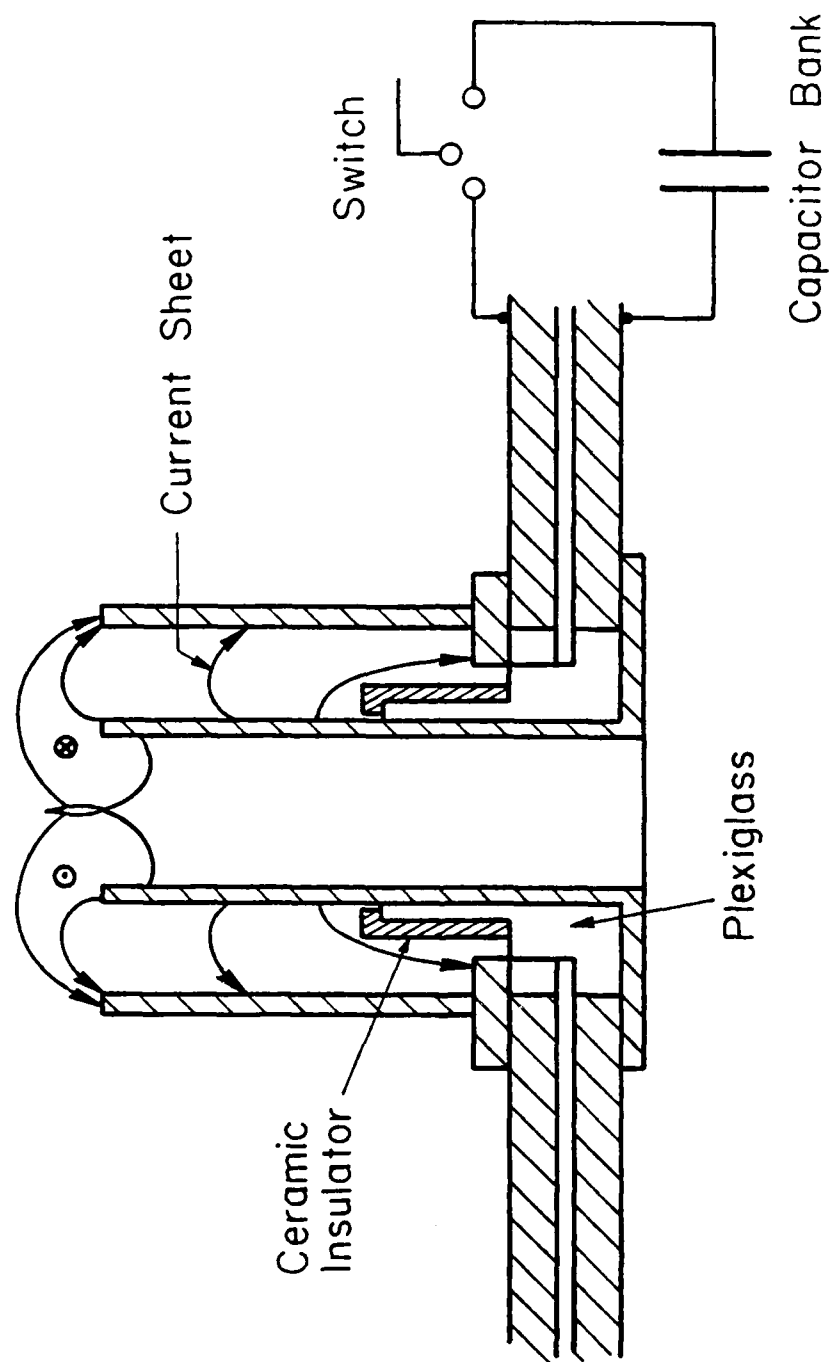


Figure 1

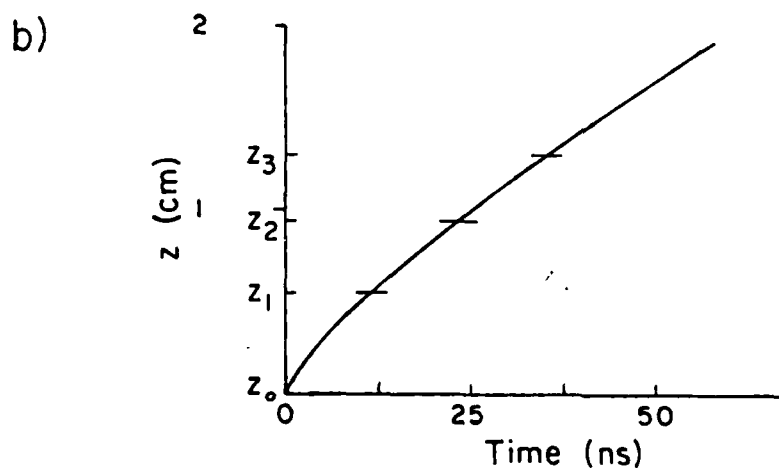
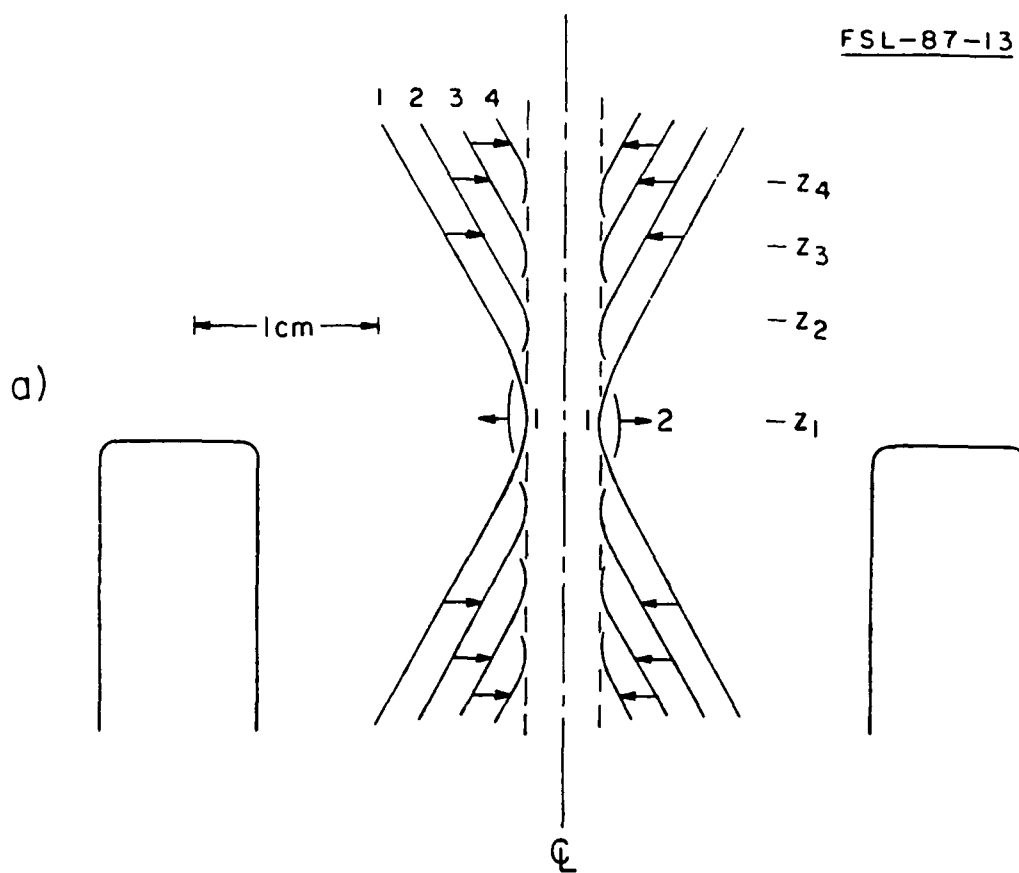


Figure 2



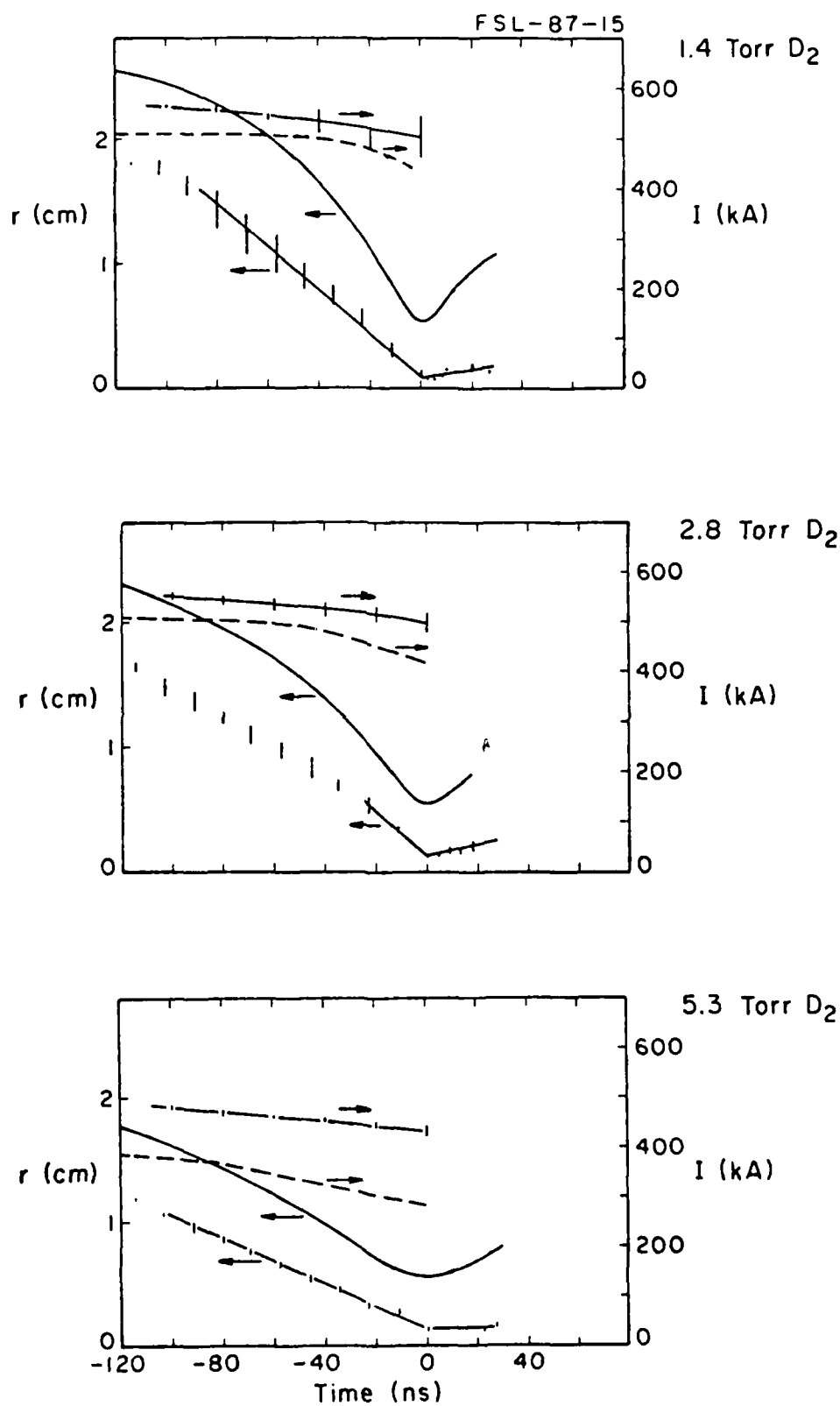
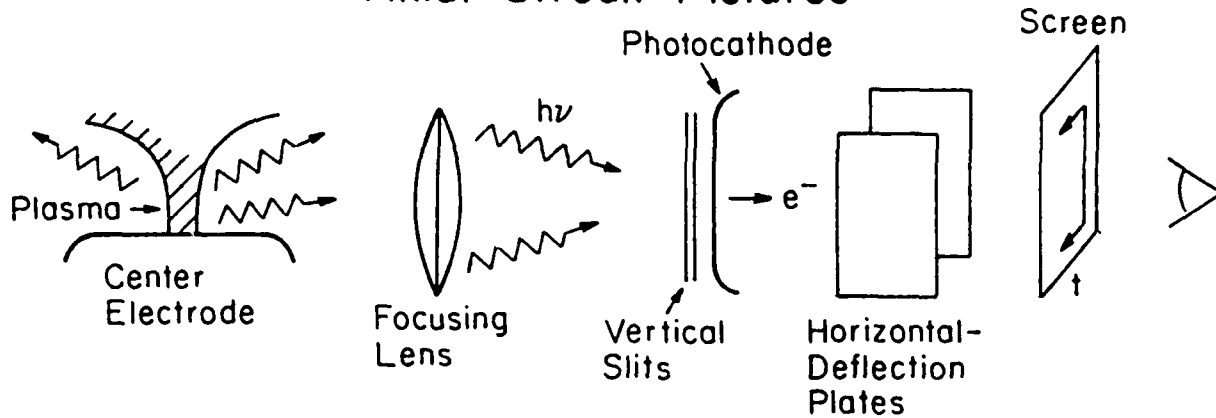
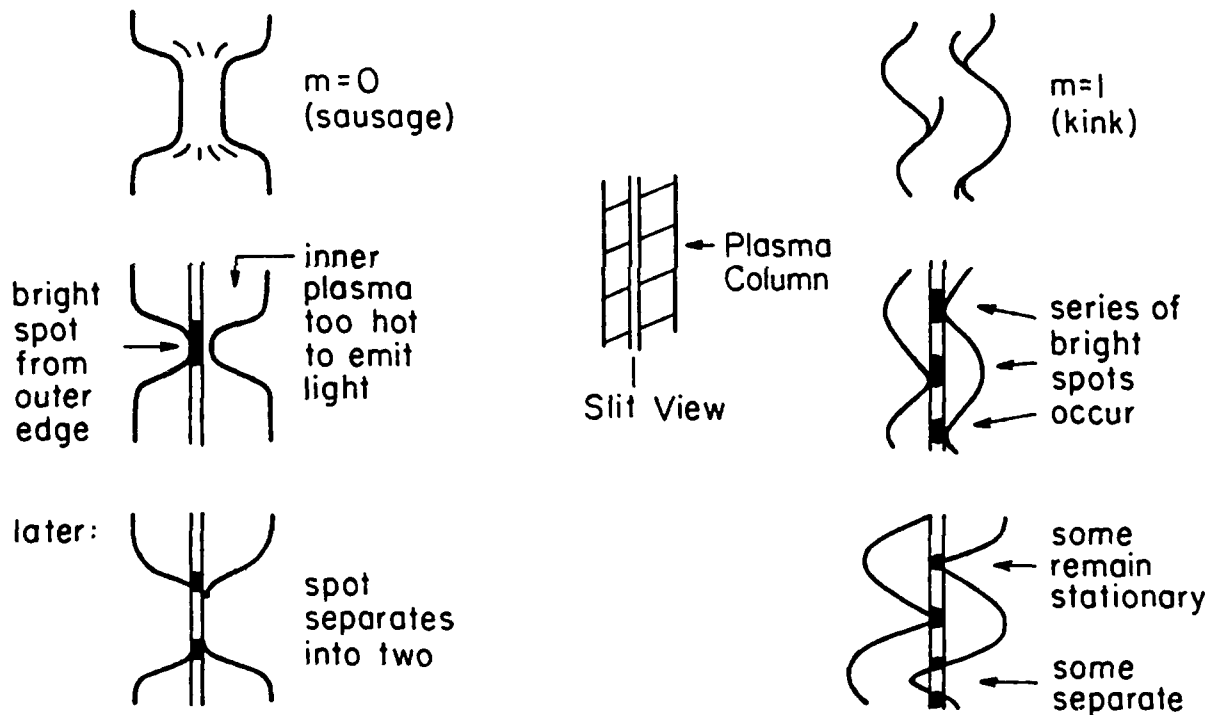


Figure 3

# Axial Streak Pictures



## mhd instabilities:



## view on screen:

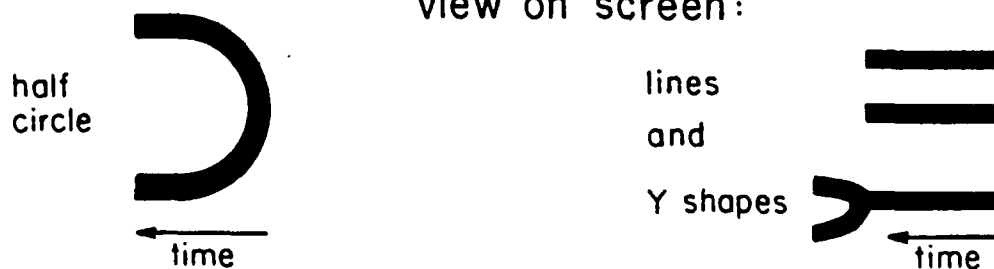
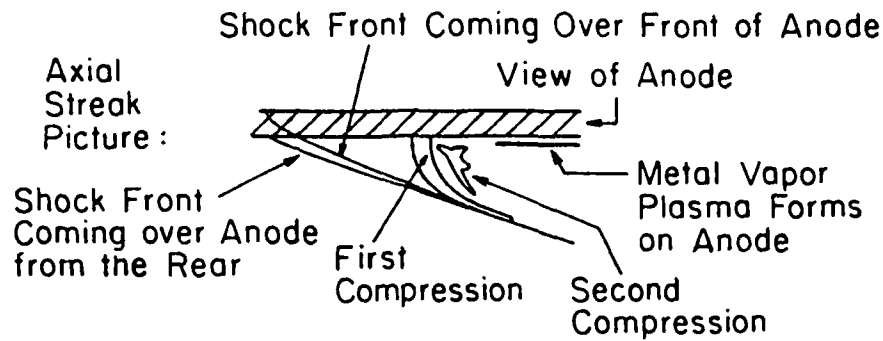


Figure 4

## Current Waveforms and Axial Streak Pictures



time →

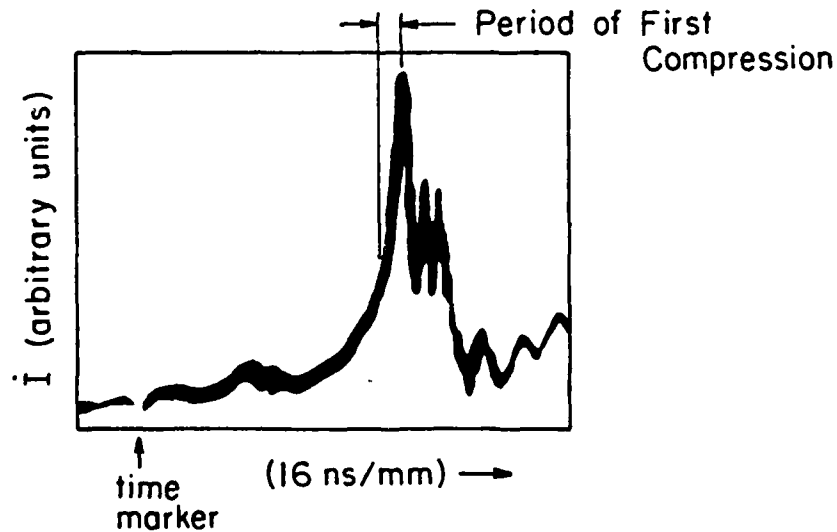
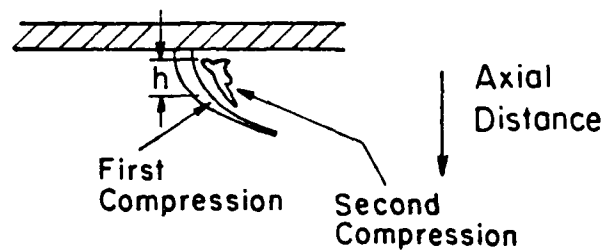
Definition of  $h$ :

Figure 5

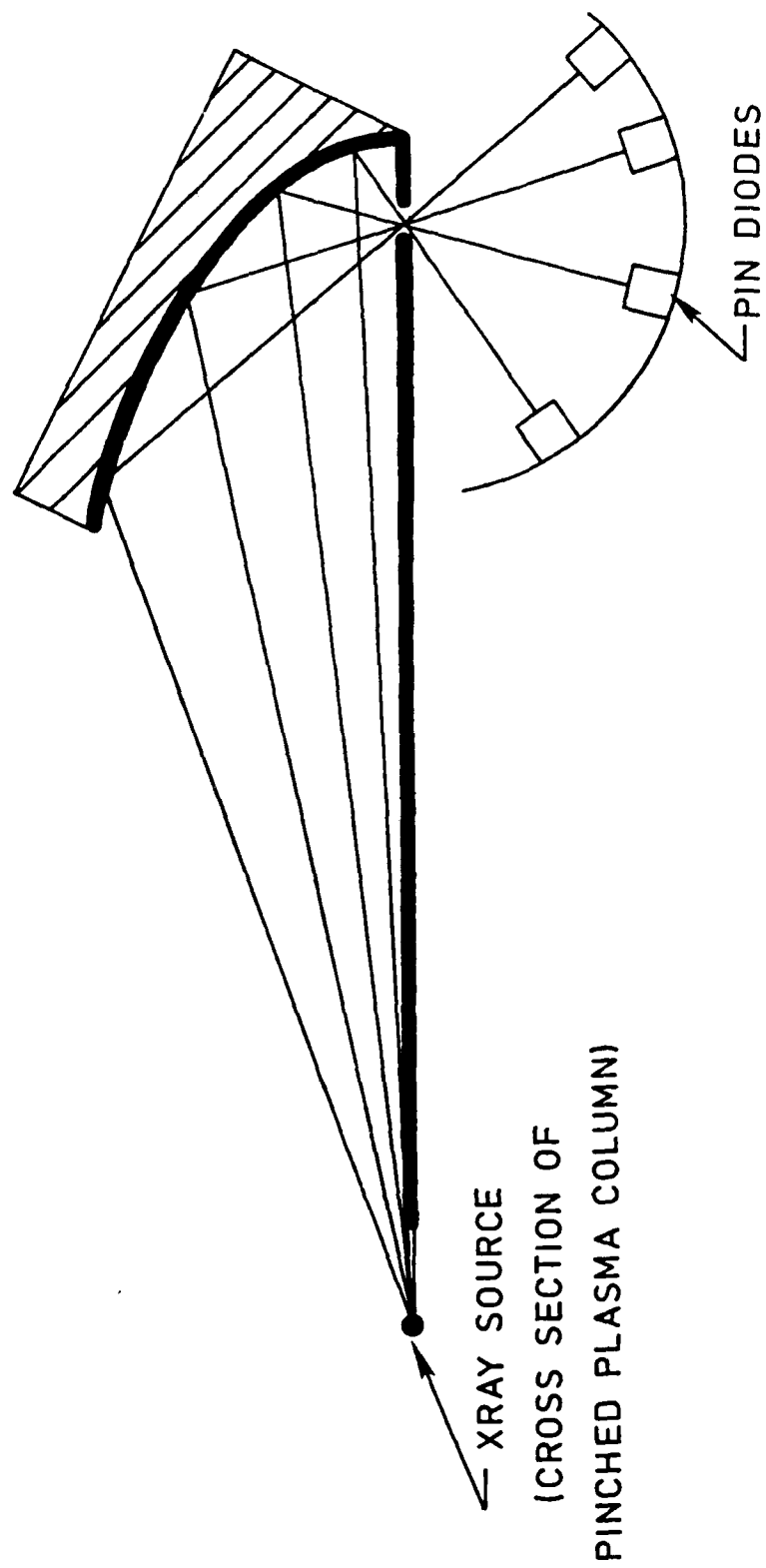


Figure 6

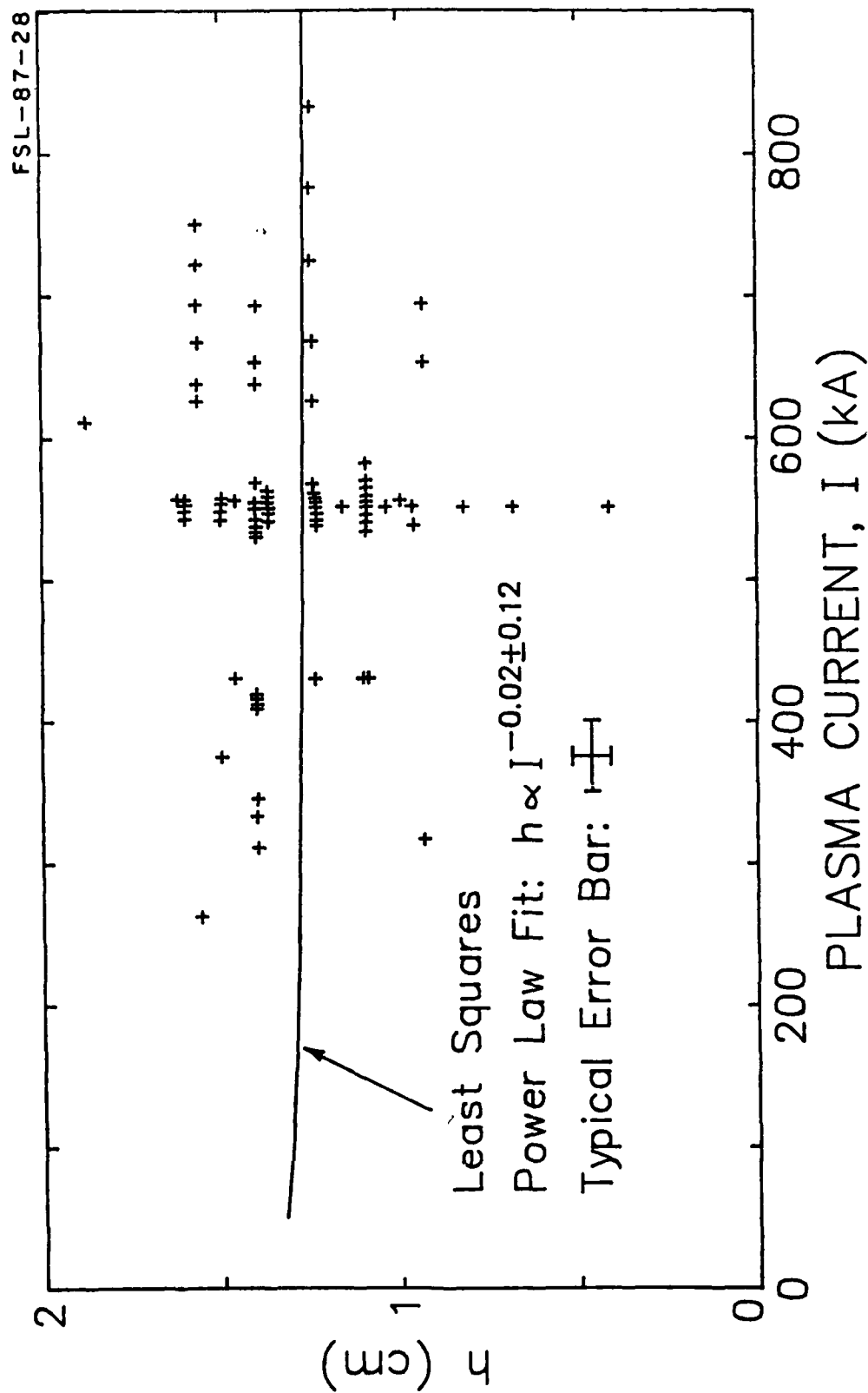


Figure 7

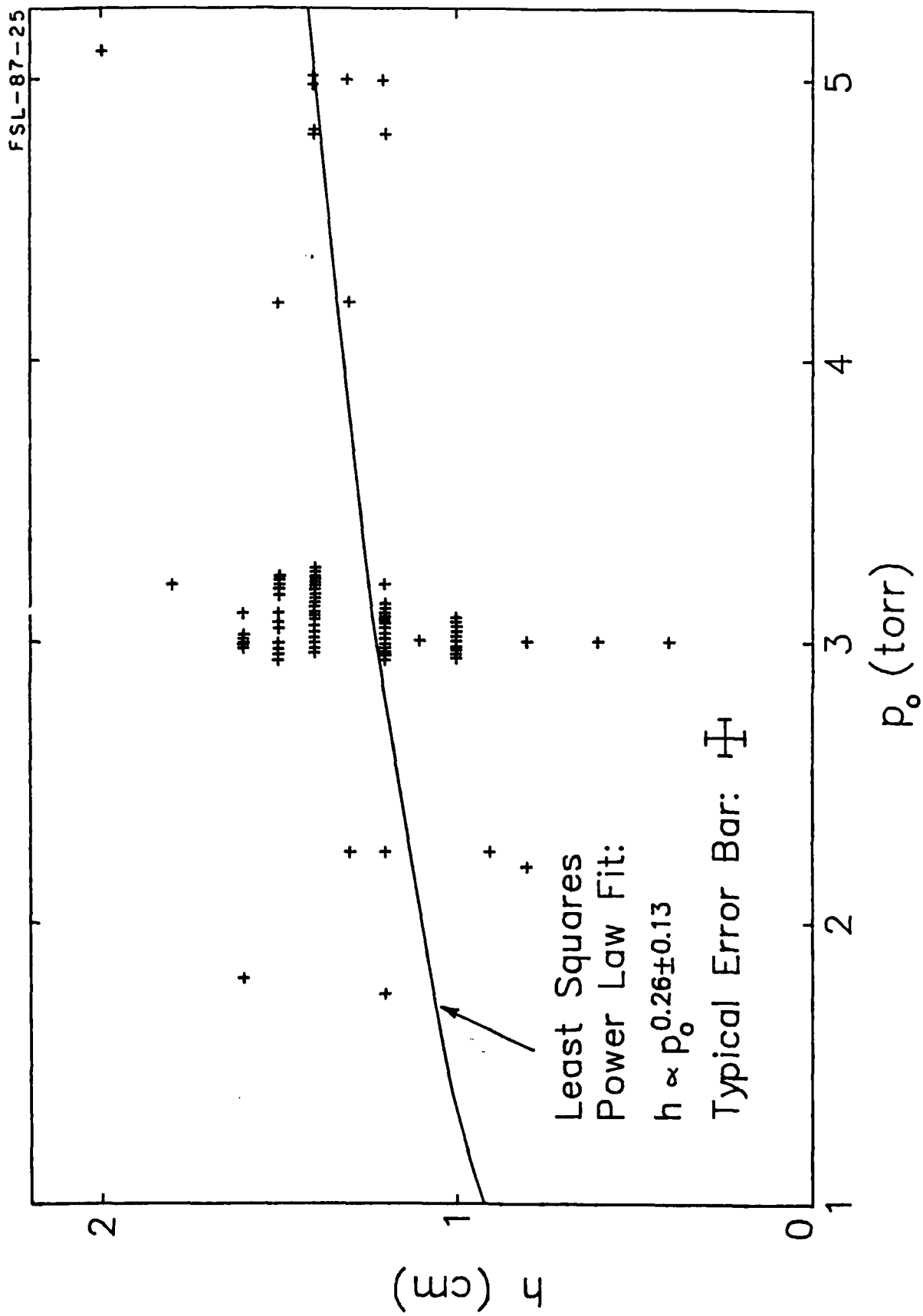


Figure 8

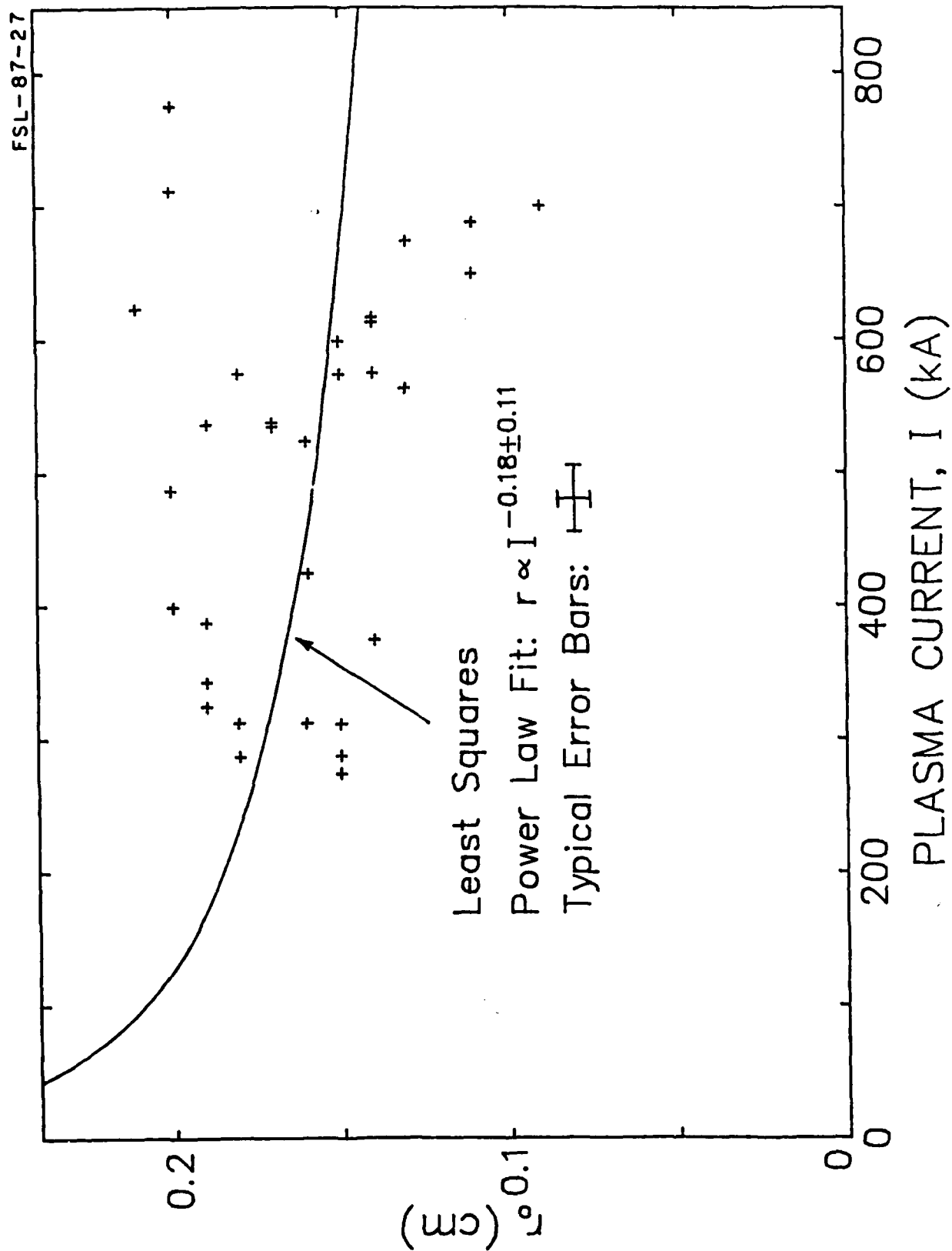


Figure 9

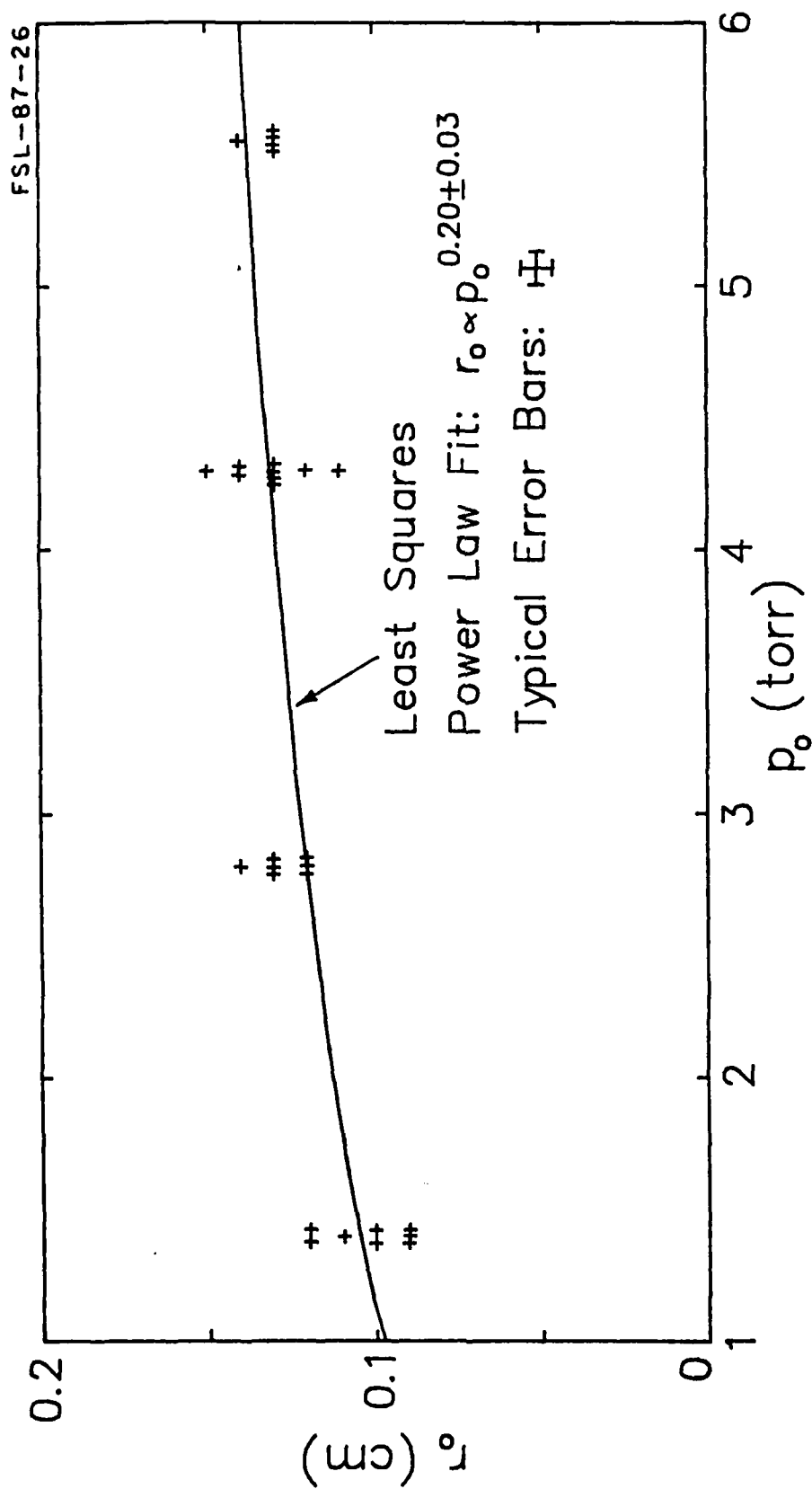
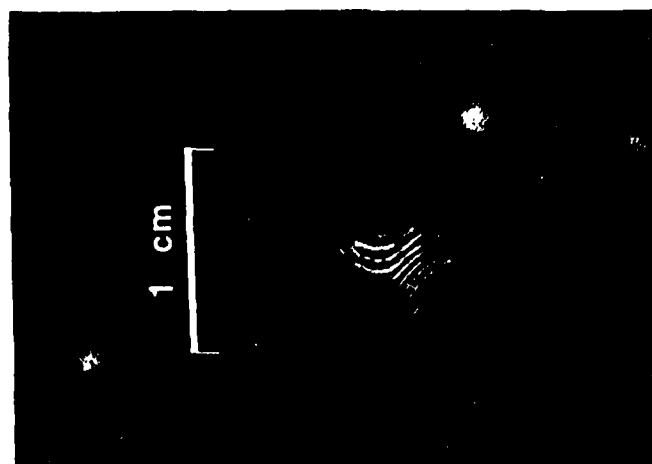
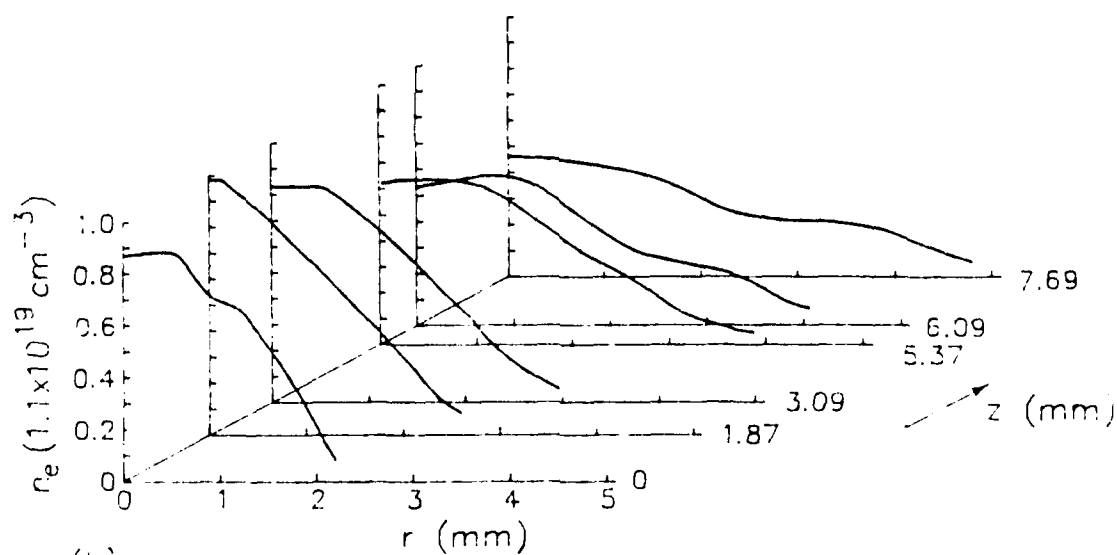


Figure 10





(a)



(b)

Figure 11

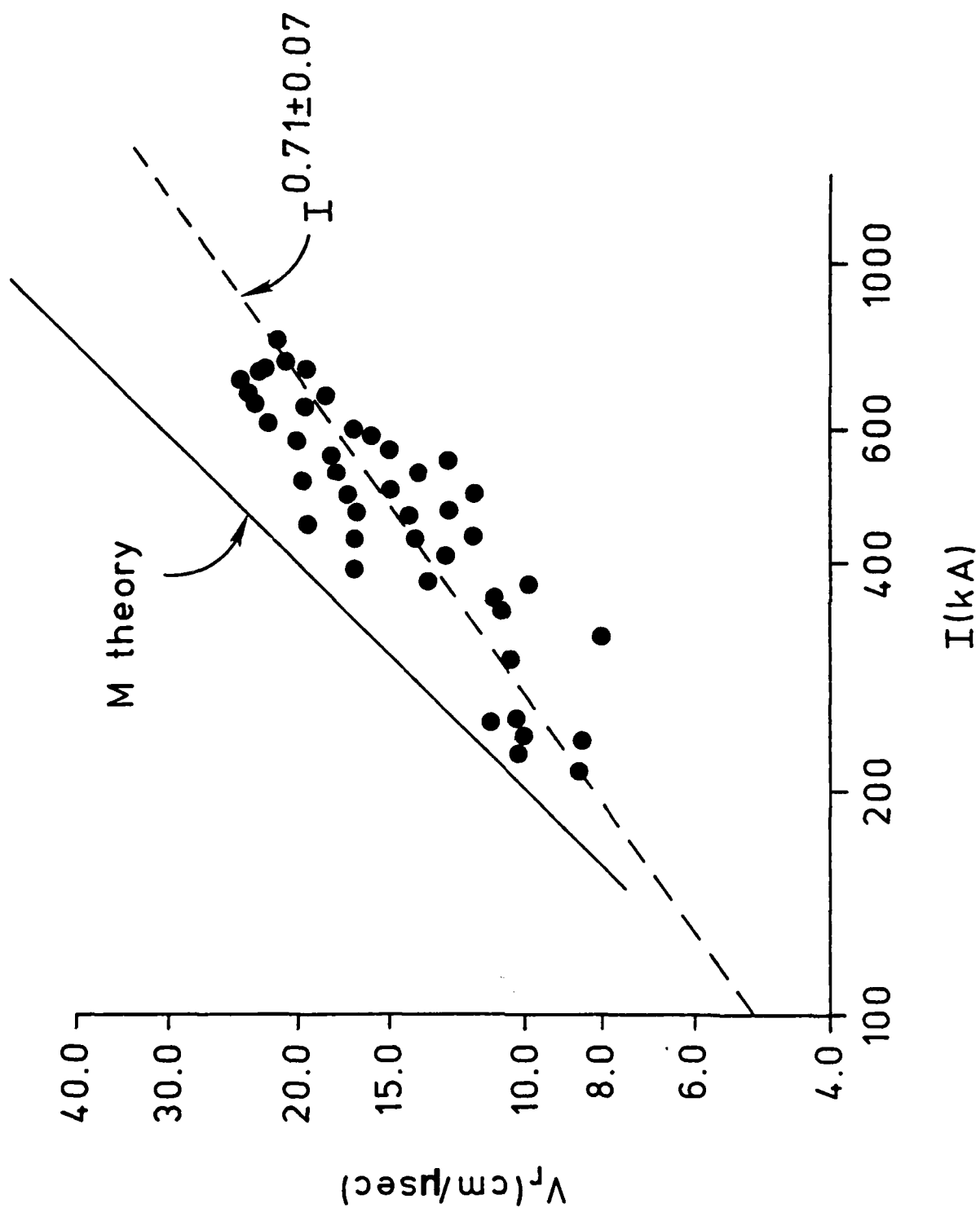


Figure 12

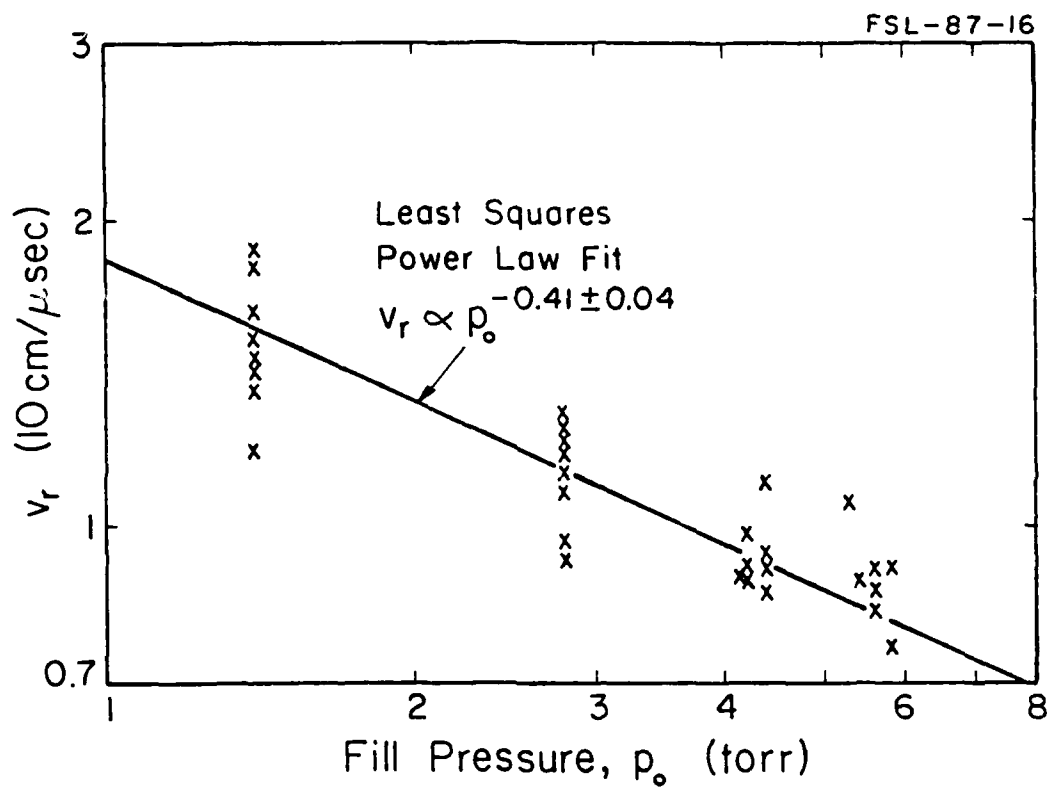


Figure 13

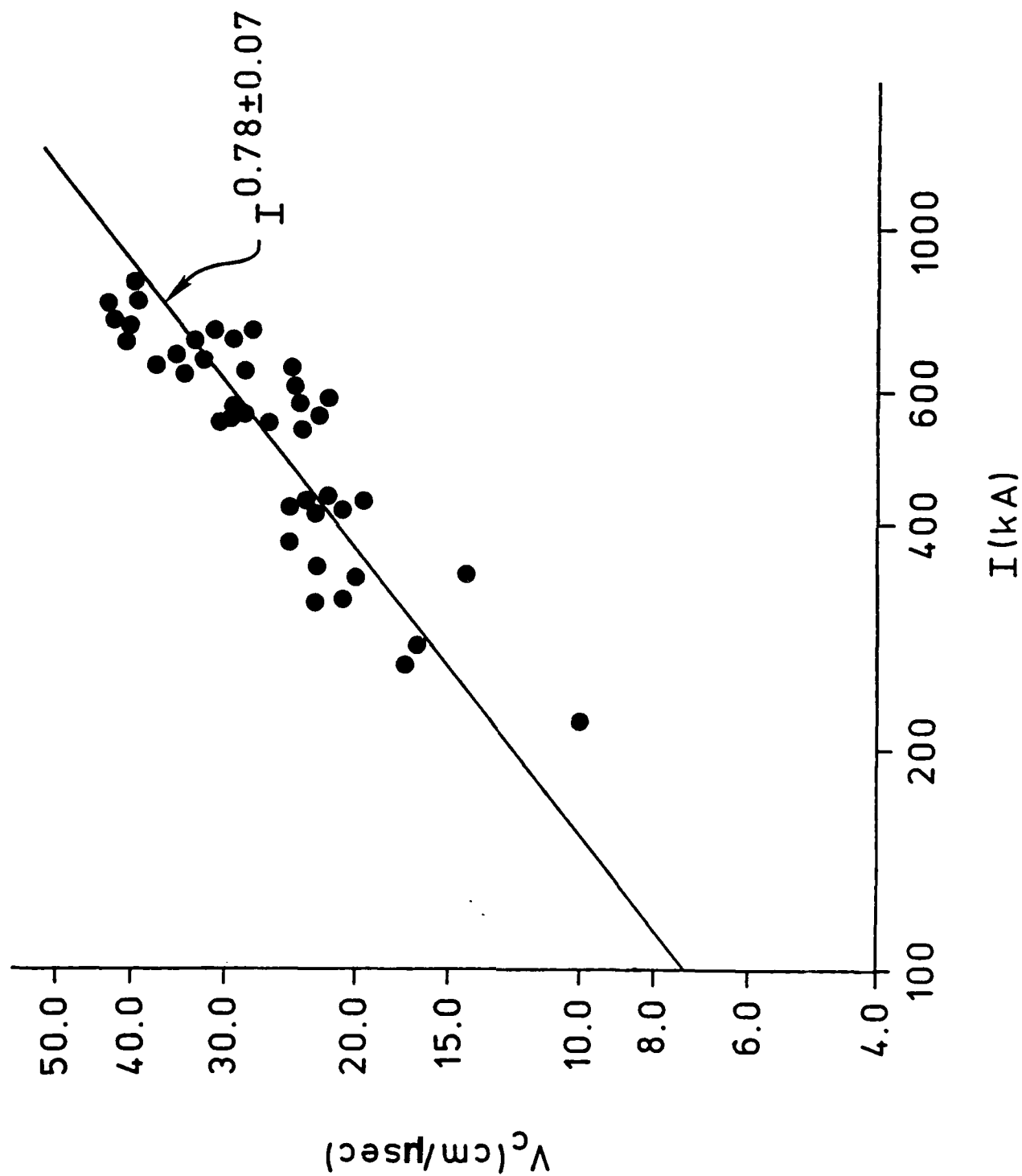


Figure 14

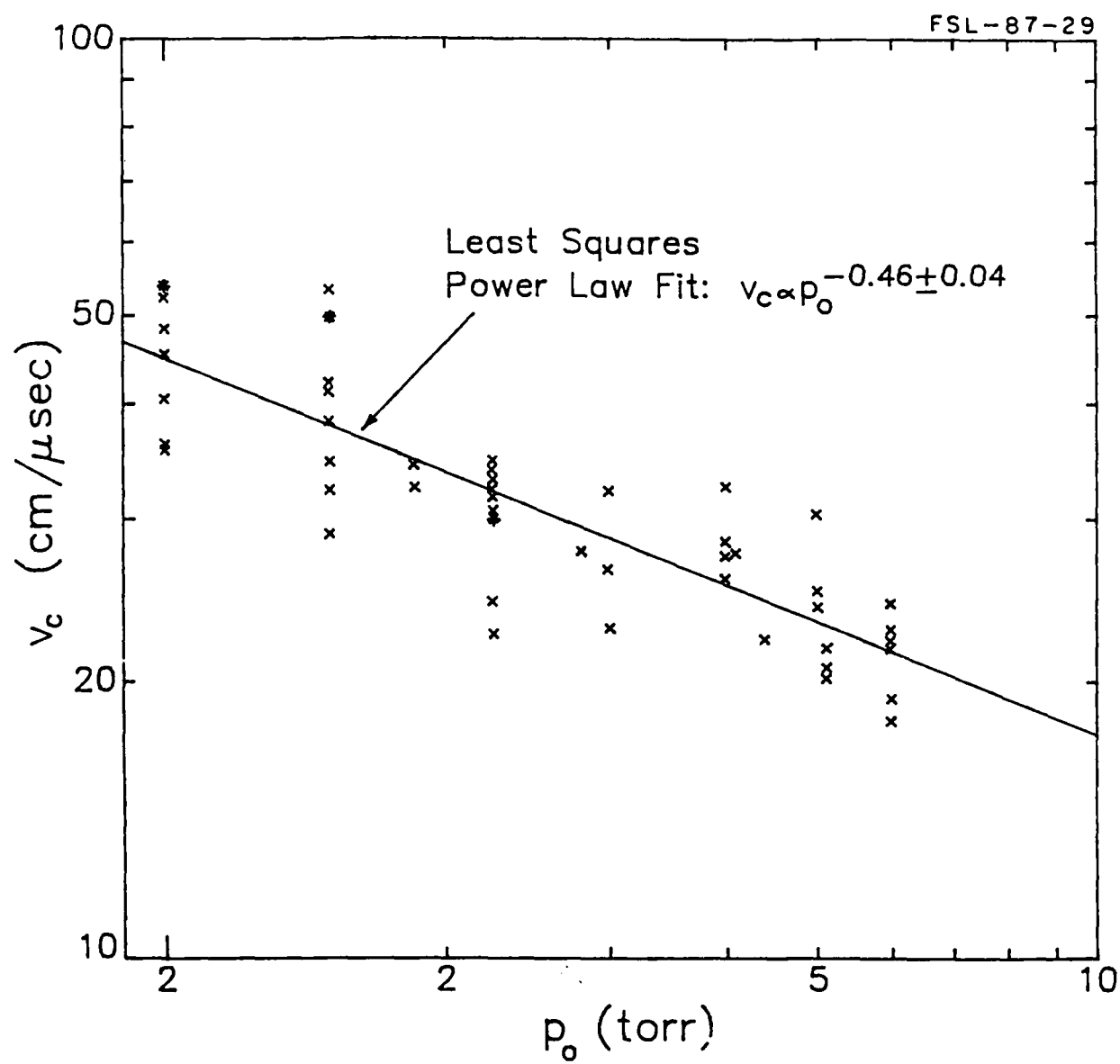


Figure 15

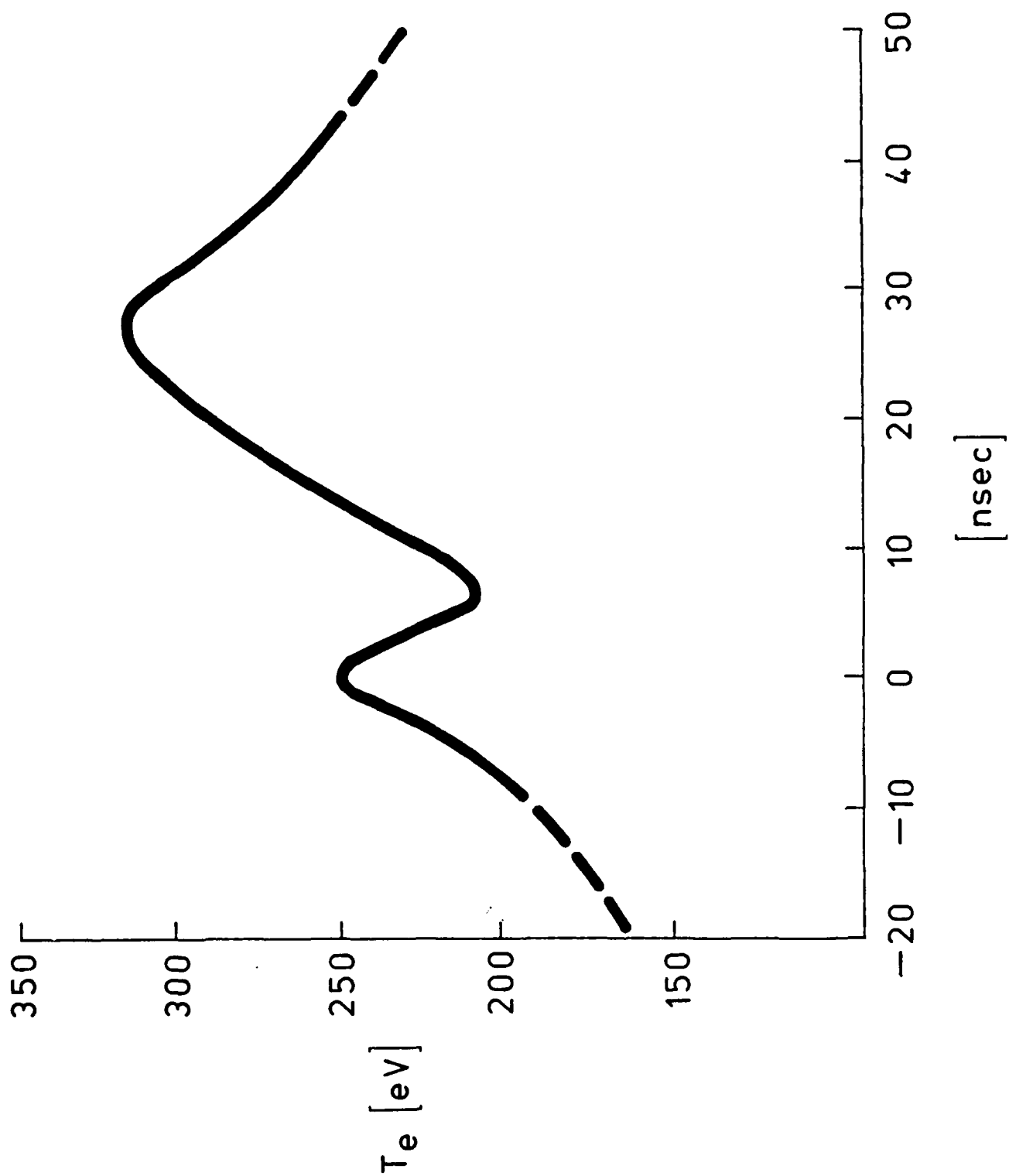


Figure 16

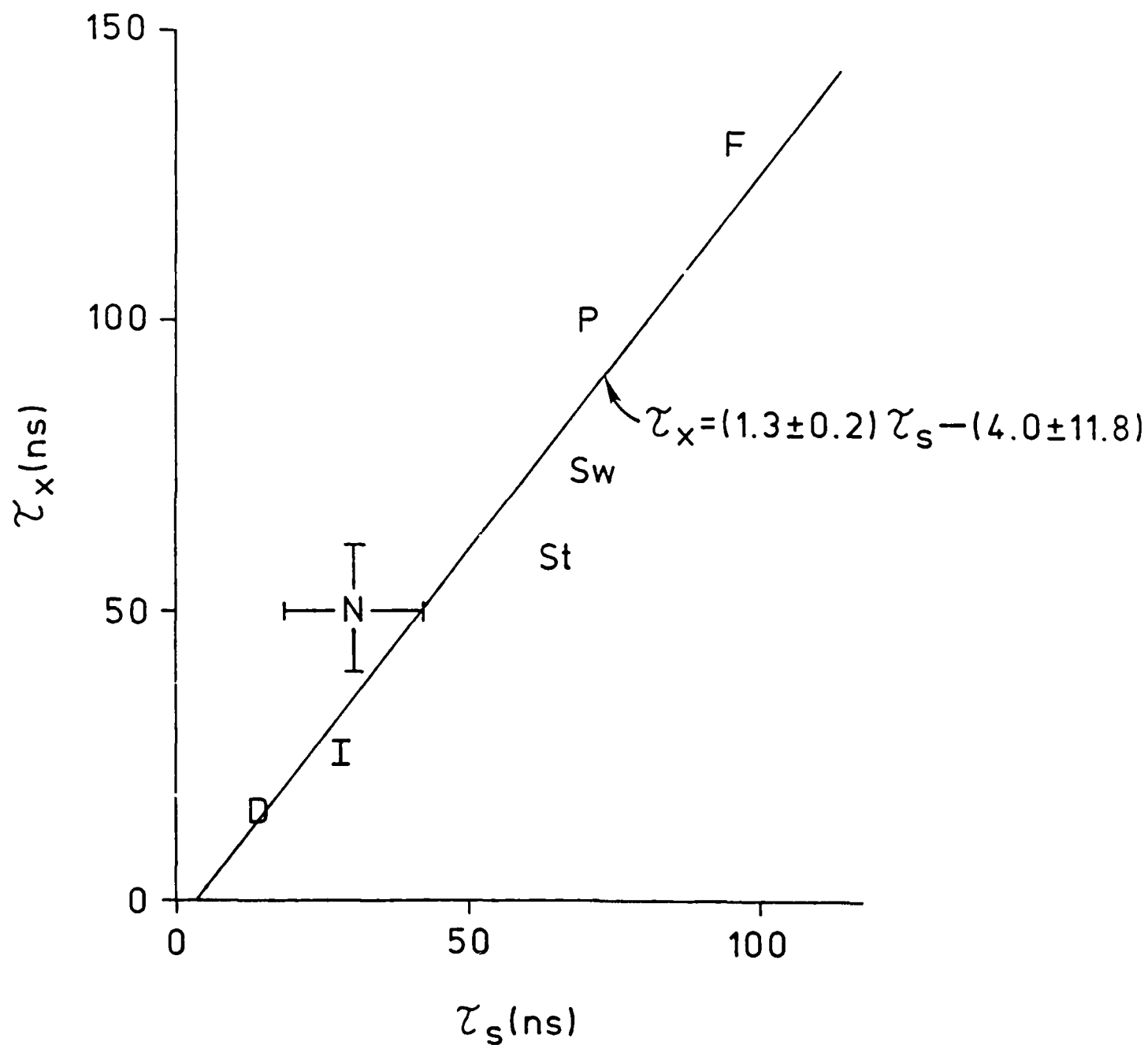


Figure 17

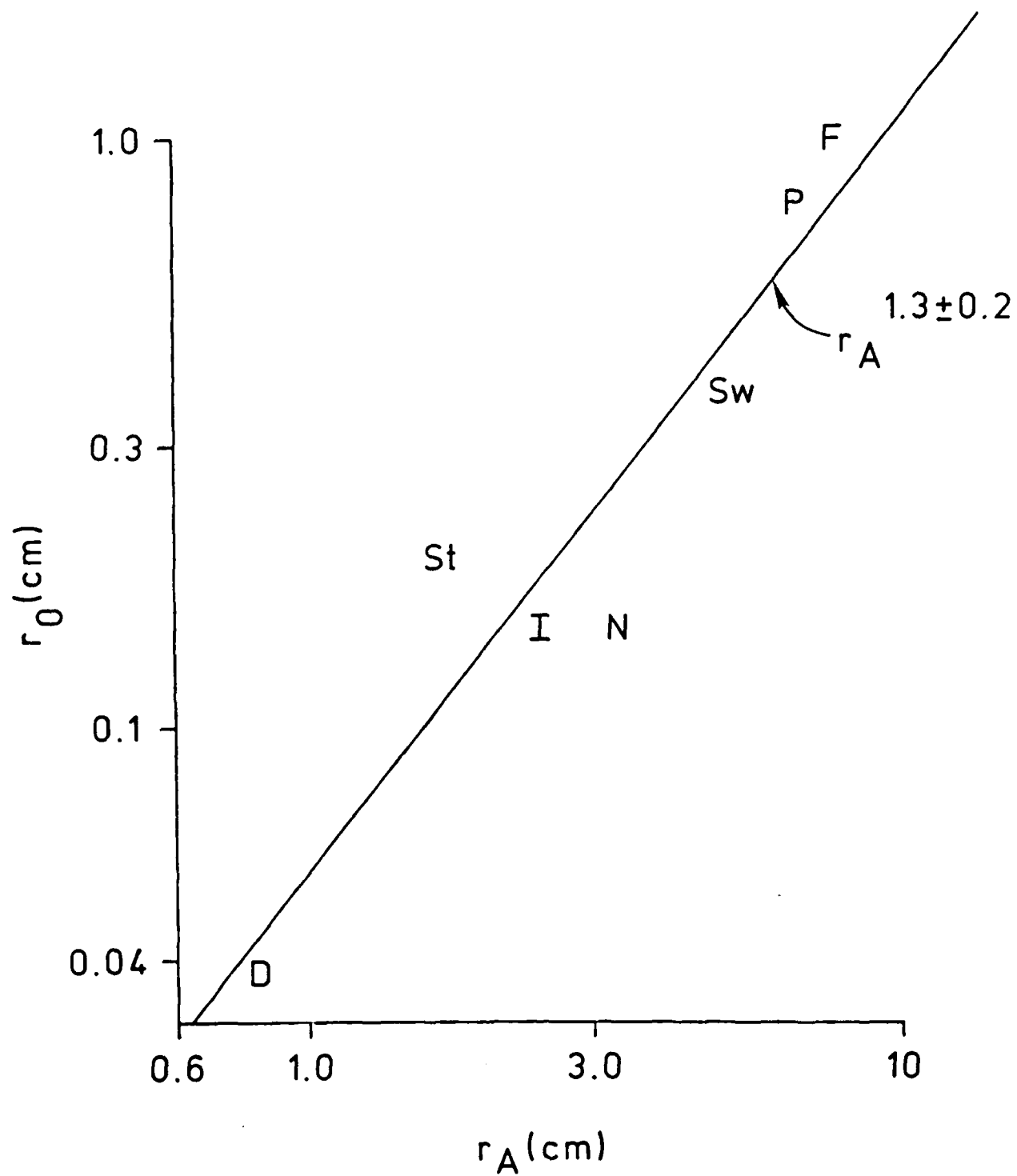


Figure 18



APPENDIX B

TIME RESOLVED DENSITY MEASUREMENTS  
IN THE UNIVERSITY OF ILLINOIS DENSE PLASMA FOCUS  
USING LASER INTERFEROMETRY

BY

KEVIN ARTHUR BOULAIS

B.S., University of Illinois, 1984

THESIS

Submitted in partial fulfillment of the requirements  
for the degree of Master of Science in Electrical Engineering  
in the Graduate College of the  
University of Illinois at Urbana-Champaign, 1987

Urbana, Illinois

UNIVERSITY OF ILLINOIS AT URBANA-CHAMPAIGN

THE GRADUATE COLLEGE

SEPTEMBER 1987

WE HEREBY RECOMMEND THAT THE THESIS BY

KEVIN ARTHUR BOULAIS

ENTITLED TIME RESOLVED DENSITY MEASUREMENTS IN THE

UNIVERSITY OF ILLINOIS DENSE PLASMA FOCUS USING LASER INTERFEROMETRY

BE ACCEPTED IN PARTIAL FULFILLMENT OF THE REQUIREMENTS FOR

THE DEGREE OF MASTER OF SCIENCE

*Glenn C. Kerdin* / *Timothy H. Eust*  
Director of Thesis Research

*Timothy H. Eust*  
Head of Department

Committee on Final Examination†

*Glenn C. Kerdin*

Chairperson

† Required for doctor's degree but not for master's.

## ACKNOWLEDGEMENTS

The author of this thesis is indebted to Professor Glenn A. Gerdin for his suggestions, criticisms and perseverance in arranging for financial assistance. I express appreciation to Professor Kyekyoon Kim for serving as my academic advisor and for the official reading of the text. I would also like to thank Mr. Francesco Venneri for his inexhaustible help and advice throughout the research and for his suggestions for improvement of this text. Thanks also go to Mr. L. Stalker and Mr. C. Anderson for their patience in machining the precision parts.

I also express thanks to my family: the love, encouragement, patience and support of my dear wife Karen and my children Phillip, Barbara and Thomas; the love, encouragement and support of my parents, Mr. and Mrs. Boulais, that led me to seek the degree which leads to this work; to my brother Rick and my sister Gail; and to all of my beloved in-laws.

## TABLE OF CONTENTS

	Page
I. INTRODUCTION . . . . .	1
A. The Dense Plasma Focus . . . . .	1
B. Overview of Interferometry as a Plasma Diagnostic . . . . .	4
II. EQUIPMENT . . . . .	7
A. The Nitrogen Laser . . . . .	7
1. Source Requirements . . . . .	9
2. Laser Operation . . . . .	12
B. The Mach-Zehnder Interferometer . . . . .	17
C. The Detection Stage . . . . .	22
1. The Timing Detector . . . . .	22
2. The Fringe Detector . . . . .	22
a. The Lens and Pinhole . . . . .	25
b. Filters . . . . .	30
c. Film . . . . .	31
D. The Complete Interferometer System . . . . .	31
III. DATA ANALYSIS . . . . .	34
A. Line Density . . . . .	34
B. The Plasma Density (Assuming Axial Symmetry) . . . . .	35
C. Numerical Analysis . . . . .	37
D. Analytical Examples and Numerical Error Analysis . . . . .	40
IV. DATA . . . . .	47
A. Timing . . . . .	47

	Page
B. Results . . . . .	48
1. The First Compression . . . . .	48
2. The Radial Expansion . . . . .	56
3. The Second Compression (Plasma Breakup) . . . . .	56
C. Error Margins . . . . .	61
V. SUMMARY AND CONCLUSIONS . . . . .	63
APPENDIXES	
I. FRINGE SHIFT OF A WAVE IN A DIELECTRIC . . . . .	65
II. APPROXIMATIONS FOR PLASMA INDEX . . . . .	68
III. INTERFEROMETER ALIGNMENT PROCEDURE . . . . .	72
REFERENCES . . . . .	75

## I. INTRODUCTION

The determination of electron density in a plasma is important in the formulation of plasma models. Some of the more common parameters that the electron density,  $n_e$ , helps to reveal are electron plasma frequency ( $f_p \propto n_e^{1/2}$ ), electron collision rates ( $R \propto n_e$ ), plasma skin depth ( $\delta_s \propto n_e^{-1/2}$ ), and Debye length ( $\lambda_D \propto n_e^{-1/2}$ ).

The time resolved density profile is important in displaying plasma boundaries and, resolution permitting, finer structures of the plasma such as current sheaths. In a dynamic plasma such as that generated in a plasma focus, knowledge of the density profile is fundamental to the understanding of plasma behavior and permits comparison with various theoretical models.

It is the purpose of this work to measure the electron density profile of the plasma produced by a dense plasma focus in order to study the dynamics of the pinch phase; a nitrogen laser interferometer is used.

### A. The Dense Plasma Focus

The dense plasma focus (DPF) is a machine that transforms a cold, low pressure gas into a hot, high density plasma. Conversion is achieved by the magnetic pinch effect. Plasma densities on the order of  $10^{19} \text{cm}^{-3}$  are produced along with high neutron yields and intense radiation across a wide region of the spectrum.

Because significant numbers of neutrons are produced, the DPF was originally studied as a potential fusion reactor. However, the dense plasma does not last long enough in present day devices to obtain a "break even" reactor<sup>1</sup>. The DPF is still being researched as a high energy opening switch<sup>2</sup>, soft x-ray source<sup>3</sup>, laser pumping device<sup>4</sup>, neutron source and, aside from many other possible applications, it is being studied for a better understanding of hot, dense plasmas.

The device consists of a pair of coaxial electrodes - open at one end and insulated at the other - in a gas filled chamber (Figure 1). Up to 100 kJ of electrical energy stored in a capacitor bank is discharged into the electrodes through spark gap switches. The pinch process starts as an electrical breakdown of the gas along the base insulator forming a current sheath between the electrodes. The self-induced magnetic field lifts the current sheath from the insulator and accelerates it down the electrodes. When the open end of the electrodes is reached, the current sheath collapses radially, forming a high density plasma column.

For the University of Illinois DPF, the center electrode has a diameter  $d_1=5$  cm, the outer electrode has an inner diameter  $d_0=10$  cm and the length is 25 cm. The energy is initially stored in four 10  $\mu$ F capacitor banks placed symmetrically around the electrodes. The initial voltage on the capacitors,  $V_0$ , can be varied between 20 kV and 30 kV in

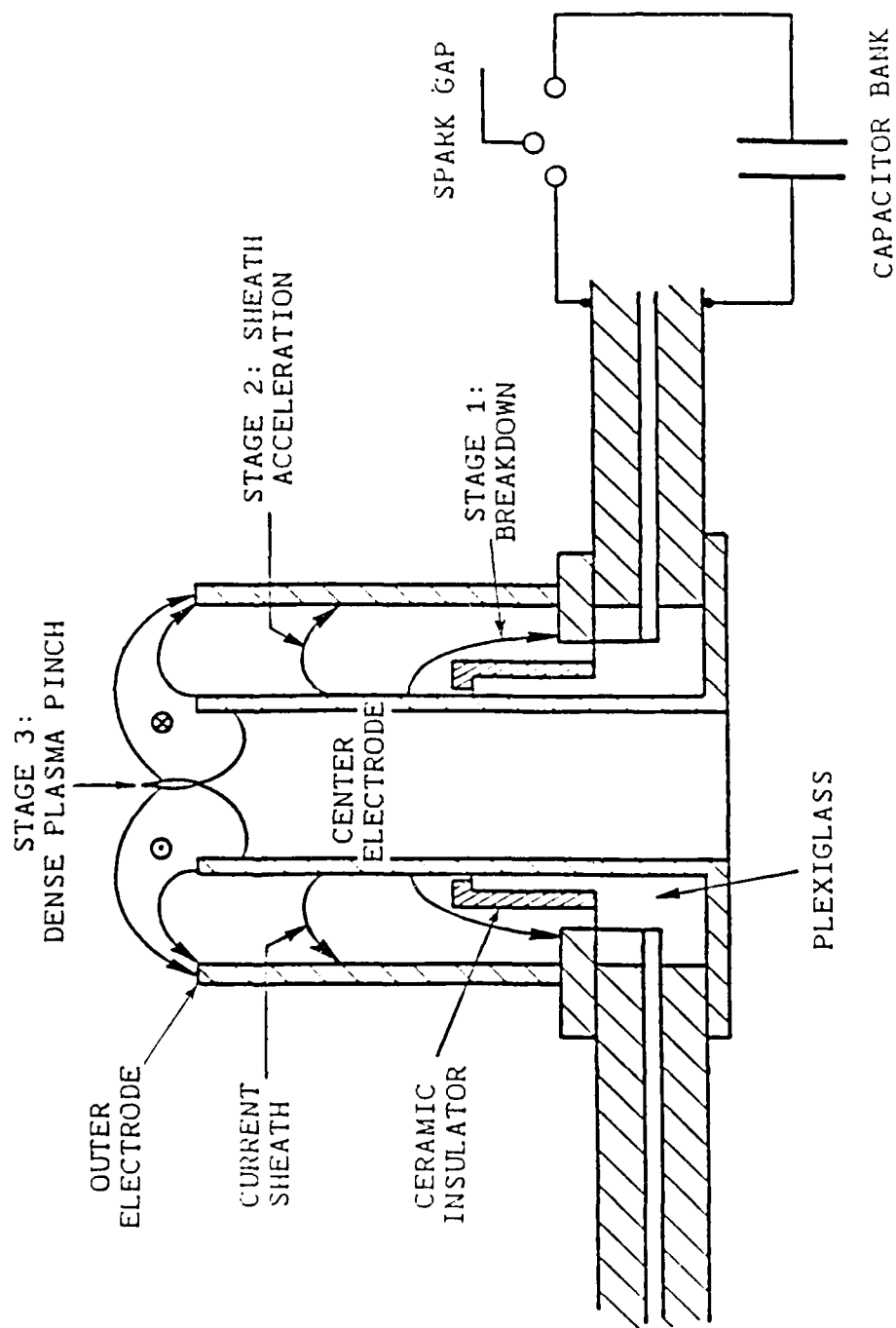


Figure 1. Schematic of a Mather-type dense plasma focus with an exhibit of the three stages leading to the pinch.



order to vary the plasma current. The gas in the fill chamber is usually deuterium or hydrogen at 3 torr. The pressure,  $P_0$ , can also be varied from 1.5 torr to 5 torr.

#### B. Overview of Interferometry as a Plasma Diagnostic

All interferometers rely on interference to produce fringes on a screen (Figure 2). A single electromagnetic wave is split in two and recombined with a slight angle,  $\theta$ , between the wave vectors,  $k_1$  and  $k_2$ . The phase fronts interfere constructively and destructively producing light and dark areas on the screen known as fringes. For a rigorous mathematical treatment of fringe production see Reference 5.

The two waves must originate from a single source in order to preserve the phase information. It is easily seen from Figure 2 that the fringes will move across the screen proportionally with a change in phase between the two waves. The phase shifts can be random, caused by the natural line broadening of the source, or determined by a change in optical path length of one wave with respect to the other. The second case is of interest here. If a material of length  $L$  and index of refraction  $\mu(y)$  is inserted in one arm of the interferometer, the fringes will change position on the screen according to

$$\delta = \frac{1}{\lambda} \int_L [\mu(y) - 1] dy \quad (1)$$

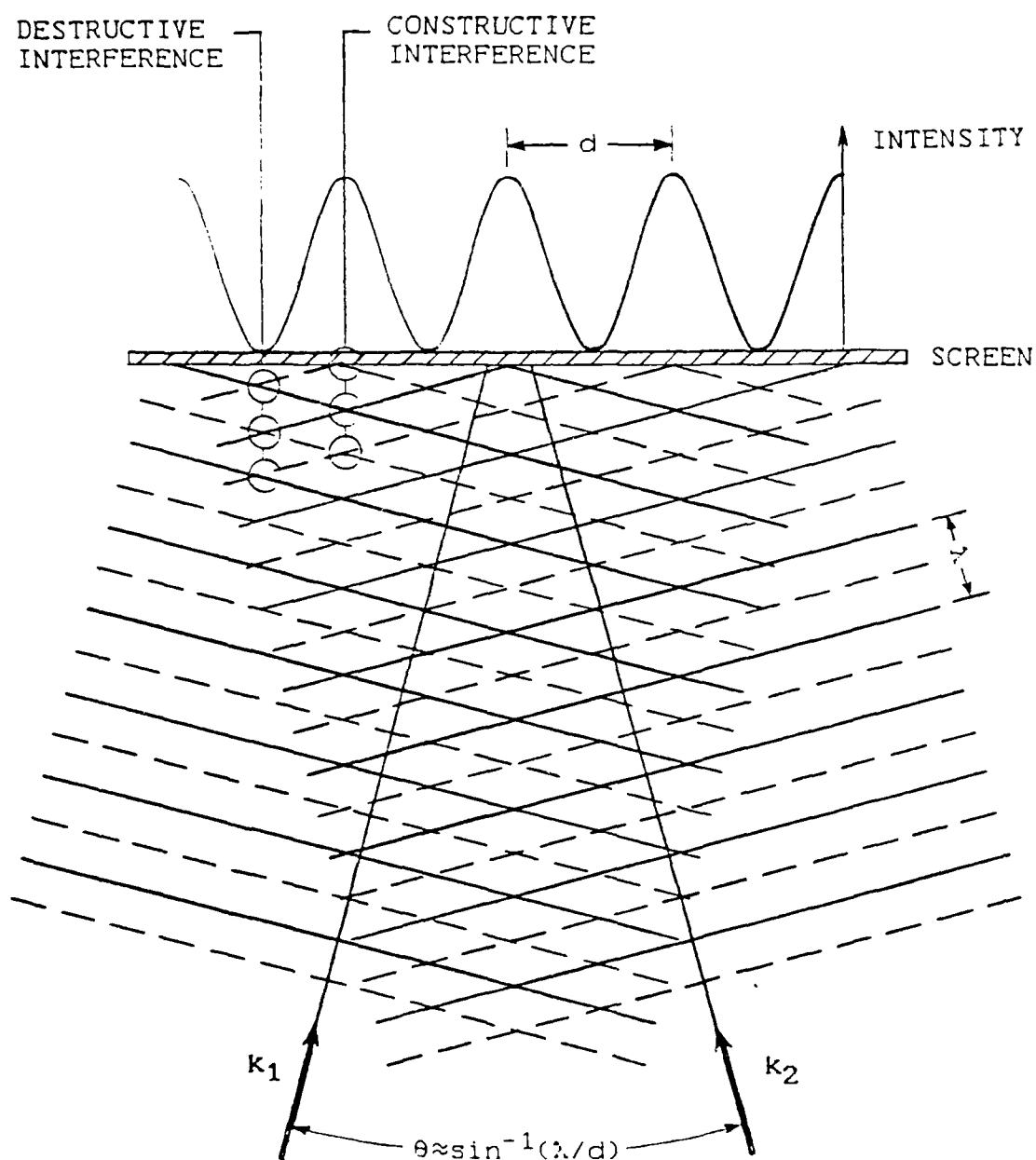


Figure 2. Two plane waves of the same wavelength,  $\lambda$ , interfering on a screen ( $\theta$  is greatly exaggerated).

where  $\delta$  is the fringe shift in wavelength units,  $\lambda$  is the source wavelength in a vacuum and  $y$  is the line-of-sight path of a source ray through the medium (see Appendix I).

For a highly ionized plasma in which the wave frequency is much larger than the electron plasma frequency, which in turn is much larger than electron cyclotron frequency and electron-ion collision frequency, the term in the integral of Equation (1) can be approximated by

$$\mu(y)-1 \approx \frac{-f_p(y)^2}{2f^2} \quad (2)$$

(see Appendix II) where the plasma frequency is given by

$$f_p(y) = \sqrt{\frac{e^2}{4\pi^2 m_e \epsilon_0} n_e(y)} \quad (3)$$

The fringe shift observed on the screen is therefore a direct measure of plasma density.

In this research the critical density for which the plasma frequency is equal to the source frequency (UV light,  $\lambda=337.1\text{nm}$ ) is  $9.8 \cdot 10^{21}\text{cm}^{-3}$ , which represents the theoretical upper limit in plasma density at which the laser light is reflected. In practice, the upper limit is about one-third of this value<sup>6</sup>. From Equations (1), (2) and (3), the minimum density that can be measured in this experiment is approximately  $10^{17}\text{cm}^{-3}$ , which corresponds to a few tenths of a fringe shift.

## II. EQUIPMENT

The interferometer system (Figure 3) can be separated into three major components:

1. a radiating source,
2. interferometric optics, and
3. a detection stage.

A laser is the obvious choice for the radiating source since it is inherently coherent and its frequency can be much greater than the plasma frequency of a dense plasma. The interferometric optics consist of two beamsplitters (one to split the light beam and one to recombine it) and two beam guidance mirrors. A special camera is used in the detection stage to record the fringes on film, and a fast photodiode is used to determine the timing of the laser output relative to the plasma event.

### A. The Nitrogen Laser

A molecular nitrogen laser has been selected as the source. The wavelength of the most powerful  $N_2$  line<sup>8</sup> is  $\lambda=337.1$  nm. which corresponds to the  $C^3\Pi_u - B^3\Pi_g$  band.

The laser was built at the University of Illinois and was originally designed to be used in an undergraduate laboratory as a learning aid. Several modifications were made to adapt the laser to the interferometer, such as a larger electrode cross section to produce a more uniform beam and a low jitter triggering system.

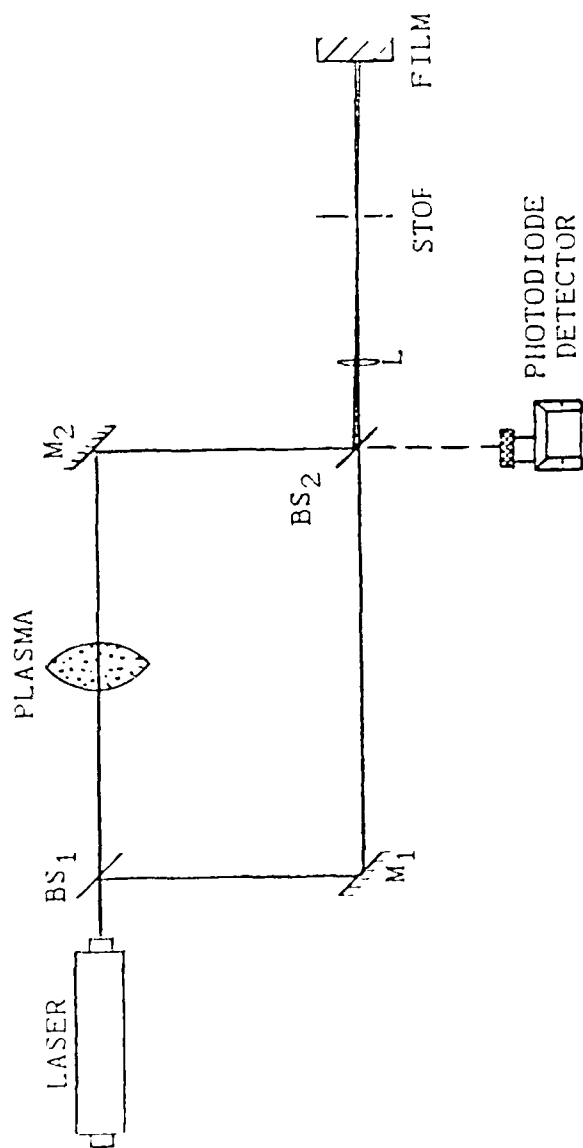


Figure 3. A simplified schematic of a Mach-Zehnder interferometer used for plasma density measurements. The laser is the plasma probe. The interferometric optics include two beamsplitters (BS<sub>1</sub> & BS<sub>2</sub>) and two beam guidance mirrors (M<sub>1</sub> & M<sub>2</sub>). Also shown is the fringe detector (consisting of a lens L, a pinhole and film) and the photodiode detector.

## 1. Source Requirements

The source requirements are:

- 1) the frequency must be high enough that the plasma acts as a lossless dielectric,
- 2) the frequency must be low enough to retain sensitivity in the interferometer system,
- 3) the output must have a fair degree of coherence in order to obtain fringes,
- 4) the source should emit paraxial rays,
- 5) the source must have a high intensity output, and
- 6) the source should be pulsed in the case of a dynamic plasma.

The nitrogen laser fulfills all the requirements needed for its use in this experiment. The first requirement is dealt with in Appendix II.

The second requirement arises from the fact that the fringe shift is inversely proportional to the source frequency (Equations (1) and (2)). As the frequency increases, the fringe shift (for a given plasma density) will decrease and the sensitivity of the system will be reduced. The useful density range (see Introduction) is

$$10^{17}\text{cm}^{-3} < n_e < 10^{21}\text{cm}^{-3}.$$

The maximum density for the University of Illinois DPF has been estimated<sup>3</sup> to be  $n_e \approx 2 \cdot 10^{19}\text{cm}^{-3}$ . Thus, the nitrogen laser will resolve the plasma density over two orders of magnitude.

The third requirement, coherence, is needed to obtain fringes. In general, the optical path difference between the two arms of the interferometer (including the phase shift from the plasma in the "probe" path) must be less than the coherence length of the source. The coherence length of a nitrogen laser is only a few millimeters, since the laser operates without a cavity (due to the high gain of  $N_2$ ). The short coherence length adds inconvenience to the adjustment of the path length difference (for further details, see Section B: The Interferometer).

The fourth requirement, paraxial rays, is needed so the phase shift is not lost due to finite detector aperture. The  $N_2$  laser operates without a cavity and the beam divergence is relatively large. The divergence can be approximated by

$$\theta/2 \approx w/d \quad (4)$$

where  $w$  is the cavity width and  $d$  is the electrode length. For the  $N_2$  laser used in this research,  $w=1.2$  cm,  $d=91$  cm and  $\theta \approx 26$  mrad. A pinhole is used to remove most of the nonparaxial rays (see Section C: The Detection Stage).

The intensity of the source (fifth requirement) must be much higher than the intensity irradiated by the plasma at that wavelength. The light from the plasma adds a background component to the fringe visibility, which tends to

swamp the fringe pattern with light. The output power of the laser is  $\approx 500$  kW (Figure 4) which is much greater than the expected blackbody radiation of the pinch ( $\approx$  watts).

Finally, the laser must be pulsed since the plasma produced in a DPF is rather short lived. It is known<sup>9</sup> from streak pictures taken of the University of Illinois DPF that the radial implosion velocity of the pinch at a fill pressure of 3 torr is  $\approx 11$  cm/ $\mu$ s. Since the laser pulse is 6 ns at FWHM (Figure 4), the horizontal resolution of the fringe profile is  $\approx 0.7$  mm. The resolution is actually much better because a) the radial velocity represents a maximum<sup>9</sup> and b) the fringe smear caused by the plasma movement is averaged out when the data are read.

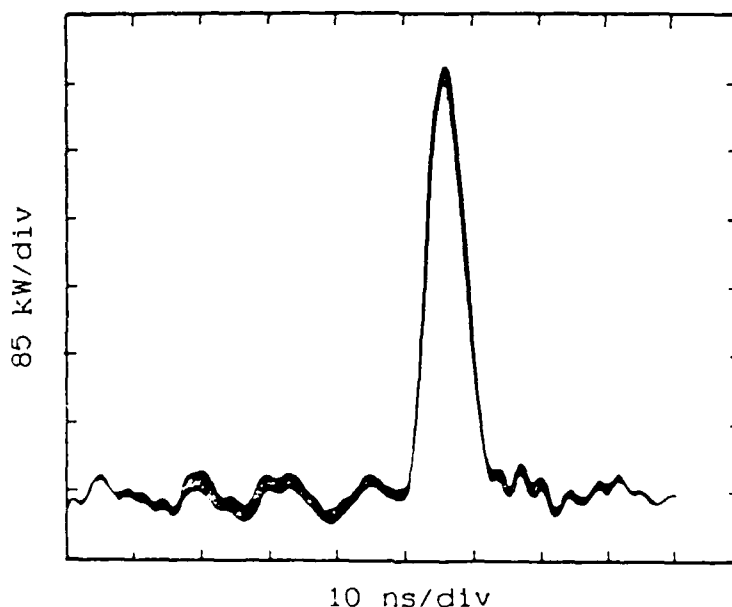


Figure 4. The  $N_2$  laser output as a function of time (detected using a fast silicon photodiode).



## 2. Laser Operation

Table 1 lists the specifications of the nitrogen laser. Figure 5 shows a block diagram of the laser's electrical system and Figure 6 is of the gas flow system.

The energy storage system for a nitrogen laser must be able to excite the gas to the  $C^3\Pi_u$  state in a time much less than 40 ns, which is the spontaneous lifetime of the state. To achieve this it is common to use a Blumlein structure, which is a parallel-plate transmission line with low inductance. As shown in Figure 7a, the total inductance and capacitance of the discharge system can be modeled in an LC circuit with a period of

$$T = 2\pi(LC)^{1/2} \quad (5)$$

The highest potential across the cavity electrodes is reached at 1/4 of this period (Figure 7b), at which time the  $N_2$  discharge takes place. The total capacitance on the oscillatory side is  $\approx 10$  nF. A discharge time of much less than 40 ns requires a total inductance of  $L \ll 16$  nH. Therefore, the design of a low inductance spark gap is crucial since this is probably the largest source of inductance in the discharge system. A field distortion gap with a "ring" trigger was designed to fire the laser. The size of the gap as well as the electrode spacing were kept to a minimum. The gap is typically pressurized with air to  $\approx 30$  lb.

Table 1. Nitrogen Laser Specifications

Population Inversion Method:	Electron collisions by transverse electric amplification (TEA)
E/P:	210 V/cm-torr
Energy/Pulse:	$\approx 3.0$ mJ
FWHM:	$\approx 6$ nS
Energy Storage:	Double Blumlein ( $\approx 4.1$ J @ $V_0=20$ kV)
Efficiency:	0.07%
Gas Fill System:	Static fill
Trigger Type:	Field distortion spark gap with ring trigger
Cavity Type:	Superradiant
Electrode Separation:	1.2 cm
Electrode Length:	91 cm
Cavity Length:	100 cm

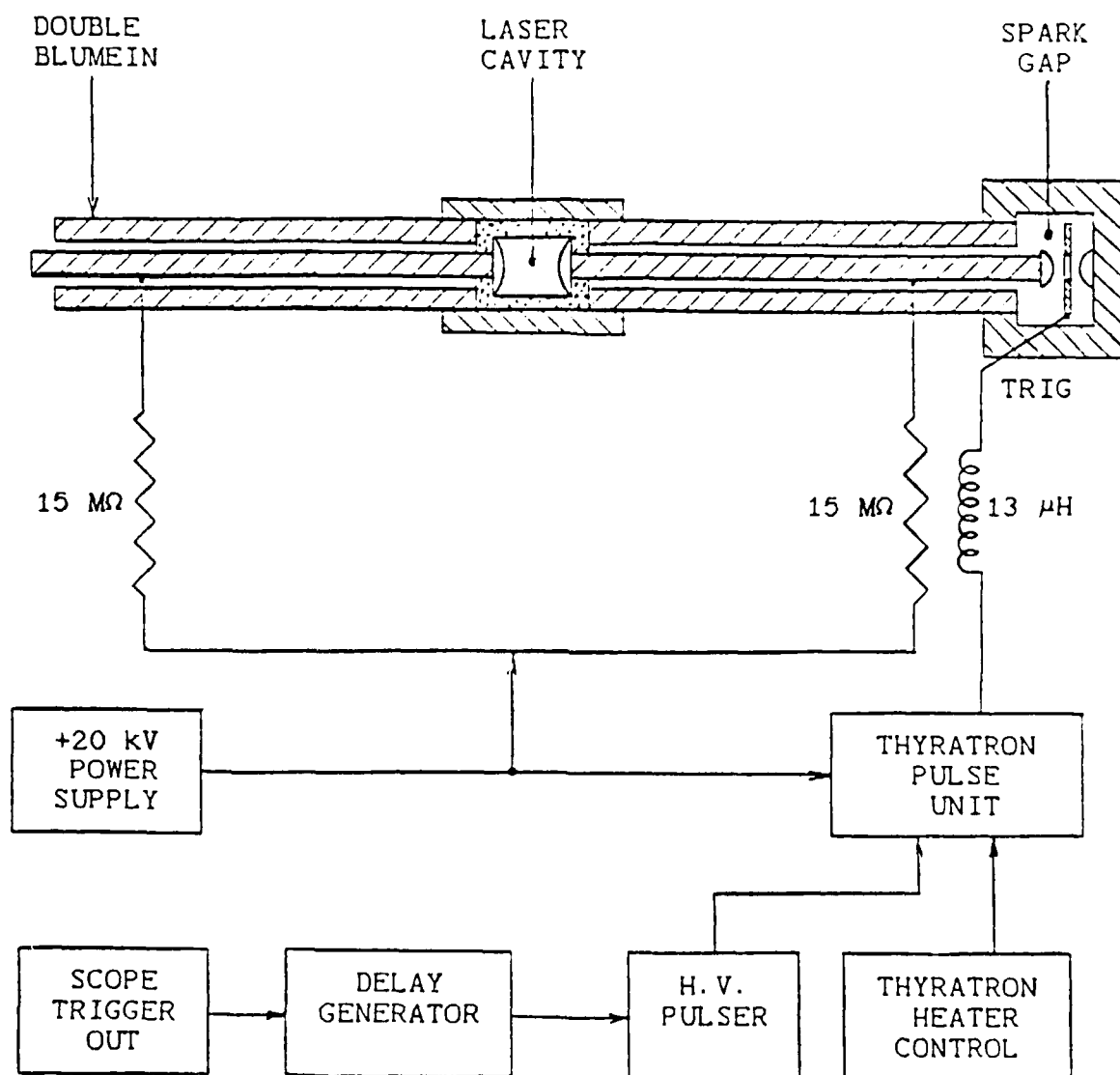


Figure 5. End cut-away view of the nitrogen laser with a block diagram of its electrical system.

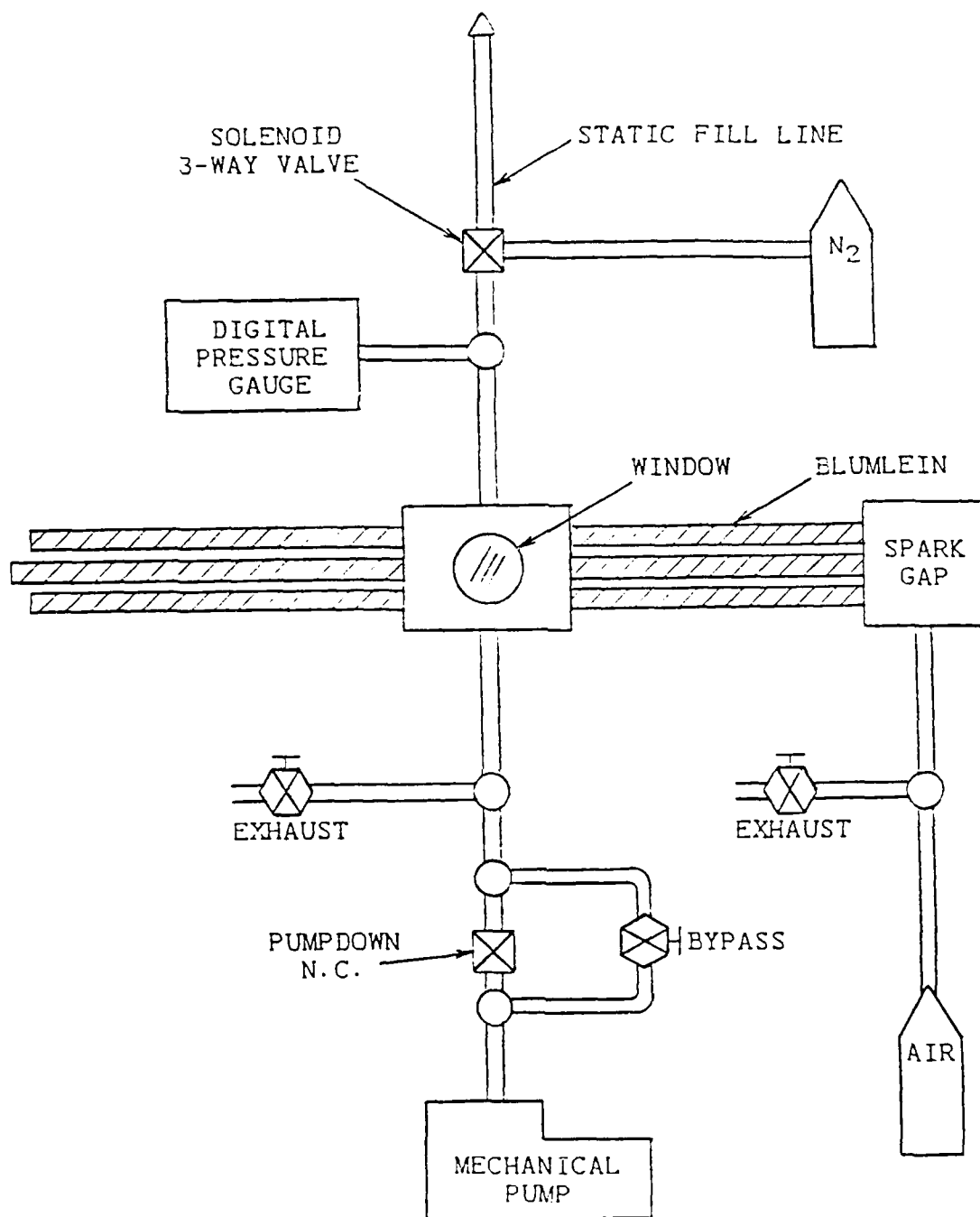
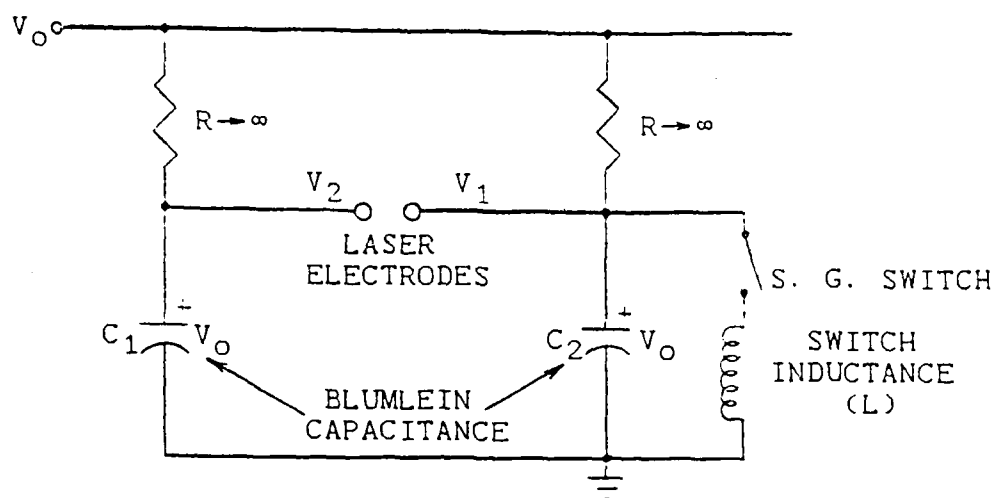
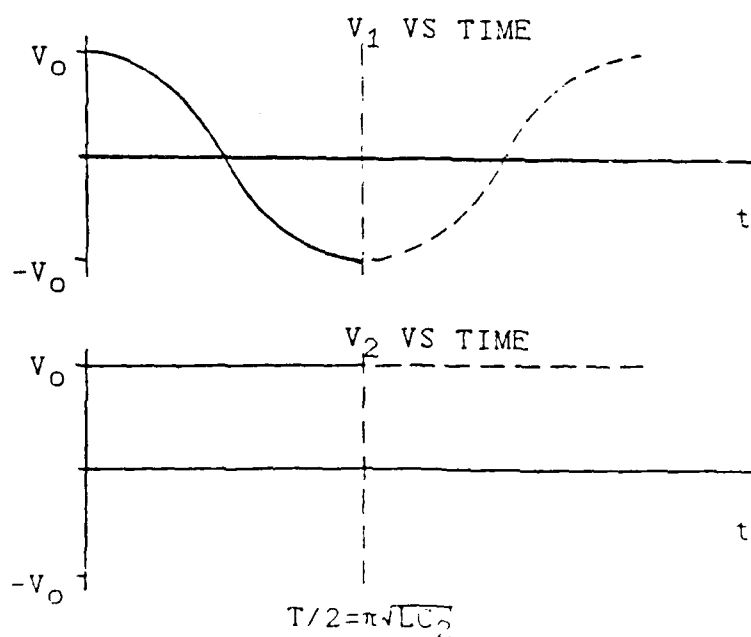


Figure 6. End view of N<sub>2</sub> laser and the gas flow arrangement.



(a)



(b)

Figure 7. (a) Equivalent circuit for the  $N_2$  laser. (b) Oscillatory diagram for the above circuit.

It is also critical that the jitter of the laser pulse with respect to the pinch time be kept minimal. This was accomplished with the aid of a thyatron pulse unit used to trigger the spark gap. As seen in Figure 5, the thyatron and the Blumlein are charged with the same power supply. However, the thyatron releases a -20 kV pulse to the +20 kV charged spark gap helping to reduce jitter since the breakdown occurs from the trigger ring to both main electrodes simultaneously. It was experimentally determined that a small inductance of  $\approx 13 \mu\text{H}$  is needed between the thyatron pulser and the gap's trigger ring to reduce the amount of energy flow to the thyatron when triggered.

#### B. The Mach-Zehnder Interferometer

The Mach-Zehnder interferometer consists of a source beamsplitter ( $\text{BS}_1$ ), two beam guidance mirrors ( $\text{M}_1$  and  $\text{M}_2$ ) and a beam recombination beamsplitter ( $\text{BS}_2$ ) shown in detail in Figure 8 (setup for DPF density measurements). All these components are oriented at  $45^\circ$  angles to the initial source beam with adjustment provisions made through gimbal mounts (GM). Adjustment for the equality of the two beam paths is provided by a translational stage attached to mirror  $\text{M}_2$ . This also eliminates the need for a phase shift compensator in the reference path (to account for the phase change due to the windows in the probe path). All gimbal mounts and their respective optics are attached to the DPF

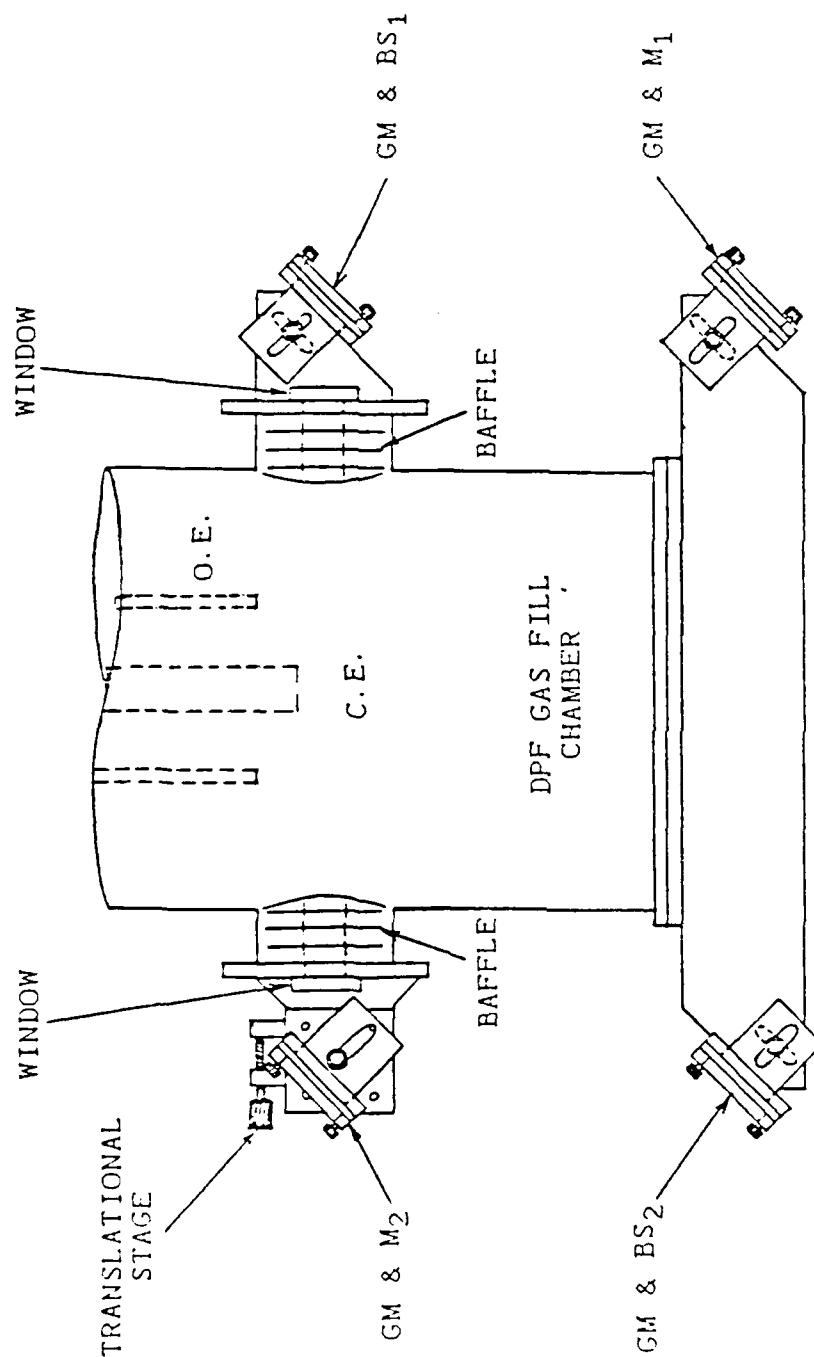


Figure 8. Detailed schematic of the mounting arrangement for the interferometer optics to the DPF gas fill chamber. C.E. is the center electrode and O.E. is the outer electrode.

vacuum chamber with flanges designed to reduce room vibrations that may be present.

Each optical component that the beam traverses must be flat to much less than a wavelength of the source in order to exhibit a straight, flat vacuum fringe pattern. Since each wave traverses different optical components, the flatness prevents different phase distortions in each path.

The substrate for all optics is synthetic fused silica. This material has exceptional UV transmission properties ( $\approx 90\%$  at  $\lambda = 337$  nm) and is very resistant to radiation darkening from UV, x-rays, and neutrons<sup>10</sup>, all of which are produced in a dense plasma focus. Three tier baffles have been placed in the DPF adjacent the fill chamber windows (Figure 8) to further reduce darkening of the windows from electrode metal vapor deposits. The deposits could destroy the flatness of the windows. Each baffle, as well as most other nonoptical components to the interferometer system, have been blackened to reduce reflections for safety purposes and to reduce other possible distortions in the fringe pattern induced by reflections.

It has been mentioned that the difference in path lengths between the reference wave and the the probe wave should be minimized (to much less than the coherence length of the source) in order to obtain highly visible fringes. This is especially true since the nitrogen laser does not use a resonating cavity. In such a case, the bandwidth of the



wave imposes a limit on how rapidly the phase can vary, and this can be related to the coherence length by<sup>5</sup>

$$l_c = c/\Delta\nu \quad (6)$$

where  $\Delta\nu$  is the bandwidth and  $c$  is the speed of light. For the nitrogen laser, the coherence length is on the order of a few millimeters. However, the contrast of the fringes varies strongly over this length. The variations can best be described in terms of the visibility function<sup>5</sup>,  $V$ , defined as

$$V = \frac{I_{\max} - I_{\min}}{I_{\max} + I_{\min}} \quad (7)$$

where  $I_{\max}$  and  $I_{\min}$  are the constructive and destructive wave intensities, respectively. It is a function of the optical path difference,  $\tau$ , bandwidth of the source,  $\Delta\nu$ , and intensities of the two waves.

The visibility function for the system used in this thesis peaks at  $\tau=0$  and rapidly approaches zero. The loss of visibility in the fringe pattern as  $\tau$  increases or decreases is caused by one wave becoming more random in phase with respect to the other because of line broadening of the source. Through experimentation, the path difference must be less than  $\approx 20 \mu\text{m}$  in order to obtain high contrast fringes (Figure 9). The procedure used to align the interferometer

within this limit is discussed in Appendix III.

The visibility function is greatest when the two wave intensities are equal. Since the beamsplitters used for this experiment are very nearly 50/50, the intensities are equal up to the point of recombination. However, due to the antireflection coating on the back of  $BS_2$ , more than 60% of the reference beam gets transmitted to the detector whereas only 50% of the probe beam reaches it. The problem is easily solved by placing an 80% transmission neutral density filter in the reference path. The filter, also manufactured from synthetic fused silica, has an index of refraction different from the surrounding air, which affects the path length difference and must be taken into account.

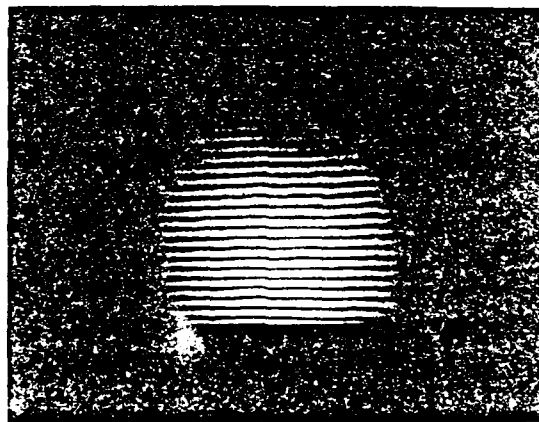


Figure 9. Vacuum interferogram showing highly visible fringes from a well adjusted interferometer. The nonparallelism between the top and bottom fringes is caused by skew paths. The problem adds only minimal distortions to horizontal measurements.

NO-A198 155

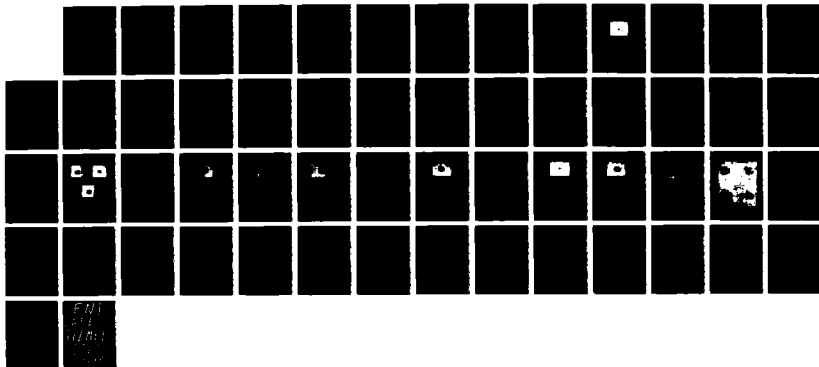
OPENING SWITCH RESEARCH ON A PLASMA FOCUS VI(U)  
ILLINOIS UNIV AT URBANA DEPT OF NUCLEAR ENGINEERING  
G A GERDIN 26 FEB 88 AFOSR-TR-88-0938 AFOSR-86-0383

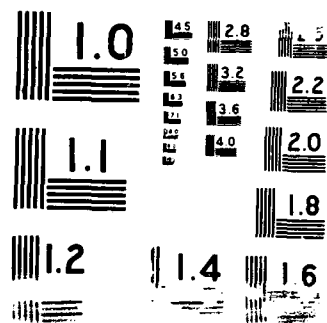
2/2

UNCLASSIFIED

F/8 28/8

NL





### C. The Detection Stage

Two detectors are needed for this interferometer system: one for timing purposes and the other to record the fringe pattern. The timing detector was built around a fast silicon photodiode (used to obtain the trace in Figure 4). The fringe recorder is Polaroid film which the light reaches after passing through a series of optics needed to correct distortions and add magnification to the fringe profile.

#### 1. The Timing Detector

The timing detector consists of a fast silicon photodiode (1 ns risetime) in the circuit of Figure 10. The peak of the laser pulse from the diode indicates the time at which the fringe photograph is taken relative to the plasma pinch event. Because of the high sensitivity of the diode (1 A/W at  $\lambda=337$  nm), several neutral density filters were needed to attenuate the laser light. A bandpass filter ( $\lambda=337\pm6$  nm) at the diode input isolates the laser light from noise produced by both room and plasma light.

#### 2. The Fringe Detector

The fringe detector (Figure 11) consists of three parts:

- a) a multipurpose lens and spatial low-pass filter (pinhole).
- b) neutral density and bandpass filters, and
- c) photographic film.

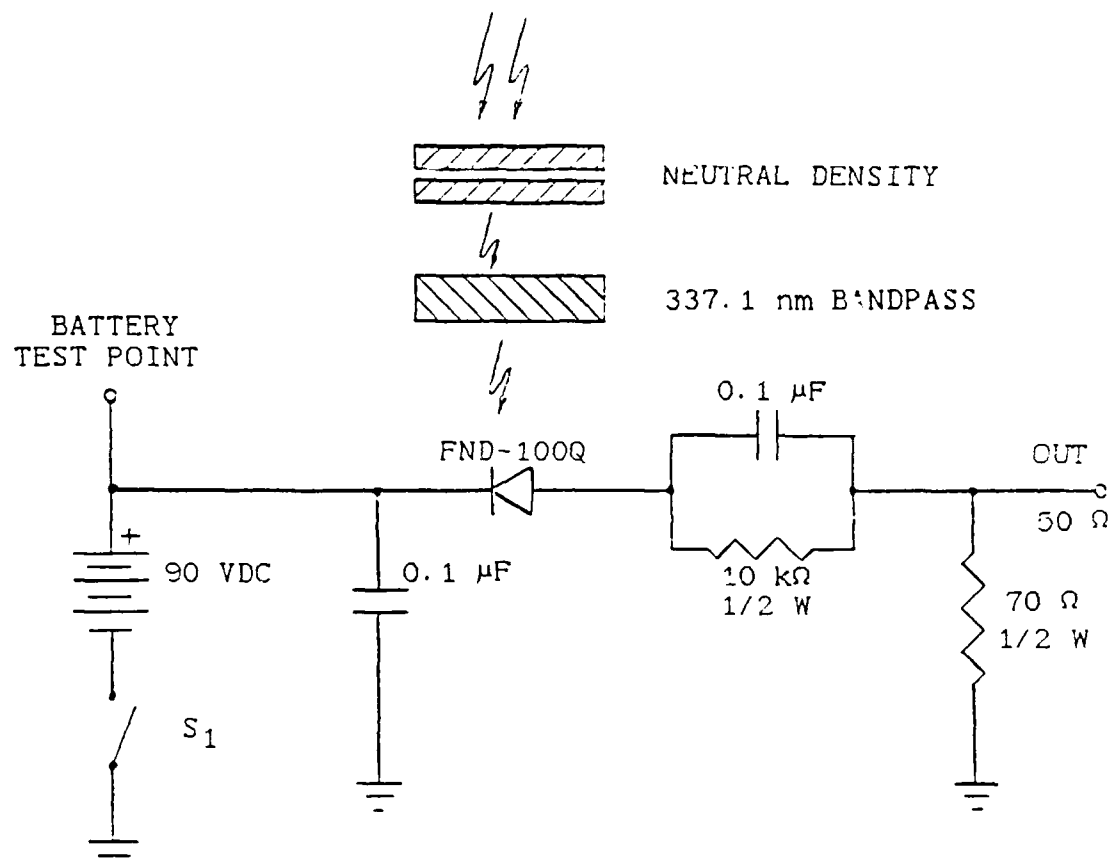


Figure 10. Schematic diagram of the laser pulse detector.

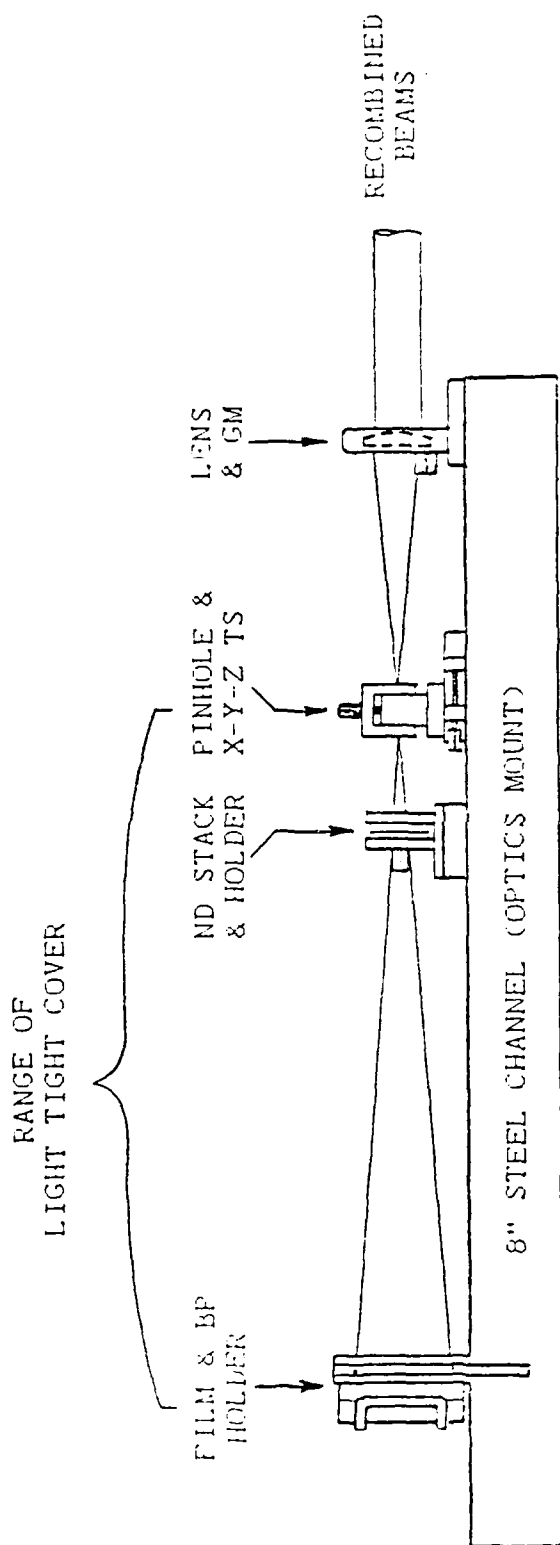


Figure 11. Component layout for the fringe detector/recorder.  
 BP, bandpass filter; ND, neutral density filter;  
 TS, translational stage; GM, gimbal mount.

### a. The Lens and Pinhole

The most important purpose of the lens is to prevent distortion of the fringe image from laser beam refraction created through density variations of the plasma pinch. Using the ray matrix method<sup>11</sup>, the input and output parameters of a general optical system are related by the ABCD matrix,

$$\begin{bmatrix} R_{out} \\ R'_{out} \end{bmatrix} = \begin{bmatrix} A & B \\ C & D \end{bmatrix} \cdot \begin{bmatrix} R_{in} \\ R'_{in} \end{bmatrix}, \quad (8)$$

where  $R$  is the radial distance from the optical axis and  $R'$  is the slope of that ray. For an optical system consisting of a length of free space ( $d_1$ ), a lens of focal length  $f$  (using thin lens approximations) and another segment of free space ( $d_2$ ), the matrix becomes

$$\begin{bmatrix} R_2 \\ R'_2 \end{bmatrix} = \begin{bmatrix} 1-d_2/f & d_1-d_1d_2/f+d_2 \\ -1/f & 1-d_1/f \end{bmatrix} \cdot \begin{bmatrix} R_1 \\ R'_1 \end{bmatrix}. \quad (9)$$

By letting

$$B = d_1 - d_1d_2/f + d_2 = 0 \quad (10)$$

where  $d_1$  is the distance from the center of the plasma pinch to the lens and  $d_2$  is the distance from the lens to the film plane, the radial function of the image on the film does not depend on the slopes of the rays as they leave the plasma. In effect, the plane of the film is moved to a distance  $B$



from the plasma pinch. When  $B=0$ , the system is in focus.

The second purpose for the lens is to magnify the fringe image on the film for better readability. The magnification factor is (for  $B=0$ )

$$M = R_2/R_1 = 1-d_2/f. \quad (11)$$

By choosing a particular magnification factor and focal length, the distances  $d_1$  and  $d_2$  are determined.

The third purpose of the lens is to focus the near-paraxial beam through a sufficiently small pinhole. The term near-paraxial is used in reference to the refraction of the laser light through the plasma rather than from the natural beam divergence which can be assumed to equal zero from Equation (10). Since Equation (10) can equal zero for one image plane distance only ( $d_2 \equiv$  distance from the lens to the film plane), a particular ray's parameters at the pinhole will depend on its angle of departure from the plasma. This applies to any nonparaxial ray whether it be from the plasma generated light or the laser beam. From Equation (9), it can be seen that a pinhole distance equal to the lens focal length will force the A term to zero. Thus, the nonparaxial rays ( $R'_1 \neq 0$ ), most of which are from the plasma light, are blocked by the pinhole.

In order to predict the pinhole size needed to let the refracted laser rays through but still block most of the plasma light,  $d_2$  in Equation (9) is defined to be the

distance from the lens to the pinhole and the maximum  $R_2$  is calculated. For a plasma that is cylindrically symmetric in its density profile,  $R_1$  and  $R'_1$  can be related<sup>12</sup> by

$$\theta(b) = \pi - 2 \int_{r_0}^{\infty} r^{-2} [b^{-2} - r^{-2} - b^{-2} V(r)]^{-1/2} dr \quad (12)$$

where

$$R'_1 = \tan \theta(b)$$

$$R_1 \approx b \equiv \text{impact parameter of the given ray}$$

$$\theta(b) \equiv \text{ray's angle of departure from plasma}$$

$$V(r) = [f_p(r)/f_{\text{wave}}]^2$$

and  $r_0$  is the ray's distance of closest approach to the plasma center (calculated by setting the expression in brackets in Equation (12) equal to zero). Shmoys<sup>12</sup> presents a parabolic distribution for  $V(r)$ :

$$\begin{aligned} V(r) &= V_0 [1 - (r/a)^2], & r < a \\ V(r) &= 0, & r > a. \end{aligned} \quad (13)$$

The resulting analytical solution for  $\theta(b)$  is

$$\theta(b) = \sin^{-1} \frac{V_0 [(b/a)^2 - (b/a)^4]^{1/2}}{\{V_0 (b/a)^2 + [(1 - V_0)/2]^2\}^{1/2}}. \quad (14)$$

For a peak density of  $n_e = 2 \cdot 10^{19} \text{ cm}^{-3}$ ,  $V_0 \approx 0.002$ . Also, from streak photographs of a typical pinch produced by the University of Illinois DPF, the "a" parameter in Equation (13) is estimated to be approximately 1.5 mm. Using these

values in Equation (14) and then in Equation (9), a pinhole size of 2 mm diameter is estimated. However, the 2 mm pinhole also blocks much of the diverging light from the laser light. This in turn reduces the picture area of the pinch so a pinhole of 3 mm diameter was selected to increase the picture size with little effect on fringe visibility.

Since a simple, single lens system is used, it is important to reduce as many lens aberrations as possible by lens shape. Due to the nature of the laser light, only monochromatic aberrations are important. Those most affected by lens shape are spherical aberration and coma. The former type is the failure of rays from a point object on the optical axis to converge to a point image. They actually converge to a small circle at the image plane which indicates the finest detail that the lens can resolve. Coma is a similar effect but for off-axis rays which converge to a comet-shaped configuration. For the case of paraxial rays merging to the focal point of the lens, these aberrations can be minimized by choosing a plano-convex lens with the convex side toward the paraxial light ray source<sup>13</sup>.

The shape and index of refraction of a lens affect the focal spot size through a function  $K(\mu)$  where  $\mu$  is the index of refraction for a given wavelength of light. From third-order, thin-lens aberration theory and from the Fraunhofer diffraction limit for a uniformly illuminated square aperture of side dimension  $a$ , the spot size diameter

can be approximated by

$$s \approx 2f[K(\mu)/2 (D/f)^3 + \lambda/a] \quad (15)$$

where  $D$  is the larger dimension and  $a$  is the smaller dimension of the beam at the lens. For a plano-convex lens<sup>10</sup>

$$K(\mu) = \frac{[\mu^2 - 2\mu + 2/\mu]}{[32(\mu - 1)^2]} \quad (16)$$

From Equation (15) the optimum lens f-number ( $f/D$ ) can be found for which the spot size is minimized:

$$(f/D)_{\text{opt}} = [3fK(\mu)/2\lambda]^{1/4} \quad (17)$$

For  $D = 30$  mm,  $\lambda = 337.1$  nm and  $\mu = 1.47977$  (optical quality synthetic fused silica), we have a focal length  $f=616$  mm and a spot size  $s=22$   $\mu$ m. Due to the smaller cost of standard items, a lens of  $f = 500$  mm and diameter of 50 mm was chosen. As with the other optics in the system, high quality in manufacturing is needed to reduce irregular aberrations such as scratches, digs, surface contamination and inhomogeneities.

For this particular interferometer, a magnification factor of  $M=2$  was chosen due to physical constraints. Therefore, from Equations (10) and (11), the distance from the plasma pinch to the lens must be 750 mm, the distance from the lens to the pinhole must be 500 mm, and the distance from the lens to the film must be 1500 mm. The actual

magnification factor is  $M=2.2$  both horizontally and vertically (Figure 12). The extra 0.2 in  $M$  is within the lens focal length tolerance ( $\pm 5\%$ ).

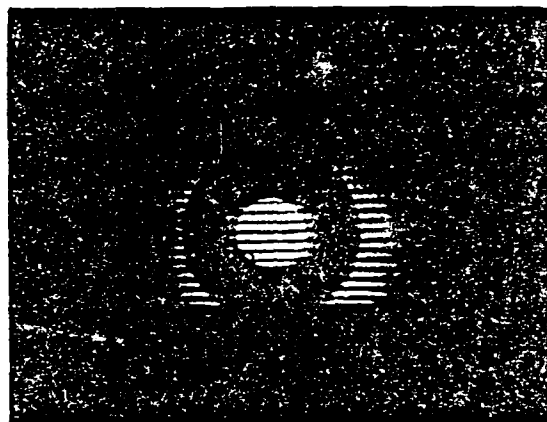


Figure 12. Vacuum interferogram with the image of a washer placed at the center electrode used to check focus and hor./vert. magnification ( $M_H, v=2.2$ ).

#### b. Filters

The second component in the fringe detection stage is the optical filter system. A combination of neutral density filters, each of a different transmittance, was used to experimentally match the laser light intensity to the film sensitivity in order to obtain the highest visibility of the fringe pattern. Also a 337.1 nm bandpass filter of bandwidth  $\pm 6$  nm is placed before the film to reduce plasma and room light. This filter should be placed as close to the film as possible in order to preserve the phase information within

the beam. No such problems occurred with the particular neutral density filters used. These filters were placed near the pinhole. A dark canopy was placed over the detector from the pinhole to the camera back covering the intermediate filter system to prevent room light exposure.

#### c. Film

Originally, the film chosen to record the fringe pattern was Polaroid type 665-negative pack film. Pack film was selected to assist in faster DPF data taking and for general convenience. Type 665 was selected because of the slow speed and therefore smaller sensitivity to background room light. Also, the photograph negatives have much higher resolution than their associated positives (170 line pairs/mm as compared to 17 line pairs/mm for its positive counterpart). A problem with the negatives is that they darken even in dim room lighting, which hampers the fringe readability. Also, the film is relatively expensive and hard to obtain. Because of these reasons, Polaroid type 667-positive pack film was used. This film is comparable to the 665-positive in resolution but is  $\approx 40$  times faster. Neutral density filters with lower transmittance were used to attenuate the beam.

#### D. The Complete Interferometer System

The complete interferometer system is shown in Figure 13. For ease in construction, the laser,

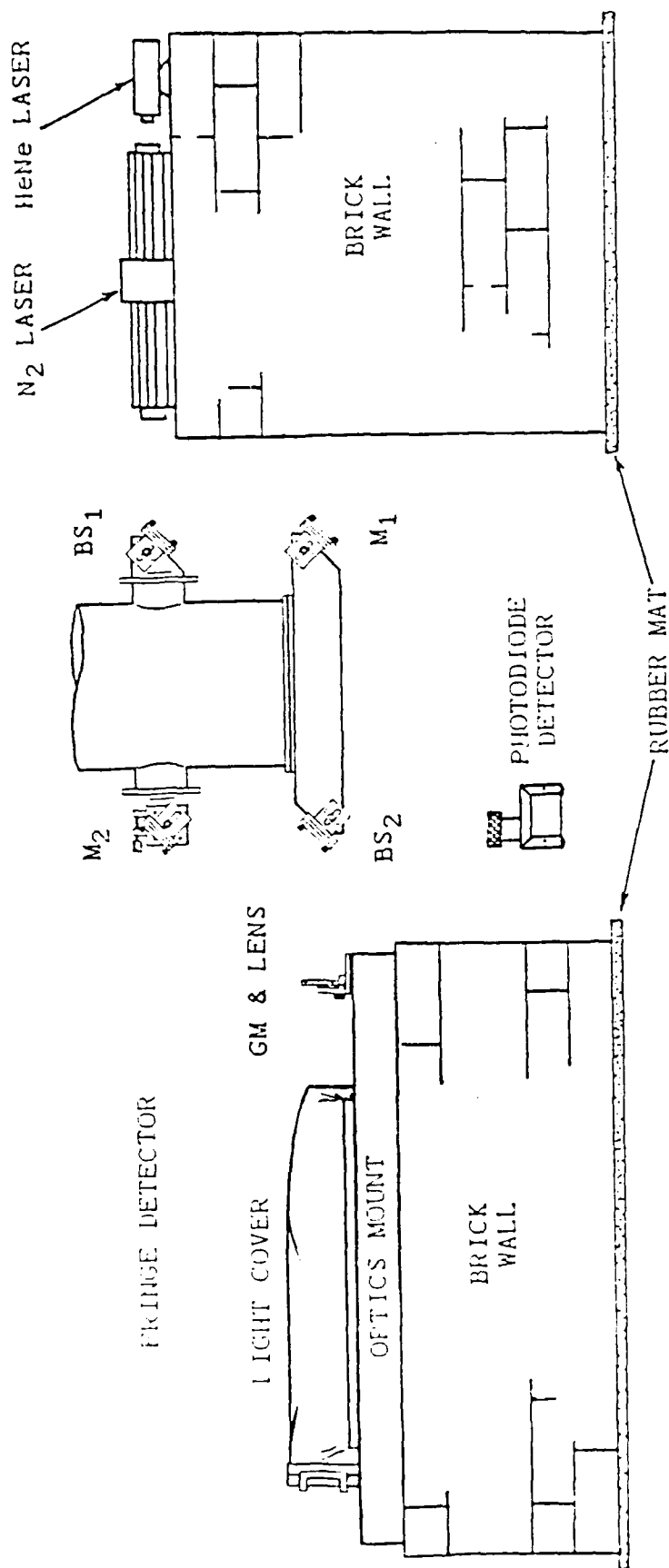


Figure 13. The complete interferometric system used for plasma density measurements in the University of Illinois DPF. The HeNe laser is for alignment. GM, gimbal mount; M, mirrors, BS, beamsplitters.

interferometer optics and detectors are not physically connected. The laser and fringe detector rests on a brick wall with a 1/4 inch rubber mat insulating the components from possible floor vibrations (such as from mechanical pumps) preventing the need for an expensive optics table. The large mass of the wall also protects the laser and fringe detector from most air vibrations that could disrupt critical alignment of the system.



### III. DATA ANALYSIS

Once the fringe profile of the plasma is obtained, the density can be found through Equations (1), (2) and (3). Symmetry conditions are assumed to simplify the analysis. The raw data are numerically transformed into a density profile.

Analytical examples are given as a test of the software and for numerical error analysis.

#### A. Line Density

Line density is the number of particles per unit length. This parameter is useful for the study of particle conservation and axial movement in a dynamic plasma.

The optical phase shift of a ray traversing a chord through a plasma (with respect to vacuum) is given by

$$\delta(x)dx = \frac{dx}{\lambda} \int [\mu(x,y)-1] dy \quad (18)$$

where  $\delta(x)$  is in wavelength units. This is the same as Equation (1) (the  $x$  dependence is included here). Through the use of Equations (2) and (3), Equation (18) can be reorganized to yield

$$\int_{-y}^y n_e(x,y)dy = -2\lambda n_c \delta(x) \quad (19)$$

where  $n_c$  is the critical density where the plasma frequency is equal to the wave frequency. The integration of both sides over the  $x$ -axis will directly give the number of particles per unit length along the  $z$ -axis of the plasma. Therefore, the line density ( $n_l$ ) can easily be calculated from the fringe shift data by using

$$n_l = 2\lambda n_c \int_{-x}^x \delta(x) dx$$

#### B. The Plasma Density (Assuming Axial Symmetry)

Given the geometry of the DPF, a cylindrically symmetric plasma is assumed ( $r^2 = x^2 + y^2$ ). For a ray of width  $dx$  traversing a plasma slice of height  $dz$  with an impact parameter,  $x=b$  (Figure 14), Equation (19) becomes

$$\delta(x) = \frac{-1}{2\lambda n_c} \cdot 2 \int_x^R \frac{n(r)}{\sqrt{r^2 - x^2}} r dr \quad (21)$$

where  $R$  is the outer boundary of the plasma (density is negligible for all  $r \geq R$ ). Equation (21) is a form of the Abel integral and can be inverted to yield

$$n_e(r) = \frac{2\lambda n_c}{\pi} \int_r^R \frac{d\delta(x)}{dx} \frac{dx}{\sqrt{x^2 - r^2}} \quad (22)$$

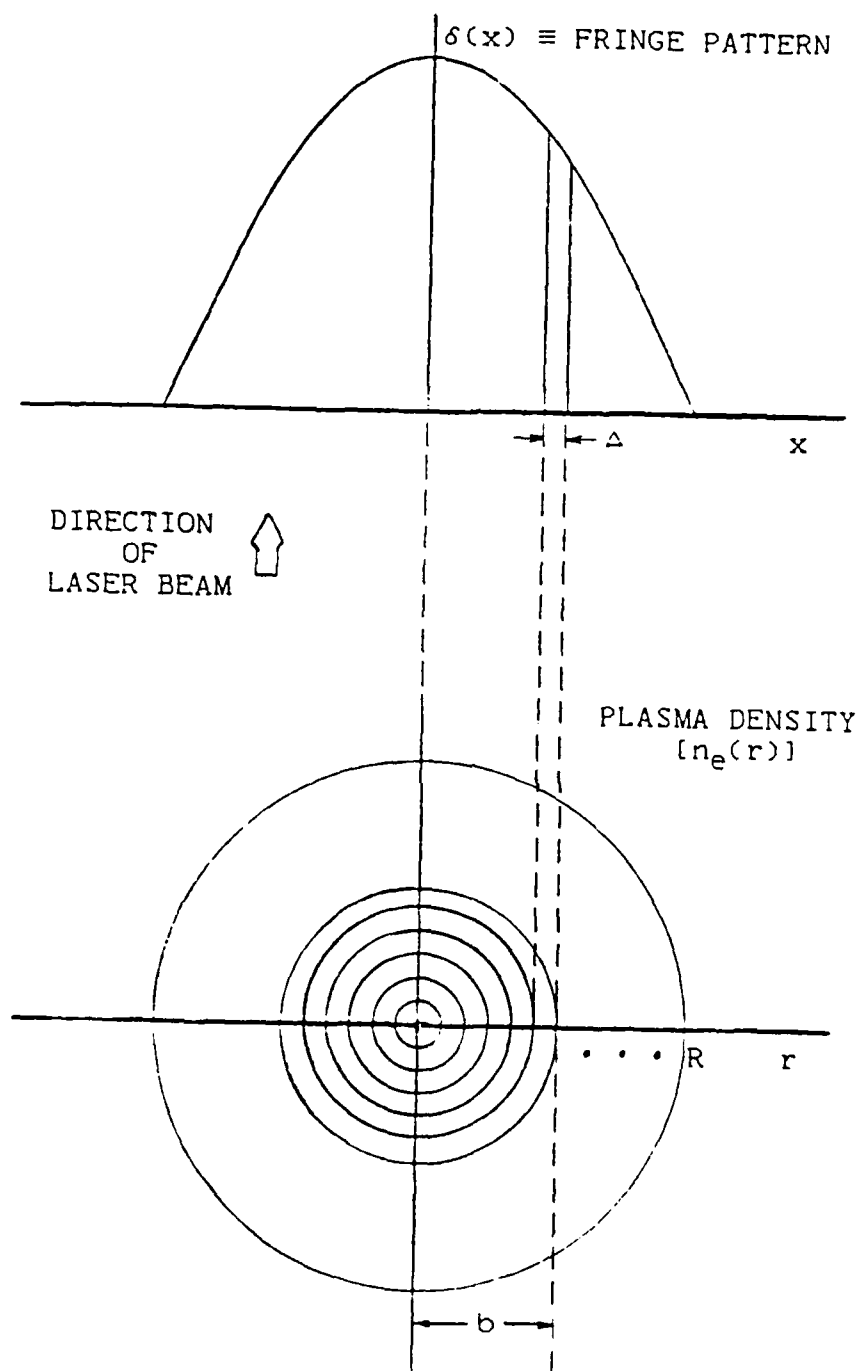


Figure 14. Relationship between fringe pattern and top profile of cylindrically symmetric plasma used for numerical analysis.  $R = \Delta N$ ;  $N = 20$ .

This is the form which is needed to obtain the radial density profile of the plasma from the fringe shift data on the film.

### C. Numerical Analysis

In general, numerical differentiation is much less accurate than numerical integration<sup>14</sup>. The data from the fringe pattern are read in tabular form. As seen from Equation (22), the data must be differentiated and any noise would be greatly amplified, especially at large gradients in the phase shift curve.

William L. Barr<sup>15</sup> introduced a method to numerically solve equations similar to Equation (22). In his method, the order of differentiation and integration is reversed, and a least-squares smoothing technique is applied before the final differentiation. The only assumptions used in his method are that the curve to be inverted is axisymmetric and that its slope on axis is zero.

The accuracy of Barr's method depends on the number of data points used. The use of twenty data points results in good accuracy for Gaussian and polynomial distributions<sup>16</sup>. Such profiles have been observed in other plasma pinch experiments<sup>17, 18, 19</sup>.

Barr divides the x-axis into equal increments  $\Delta$ , such that

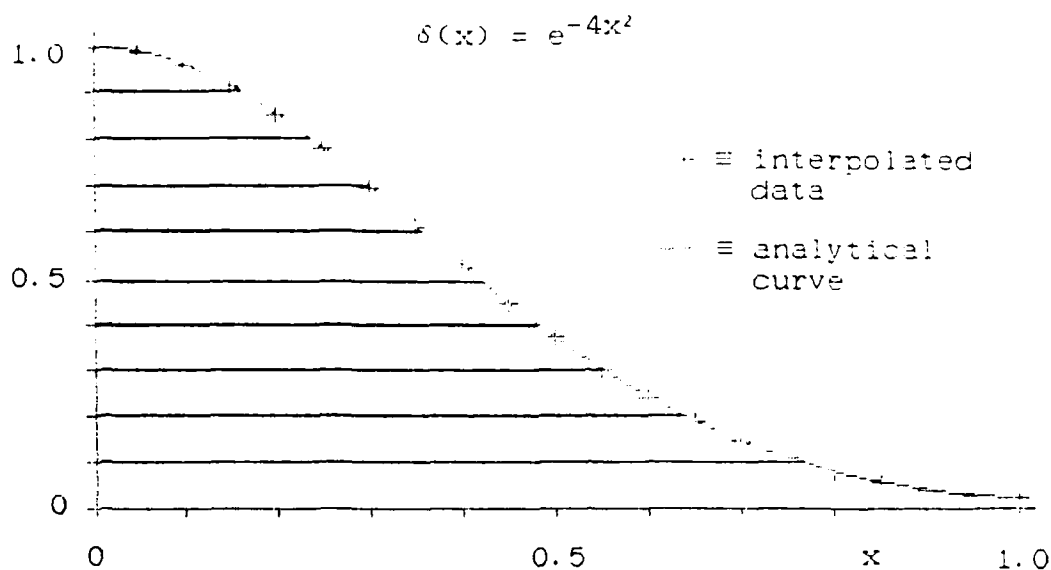
$$x_n = n\Delta, \quad r_k = k\Delta, \quad R = N\Delta \quad (23)$$

where  $n$  and  $k$  are integers between 0 and  $N$ , inclusively. The data, however, are most easily read in equal increments of  $\delta(x)$ . In order to obtain the required  $\delta(x_n)$ , a third-degree Lagrangian interpolating polynomial<sup>14</sup> is used where

$$\begin{aligned} \delta(x_n) = & \delta(x_0) \frac{(x_n - x_1)(x_n - x_2)(x_n - x_3)}{(x_0 - x_1)(x_0 - x_2)(x_0 - x_3)} \\ & + \delta(x_1) \frac{(x_n - x_0)(x_n - x_2)(x_n - x_3)}{(x_1 - x_0)(x_1 - x_2)(x_1 - x_3)} \\ & + \delta(x_2) \frac{(x_n - x_0)(x_n - x_1)(x_n - x_3)}{(x_2 - x_0)(x_2 - x_1)(x_2 - x_3)} \\ & + \delta(x_3) \frac{(x_n - x_0)(x_n - x_1)(x_n - x_2)}{(x_3 - x_0)(x_3 - x_1)(x_3 - x_2)} \end{aligned} \quad (24)$$

Figure 15 demonstrates the method with a Gaussian distribution. A Gaussian was selected since a single polynomial cannot exactly fit it. The interpolation error (excluding roundoff error) is within 0.2% of the peak in the curve.

For a near symmetric  $\delta(x_n)$  distribution, the points on either side of the pinch are averaged in order to obtain the required zero slope at  $x_n=0$ . If the data are not symmetrical, the density on either side of the pinch axis can be separately predicted by mirror imaging the data points of one side over to the other side of  $x_n=0$ . If the data are symmetric but off the chosen pinch axis (such is the case for a  $m=1$  kink instability), the axis of symmetry is taken as  $x=0$



(a)

$x$	$\delta(x)$
0.000	1.0
0.162	0.9
0.236	0.8
0.299	0.7
0.357	0.6
0.416	0.5
0.479	0.4
0.549	0.3
0.634	0.2
0.759	0.1
1.000	0.018

(b)

Figure 15. (a) Diagram showing the transformation of the fringe shift data to equal increments in  $x$ . (b) Input data to the Lagrangian interpolating polynomial of equal increments in  $\delta(x)$ .

for the analysis.

Once the  $\delta(x_n)$  values are determined, Barr's method of inverting the data will smooth any round-off errors. The final form of Equation (22) then becomes

$$n_e(x_k) = \frac{2\lambda n_c}{\pi\Delta} \sum_{n=k-2}^N \beta_{kn} \delta(x_n), \quad k > 2$$

$$n_e(x_k) = \frac{2\lambda n_c}{\pi\Delta} \sum_{n=0}^N \beta_{kn} \delta(x_n), \quad k \leq 2 \quad (25)$$

where  $\beta_{kn}$  are constants that include the entire integration, least-squares fitting, and the final differentiation process of the  $\delta(x_n)$  curve. The  $\beta_{kn}$  values are listed in Table 2.

#### D. Analytical Examples and Numerical Error Analysis

The equations from the last section are included in a computer program. The software was written to accept the raw data read from the photographs as input. The phase and density profiles are calculated and graphically displayed.

The input data are expected to be between  $\delta(-x)=0$  and  $\delta(x)=0$  with the axis of the pinch at  $x=0$ . Although these endpoints are not used in Barr's method of inversion, they are included in the Lagrangian interpolating polynomials for better accuracy of  $\delta(x)$  near the endpoints. The data are interpolated to obtain 20 equidistant points on each side of the axis where the separation is given by  $\Delta=x_{\max}/21$  where

Table 2. The coefficients  $\beta_{kn}$  ( $\cdot 10^4$ )

$n \backslash k$	0	1	2	3	4	5	6	7	8	9	10	11	12	13	14	15	16	17	18	19	20
0	-2029	-1831	-1239																		
1	-4439	-4041	-2847	-1324																	
2	-1791	-1778	-1740	-1936	-1172																
3	5111	4342	2034	-928	-1523	-1036															
4	1298	1299	1304	964	-722	-1291	-930														
5	95	204	531	969	538	-535	-1140	-847													
6	237	262	338	501	810	330	-586	-1032	-781												
7	193	203	235	292	464	714	214	-551	-951	-727											
8	152	157	173	202	260	431	646	142	-524	-886	-682										
9	122	125	134	150	179	236	403	595	95	-501	-834	-644									
10	99	101	107	117	133	162	217	380	555	63	-482	-790	-612								
11	82	84	87	94	104	120	148	202	359	522	39	-465	-752	-583							
12	69	70	73	77	84	94	111	138	189	342	495	22	-450	-720	-558						
13	59	60	61	65	69	76	87	103	129	179	326	471	9	-437	-691	-536					
14	51	51	53	55	58	63	70	81	96	122	170	313	450	-1	-424	-666	-517				
15	44	45	46	47	50	53	58	65	75	91	115	162	301	432	-9	-413	-643	-499			
16	39	39	40	41	43	46	49	54	61	71	86	110	155	290	416	-15	-402	-623	-483		
17	35	35	35	36	38	40	43	46	51	58	67	82	105	149	280	402	-20	-393	-604	-468	
18	31	31	32	32	33	35	37	40	43	48	55	64	78	101	144	271	389	-24	-384	-587	-455
19	28	28	28	29	30	31	33	35	37	41	46	52	61	75	97	139	263	377	-28	-375	-571
20	25	25	25	26	27	28	29	31	33	35	39	44	50	59	72	94	135	256	367	-30	-367



$x_{\max}$  is the larger absolute  $x$  value from  $\delta(-x)$  and  $\delta(x)$ . This is a prerequisite of using Barr's method of inversion (here,  $R=20\Delta$ ). The interpolated data on either side of the phase profile axis ( $x=0$ ) are then averaged in order to obtain the cylindrically symmetric profile in  $r$  which is required for Abel inversion. After the inversion is performed, the density magnitude at each point  $r_k=k\Delta$  ( $0\leq k\leq 20$ ) is acquired.

To obtain a more uniform display of the density graphics, the inverted data are again interpolated, using third-degree Lagrangian polynomials to fill in the spaces between  $r_k$ . The program is straightforward and is not listed here.

To test the above method, two representative functions are assumed, and their analytical solutions are compared to the program results. The first function is a Gaussian phase profile:

$$\delta(x) = e^{-x^2/a^2} . \quad (26)$$

A Gaussian profile is a good test since a low-order polynomial cannot exactly fit it and because it is sharply peaked. The analytical solution for the Abel inversion of Equation (26) (as  $R$  approaches  $\infty$ ) is

$$A(r) = \frac{1}{\sqrt{\pi}a} e^{-r^2/a^2} . \quad (27)$$

Although the numerical method can not approach this limit ( $\delta(r)=0$  for  $r>R$ ), the error is negligible for large enough values of  $R$ . The numerical and analytical inversions of Equation (26) are compared in Figure 16 for  $a=\frac{1}{2}$ . The maximum error is within 2% of the peak value of which 1% is from the round-off to 2 decimal places.

The second test function is a third-order polynomial in  $x^2$ . This curve represents a hollow density profile. The function can be written, in general, as

$$\delta(x) = a+bx^2-cx^4+dx^6. \quad (28)$$

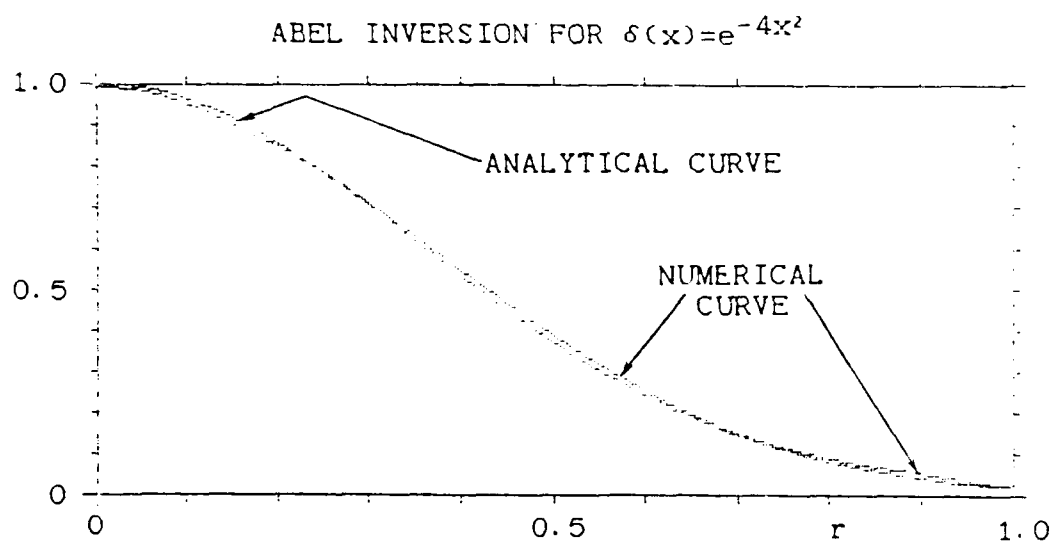
The solution for the analytical inversion is

$$A(r) = \frac{-2}{15\pi} \sqrt{R^2-r^2} [(24d)r^4+(12dR^2-20c)r^2+(9dR^4-10cR^2+15b)] . \quad (29)$$

The constants in Equation (28) are chosen such that the magnitude and slope of  $\delta(x)$  at  $x=1$  are equal to zero. This makes the obvious choice for  $R=1$ . For  $a=1$ ,  $b=2$ ,  $c=7$  and  $d=4$ , Equation (29) becomes

$$A(r) = \frac{-8}{15\pi} \sqrt{1-r^2} [24r^4-23r^2-1] . \quad (30)$$

In Figure 17, the numerical method is compared to Eq. (30).

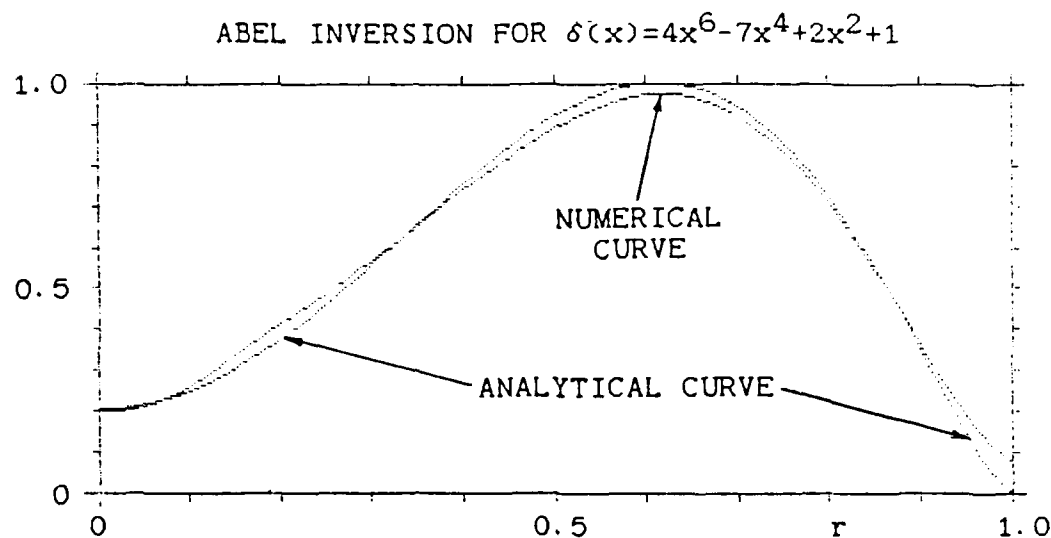


(a)

$x$	$\delta(x)$
0.00	1.0
0.16	0.9
0.24	0.8
0.30	0.7
0.36	0.6
0.42	0.5
0.48	0.4
0.55	0.3
0.63	0.2
0.76	0.1
1.00	0.0

(b)

Figure 16. (a) Comparison between the numerical and the analytical Abel inversions for a Gaussian profile (max. error = 2%).  
 (b) Program input data, incremental in  $\delta(x)$ .



(a)

x	$\delta(x)$
0.00	1.0
0.25	1.1
0.60	1.0
0.65	0.9
0.69	0.8
0.72	0.7
0.76	0.6
0.79	0.5
0.82	0.4
0.85	0.3
0.88	0.2
0.92	0.1
1.00	0.0

(b)

Figure 17. (a) comparison between the numerical and the analytical Abel inversions for a third order polynomial in  $x^2$  (max. error = 4%). (b) Program input data, incremental in  $\delta(x)$ .

The large error in the numerical curve near  $r=1$  is caused by the sharp curvature and low values in  $\delta(x)$  in this region. However, the curve generated numerically is meaningless beyond  $r=0.95$  since  $A(r)$  does not go to zero at  $r=1.0$ . The corresponding points are not used in the experimental data inversions. The maximum error generated through the numerical inversion is therefore within 4% of the maximum value in the region of interest.

#### IV. DATA

The plasma formed by the dense plasma focus is short lived (typically  $< 100$  ns). The jitter of the laser trigger must be minimized in order to accurately determine the timing of the interferogram exposure with respect to the dynamic plasma. The last section in this chapter is on error margins for the measured densities.

##### A. Timing

The jitter time of the pulse used to trigger the oscilloscope, and therefore the laser (see Figure 5 in Chapter II), is critical since the plasma changes rapidly with time. The best start pulse signal seems to be given by the voltage induced in a small magnetic probe placed between the inner and outer electrodes (also used to determine the pinch current). The trigger system then bypasses any jitter created during the initial breakdown of the gas along the base insulator of the DPF but is also early enough to accommodate for electronic equipment delay.

A good timing reference can be obtained by comparing the time of the laser output to that of the soft x-ray signal from the plasma. The soft x-rays peak at maximum plasma densities<sup>3</sup> (maximum plasma compressions). A recent comparison of x-ray peaks with laser pulses confirms the timing reported in the data section.

## B. Results

The dynamic behavior of the plasma in the DPF can be separated into three stages (Figure 18):

1. first compression.
2. radial expansion and
3. second compression (plasma breakup).

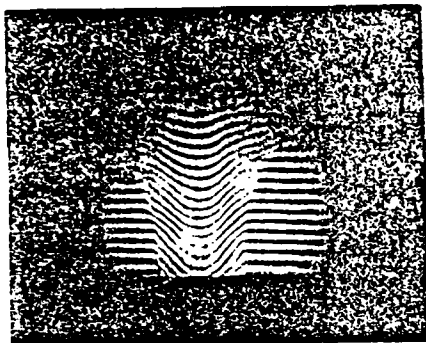
The first compression lasts for approximately 15 ns in the University of Illinois dense plasma focus at the end of which a dense plasma column is formed. The column then bounces radially outward (radial expansion phase). This phase can last for  $\approx 20$  ns. Finally, a second compression of the plasma occurs in which the pinch column breaks up. The plasma breakup, typically caused from  $m=0$  (sausage) instabilities, lasts typically less than 25 ns.

Included in this section are representative interferograms and their respective density profiles as a function of  $r$  and  $z$  (radial and axial dimensions) for the three pinch phases (although from different shots). The initial fill gas for all data is deuterium and the input energy is 12.5 kJ. The error is within 10% of the maximum density for each profile along the  $z$ -axis (see Section C. of Chapter IV).

### 1. The First Compression

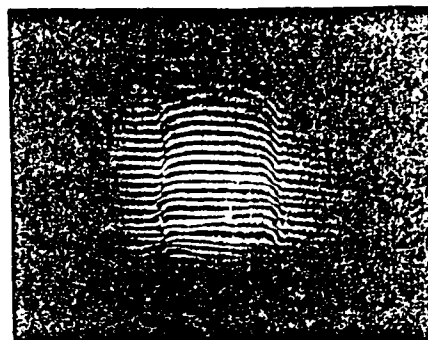
The collapse phase is recognized by the

1st COMPRESSION

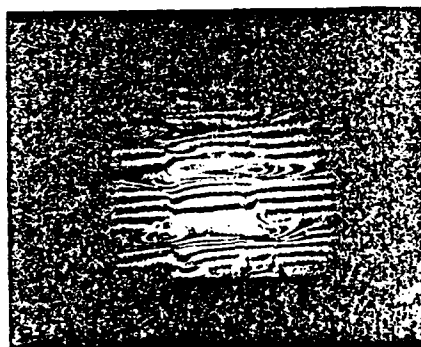


(a)

RADIAL EXPANSION



(b)

2nd COMPRESSION  
(PINCH BREAKUP)

(c)

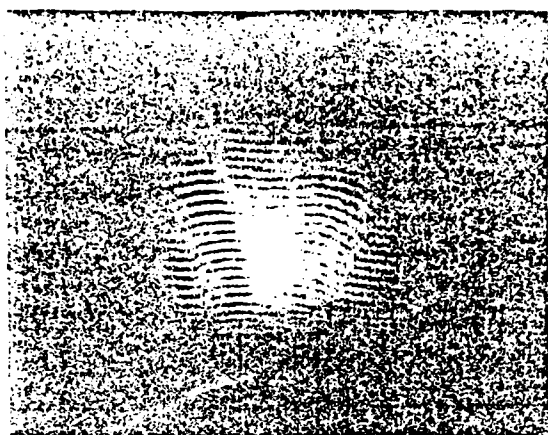
Figure 18. Phase shift data of (a) the first compression stage of the pinch cycle:  $P=3.5$  torr ( $H_2$ ),  $V_0=26$  kV, (b) the radial expansion phase:  $P=3.2$  torr ( $D_2$ ),  $V_0=25$  kV and (c) the second compression from which the plasma is breaking up due to  $m=0$  instabilities:  $P=3.5$  torr ( $H_2$ ),  $V_0=26$  kV. The flat at the bottom of the fringes is the center electrode. It is noted here that sometimes the fringes appear inverted. This is due to the sign of the angle between the reference and probe waves upon recombination and is not a problem for analysis. The magnification for all interferograms is 2.2 unless otherwise specified.



characteristic shape and smooth edges of the fringe profiles as shown in Figures 19-21. Although these edges are produced by the current sheath surrounding the plasma, no evidence of dangerous instabilities is present. Figures 19 and 20 are of the early collapse phase. Figure 19 is earlier than Figure 20 as noted from the larger radius, lower density and hollow profile. The plasma in Figure 19 seems to be, for the most part, from the current sheath, although some new plasma seems to be forming at the sheath front.

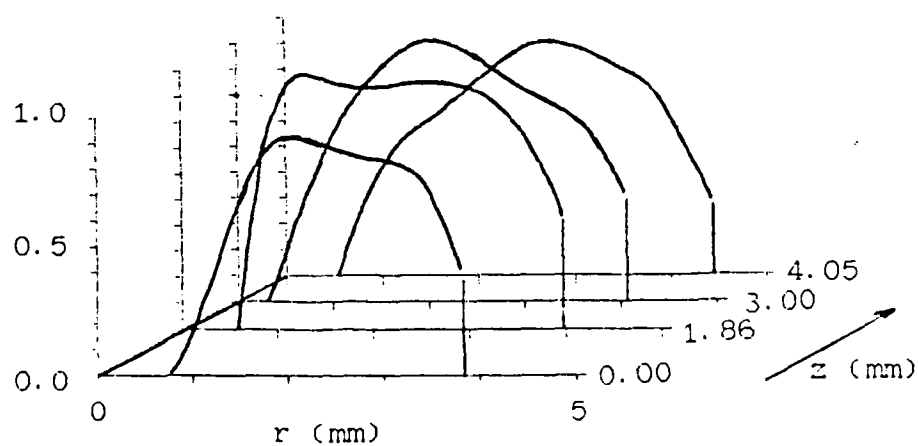
The density profile of Figure 20 suggests that pinching of the plasma has begun. The peak density is more than a factor of three greater than that of Figure 19. Also, the density profile is no longer hollow. The flat portion of the profiles is closed to that of the uncompressed plasma of Figure 19 suggesting this portion of the plasma is still collapsed. Both figures are from a fill pressure of 3.2 torr.

Figure 21 shows the end of the first compression when the density is maximum and the radius is minimum. The minimum radius occurs between 2 mm and 5 mm from the hollow center electrode (3.5 mm on the average) and is characteristically  $\approx 1$  mm (FWHM) as previously observed with streak photographs<sup>21</sup> of the visible light. The shape of the profile at  $z=1.87$  mm in Figure 21 and the high density ( $\approx 10^{19} \text{ cm}^{-3}$ ) suggest that the plasma is at maximum compression.



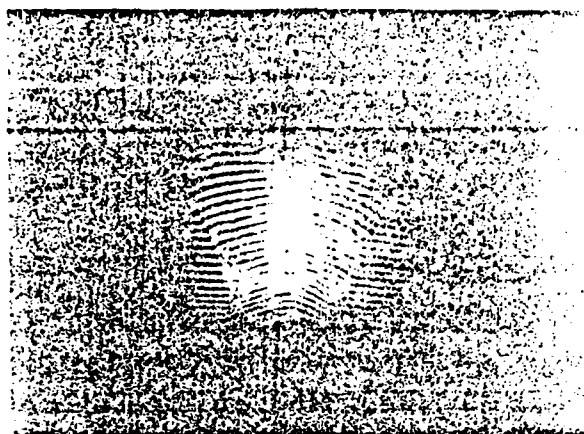
(a)

PLASMA DENSITY  
(SCALE:  $1.0 = 1.6 \cdot 10^{18} \text{CM}^{-3}$ )



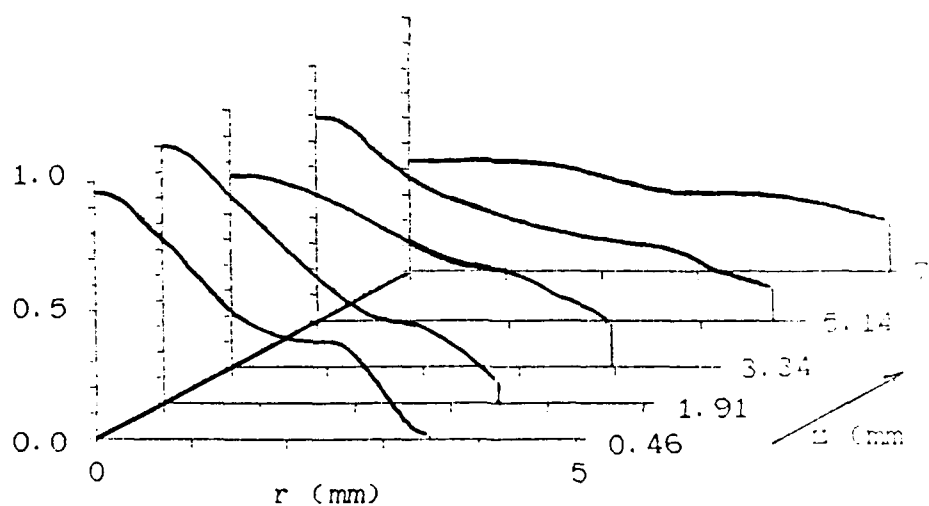
(b)

Figure 19. (a) Interferogram and (b) electron plasma density of the current sheath entering the first compression phase:  $P=3.2$  torr ( $D_2$ ),  $V_0=25$  kV.



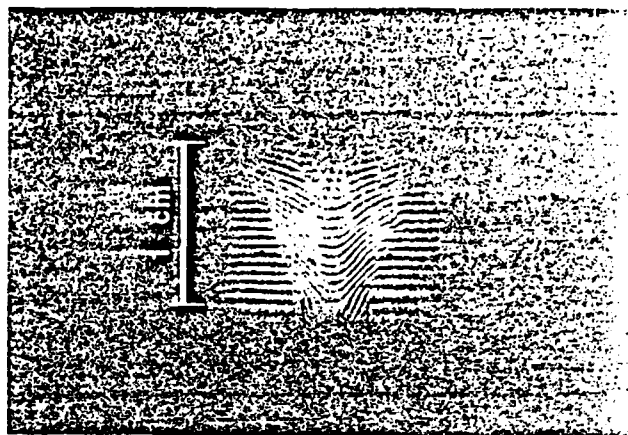
(a)

PLASMA DENSITY  
(SCALE: 1.0 =  $5.8 \cdot 10^{18} \text{CM}^{-3}$ )

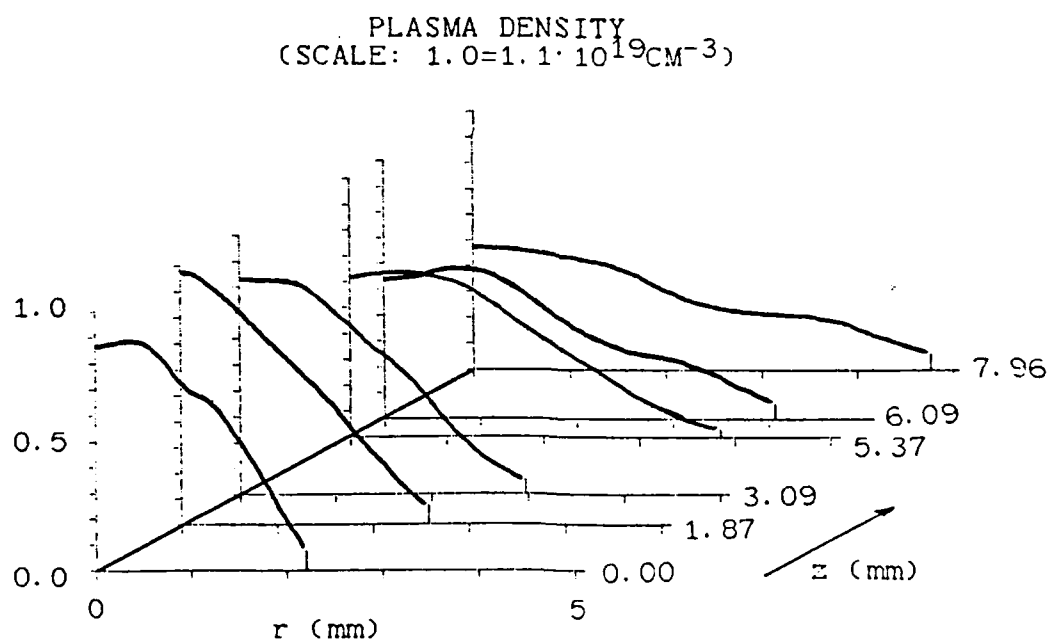


(b)

Figure 20. (a) Interferogram and (b) electron density profile of the plasma entering the first compression phase where the plasma is starting to pinch:  $P=3.2$  torr (0.4%),  $V_0=25$  kV.



(a)



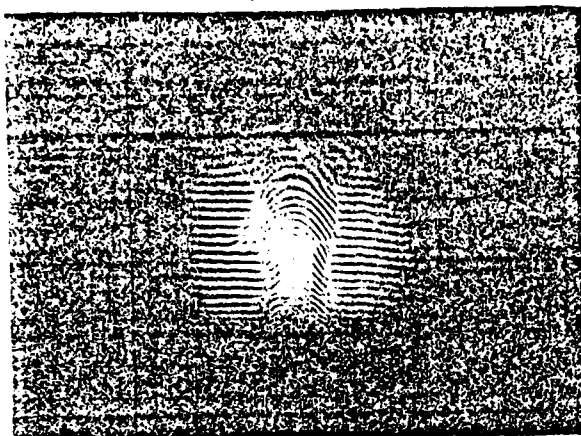
(b)

Figure 21. (a) Interferogram and (b) electron density profile of the pinch at maximum compression:  $P=3.9$  torr ( $D_2$ ),  $V_0=25$  kV.

Due to the lack of x-ray timing for the interferogram in Figure 22, and since this plasma configuration has not been observed since, it is not clear what stage the pinch was in. The high density ( $>10^{19}\text{cm}^{-3}$ ) and small minimum radius ( $<1\text{ mm}$  at  $z=2.82\text{ mm}$ ) suggest that the pinch is near maximum compression.

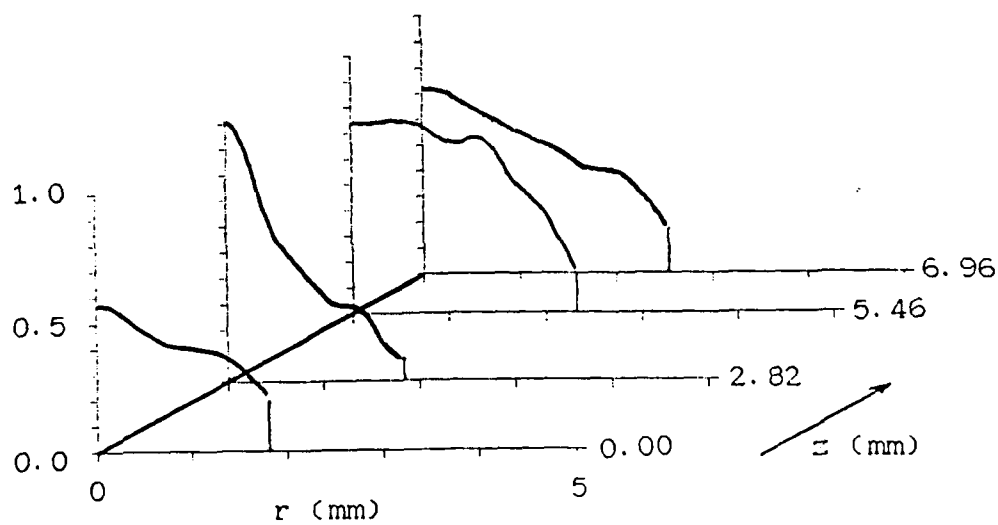
Disturbances, similar to the one at the outer left side in Figure 22, typically occur in pinches before maximum compression (from more recent x-ray timed interferograms). Disturbances are also evident at the right side of the interferogram of Figure 21. These disturbances do not occur at the minimum radius of the pinch as would be expected according to the Kruskal-Schwarzschild Theory<sup>23</sup>. Such occurrences have been reported in other DPF/ $\text{N}_2$  interferometry experiments<sup>17,18,19</sup> but not much has been said about them because they disappear during the plasma expansion. The disturbances seem to be weak instabilities of long wavelength, since it has been reported<sup>18</sup> that they only appear in longer plasma columns. From analysis of the fringes in these disturbances (not included here), the density in the region is typically of low magnitude ( $\approx 15\%$  of  $n_{e\text{-max}}$  in Figure 22).

The average line density over several first compression data is  $\approx 7.8 \cdot 10^{17}/\text{cm}$  at the tip of the center electrode and  $\approx 1.4 \cdot 10^{18}/\text{cm}$  at 1 cm above the center electrode indicating mass flow along the axis.



(a)

PLASMA DENSITY  
(SCALE:  $1.0 = 1.3 \cdot 10^{19} \text{CM}^{-3}$ )



(b)

Figure 22. (a) Interferogram showing a disturbance at the outer left side and (b) electron density profile of the plasma thought to be near maximum compression:  $P = 3.2$  torr ( $\text{D}_2$ ),  $V_0 = 25$  kV.

## 2. The Radial Expansion

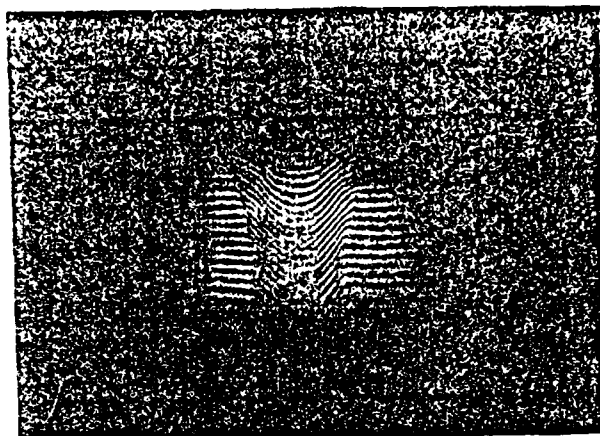
The profile of Figure 23 at  $z=1.41$  mm (minimum radius) shows a wave of plasma starting its radial expansion phase (the "hump" in the profile resembles the profiles in the expansion phase of Figure 24). The expansion appears to be occurring before the maximum compression at larger  $z$  (zippering). Similar pinch profiles have been used in the modeling of pinch dynamics<sup>22</sup>.

Figure 24 shows the plasma at maximum expansion. The radius of the plasma at this stage is typically three times the minimum radius of the first compression and the density profile is hollow. Also, the plasma configuration is generally cylindrical as compared to the curved nature of the first compression stage. The edges of the fringe pattern tend to wiggle rapidly along the  $z$ -direction indicating short wavelength instabilities in their initial stage<sup>1</sup>.

Increasing densities along the pinch axis in the profiles of Figure 24 also suggest axial mass flow away from the center electrode. The fill pressures for the expansion data are as given in the figure captions.

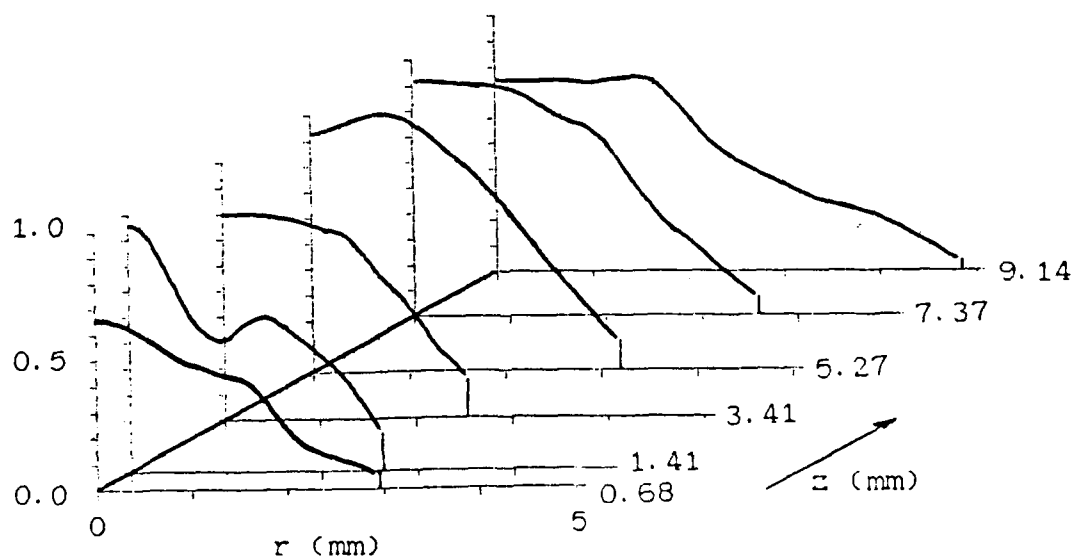
## 3. The Second Compression (Plasma Breakup)

The fringe data for this stage are generally not symmetrical and cannot be inverted to get the density profiles. Thus, only the interferograms are shown. However, the peak densities can be estimated by using selected



(a)

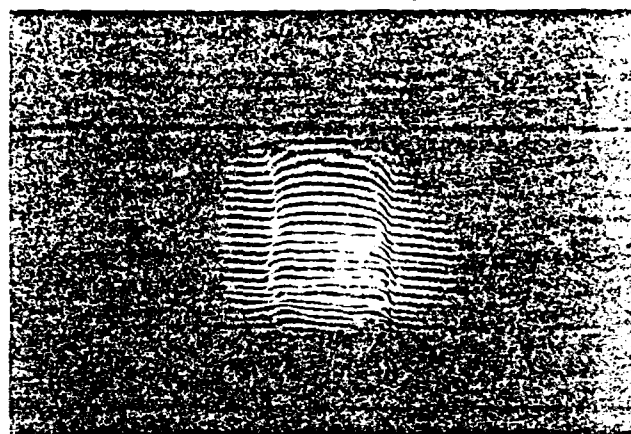
PLASMA DENSITY  
(SCALE:  $1.0 = 8.2 \cdot 10^{18} \text{CM}^{-3}$ )



(b)

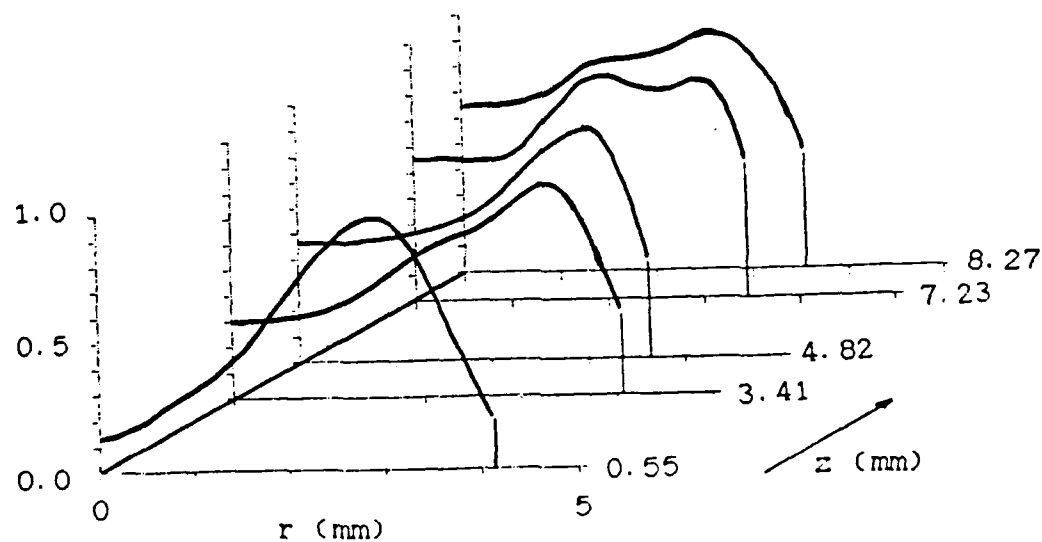
Figure 23. (a) Interferogram and (b) electron density profile of the plasma entering the radial expansion phase:  $P=4.4$  torr ( $D_2$ ),  $V_0=25$  kV.





(a)

PLASMA DENSITY  
(SCALE:  $1.0 = 2.6 \cdot 10^{18} \text{ cm}^{-3}$ )



(b)

Figure 24. (a) Interferogram and (b) electron density profile of the plasma at maximum expansion:  $P=3.2$  torr ( $D_2$ ),  $V_0=25$  kV.

fringes.

The instabilities of Figure 25 seem to have grown to the dangerous stage just before pinch breakup occurs. The wavelengths of the instabilities are longer than the rapid wiggles of Figure 24.

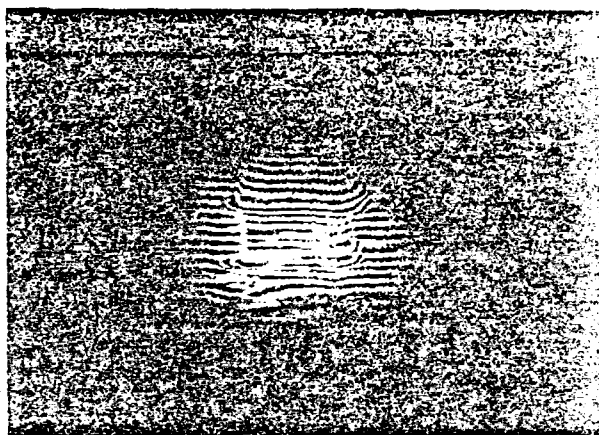


Figure 25. Interferogram of the pinch at the start of the second compression. The  $m=0$  instabilities responsible for the plasma destruction are forming at the edges of the fringes.

Figure 26 consists of four fringe patterns of the plasma well into the breakup phase. These photos and others not reproduced in this thesis reveal that  $m=0$  instabilities are almost always responsible for the plasma destruction, although  $m=1$  (kink) instabilities have been observed. From the interferograms, the wavelength of the most rapidly growing instabilities was measured and varies from 2 mm to 4 mm.

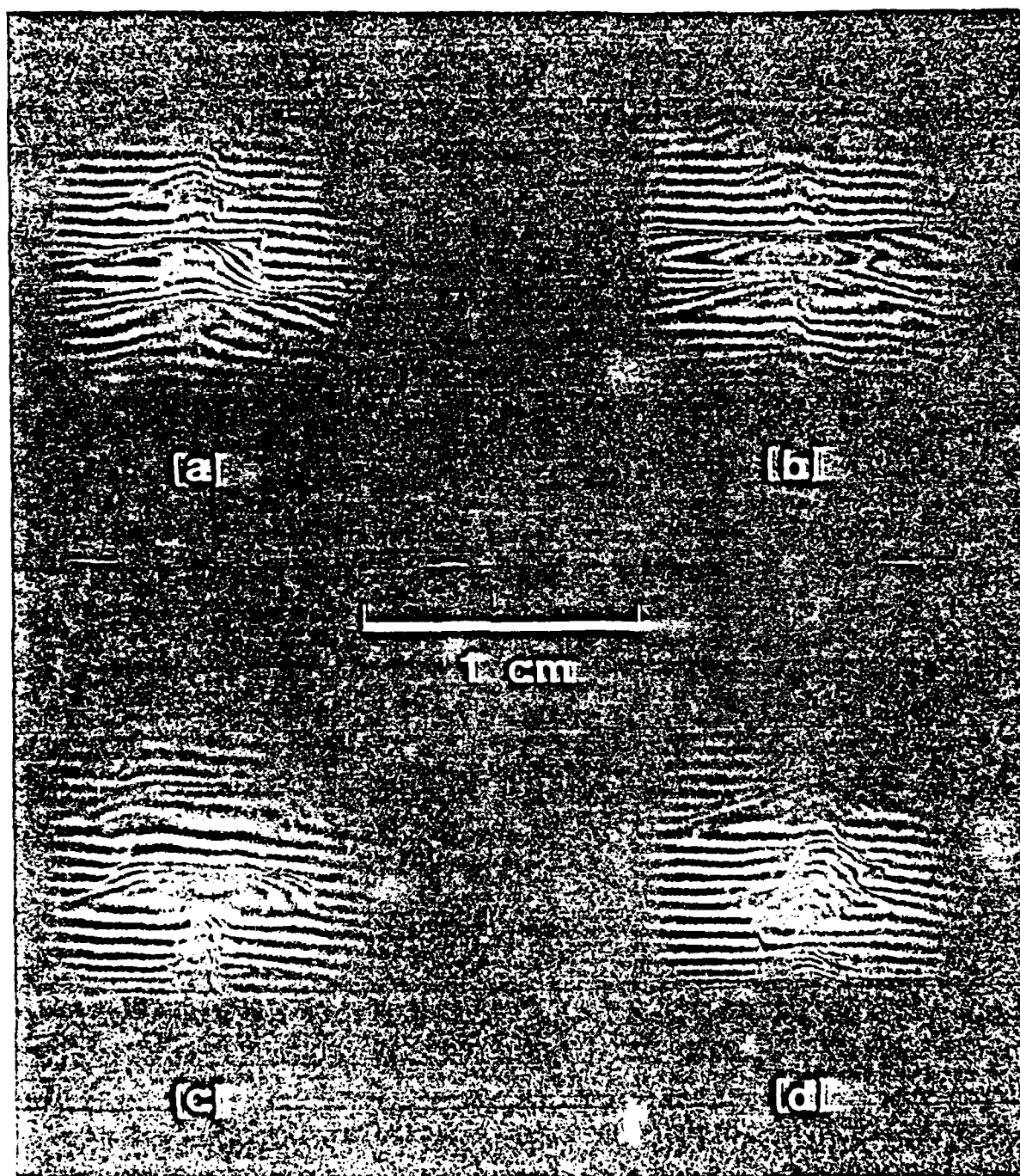


Figure 26. (a), (b), (c) and (d) are four interferograms showing the  $m=0$  instabilities that break up the plasma during the second compression.  $P_0=3.2$  torr and  $V_0=25$  kV for (a) through (d).

The densities in the constricted regions of the instabilities approach  $2 \cdot 10^{19} \text{cm}^{-3}$ . The density in the "blobs" is around  $4 \cdot 10^{18} \text{cm}^{-3}$ , and the line density is  $n_l \approx 10^{17} / \text{cm}$ , which is an order of magnitude larger than in the constricted regions. The use of line densities also demonstrates that particle conservation is not preserved along the pinch axis between stages. It is believed that the particle loss is mostly out the ends of the pinch because of the z-component of the kinetic pressure (away from  $r_{\min}$ ) and lack of confinement in this direction.

#### C. Error Margins

The largest error incorporated into the density profiles comes from the reading of the fringe patterns. The data were read in 1/2-fringe increments as a function of  $x$  using a vernier caliper of 0.1 mm resolution. By progressively shifting the original data for several profiles from  $x=0 \pm 0$  mm to  $x=R \pm 0.1$  mm in a linear fashion, a typical error margin is calculated to be less than  $\pm 3\%$  of  $n_{e-\max}$ . The method was chosen since a particular point of the density profile depends only on the larger radius points in the fringe profile when the data are Abel inverted. With the addition of the numerical error calculated in Chapter III, it can be argued that the measured densities are well within  $\pm 10\%$  of  $n_{e-\max}$ . From Figures 16 and 17 of Chapter III, it is seen that the measured densities underestimate the real

values at the peaks and overestimate the real values near the edges. The error in the line density calculations can be assumed to be within  $\pm 5\%$  of the real values. This is because the Abel inversion was not needed in their determination, and the same polynomials used to interpolate the data were also used to integrate them.

## V. SUMMARY AND CONCLUSIONS

The purpose of this work was to measure the electron density of a dense plasma focus with the use of laser interferometry. A nitrogen laser was used as the probe beam, since it fulfilled all of the requirements imposed by the high density and short duration of the plasma. The rest of the equipment needed for this research has been discussed in detail. Also discussed were the numerical methods and assumptions used to obtain the density profiles as a function of the radial and axial dimensions.

The electron density in the University of Illinois plasma focus is on the order of  $10^{19}\text{cm}^{-3}$  at maximum compression. By observing the different phases in the plasma event leading to and following the maximum compression, the dynamics of the pinch is better understood. The radius of the pinch at maximum compression is  $\approx 1$  mm and then expands to a cylindrical shape with radius  $\approx 3$  mm before plasma breakup when the current stops flowing. The breakup is almost always caused by  $m=0$  instabilities although  $m=1$  instabilities have been observed.

The Mach-Zehnder interferometer is now being used to understand the pinch dynamics when impurities are added to the initial gas fill (such as neon) and/or an axial magnetic field is added at the pinch axis. Preliminary results of 5% Ne added to  $\approx 3$  torr hydrogen show a much tighter and

straighter pinch at first compression. The magnetic field ( $\approx 500$  Gauss) stabilizes the pinch from  $m=0$  instabilities but not from  $m=1$  instabilities. Perhaps a stronger axial field will reduce the  $m=1$  instabilities and prolong the confinement time of the plasma.

## APPENDIX I. FRINGE SHIFT OF A WAVE IN A DIELECTRIC

The purpose of this Appendix is to demonstrate simply the relationship between fringe shift,  $\delta(y)$ , and index of refraction,  $\mu(y)$ , of a lossless dielectric of length  $L$  in one arm of a Mach-Zehnder interferometer (Figure I.1). The fringe shift,  $\delta(y)$ , is found for one ray of cross-sectional area  $dx \cdot dz$  in an infinite plane wave.

Written in phasor notation, a wave travelling in the  $y$  direction can be expressed by

$$E = E_0 e^{-j(\omega t - \beta y)} \quad (I.1)$$

where  $E_0$  is the constant wave amplitude,  $\omega$  is the radial wave frequency and  $\beta$  is the phase coefficient. Equation (I.1) can similarly be written as

$$E = E_0 e^{-j(vt - y)} \quad (I.2)$$

where  $v$  is the phase velocity of the wave. In fact,

$$v = \frac{\omega}{\beta} = \frac{c}{\sqrt{\epsilon_r}} \quad (I.3)$$

in a nonmagnetic material (Appendix II), where  $c$  is the speed of light in vacuum and  $\epsilon_r$  is the relative permittivity of the



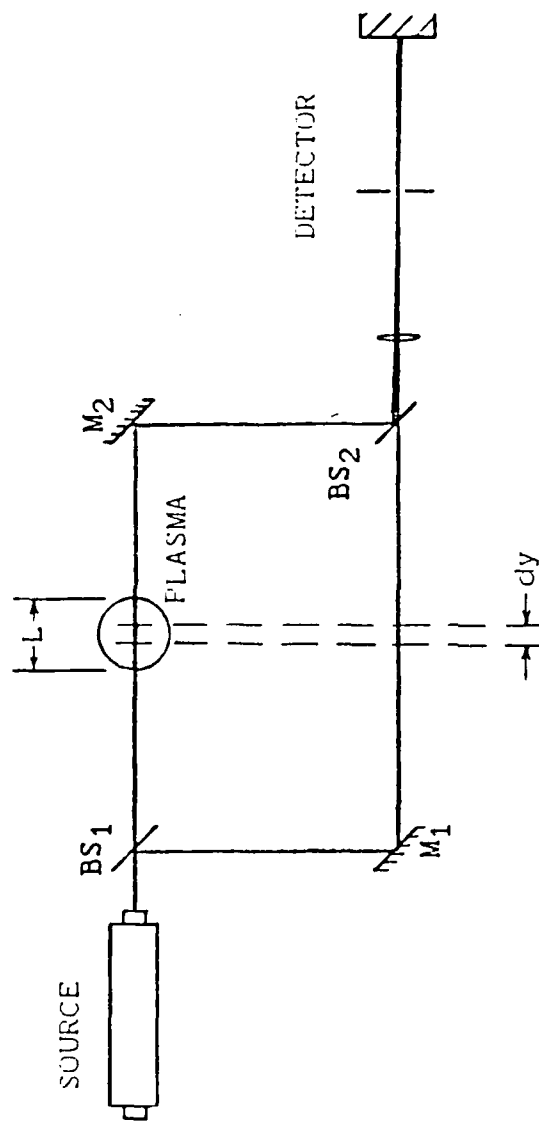


Figure I.1. Schematic used for the fringe shift of a plasma of length  $L$  (with respect to free space) in a Mach-Zehnder interferometer. The differential change is in the length  $dy$ .

medium. The index of refraction is related to the relative permittivity by

$$\mu = \sqrt{\epsilon_r} . \quad (I.4)$$

It is obvious that a material of different index in one arm of a Mach-Zehnder interferometer will cause a change in phase velocity with respect to the wave in the other arm. The phase shift caused by this change is

$$d\delta = \frac{f}{v_p} - \frac{f}{v_v} dy \quad (I.5)$$

where  $v_p$  and  $v_v$  are the phase velocities of the waves in the medium and in the vacuum, respectively.

Equation (I.5) can be simplified by noting that

$$\frac{f}{v_p} = \frac{\mu}{\lambda} \quad (I.6)$$

and

$$\frac{f}{v_v} = \frac{1}{\lambda} . \quad (I.7)$$

By using Equations (I.6) and (I.7) in Equation (I.5) and then integrating on both sides, the phase shift (fringe shift) due to the inserted material is found:

$$\delta = \frac{1}{\lambda} \int_L [\mu(y) - 1] dy . \quad (I.8)$$

## APPENDIX II. APPROXIMATIONS FOR PLASMA INDEX

The purpose of this Appendix is to demonstrate that the refractive index for the dense plasma focus can be approximated by

$$\mu = \left(1 - \frac{\omega_p^2}{2\omega^2}\right) \quad (\text{II.1})$$

which is effectively the same as Equation (2) in Chapter I, except that the radial wave frequency is used ( $\omega=2\pi f$ ). The major effects on the plasma index are from the electron collision frequency with heavy particles ( $\nu_e$ ), the electron cyclotron frequency ( $\omega_b$ ), and the plasma frequency ( $\omega_p$ ). It is also of concern that the wave frequency is not near the upper hybrid resonance frequency, ( $\omega_{uh}$ ). Note that if the following approximations hold for the electrons, they will also hold true for the ions due to their larger mass.

The electron collision frequency can be written<sup>7</sup>

$$\nu_e = 2.91 \cdot 10^{-6} n_e \lambda_{ei} T_e^{-1.5} \quad (\text{II.2})$$

where the Coulomb logarithm for electron-ion collisions,  $\lambda_{ei}$ , is given by

$$\lambda_{ei} = 24 - \ln(n_e^{1/2} T_e^{-1}) \quad (\text{II.3})$$

For a maximum density<sup>3</sup> of  $n_e = 2 \cdot 10^{19} \text{ cm}^{-3}$  and an electron temperature<sup>3</sup> of 500 eV, the collision frequency is  $\nu_e \approx 4 \cdot 10^{10} / \text{sec}$ . The radial wave frequency ( $N_2$ ) is  $\omega = 5.6 \cdot 10^{15} / \text{sec}$  and the plasma frequency for the given density is  $\omega_p = 2.5 \cdot 10^{14} / \text{sec}$ . The conditions

$$\nu_e^2 \ll \omega^2 - \omega_p^2 \quad (\text{II.4})$$

and

$$\nu_e^2 \ll \omega^2 (\omega^2 - \omega_p^2)^2 / \omega_p^4 \quad (\text{II.5})$$

are satisfied, and the refractive index can be approximated by<sup>6</sup>

$$\mu^2 = \left(1 - \frac{\omega_p^2}{\omega^2}\right) \quad (\text{II.6})$$

The binomial expansion can be used to arrive at Equation (II.1), since  $\omega_p^2$  is much less than  $\omega^2$  (typically  $\omega_p < 0.1\omega$ ).

Since a magnetic field is associated with the pinch, the plasma is anisotropic. In other words, the refractive index is a function of both the direction of propagation and electric field orientation of the wave relative to the magnetic field lines. In order to demonstrate that the magnetic field has a negligible effect on the index in the case of the plasma pinch, the electron

cyclotron frequency must first be calculated where

$$\omega_b = eB/m_e . \quad (\text{II.7})$$

The magnetic induction,  $B$ , can be approximated by applying Ampere's law to an infinitely long wire with current  $I_0$ . Then the magnetic induction at the edge of a pinch of radius  $R$  can be approximated by

$$B = \frac{\mu_0 I_0}{2\pi R} . \quad (\text{II.8})$$

The pinch current is typically  $\approx 500$  kA. The corresponding magnetic induction for a pinch radius<sup>3</sup> of 1 mm (maximum compression) is  $B \approx 1$  MGauss. The conditions set an upper limit for the electron cyclotron frequency,  $\omega_b \approx 2 \cdot 10^{13}$ /sec.

A wave propagating parallel to the field lines becomes circularly polarized with either left- or right-hand rotation. The corresponding index of refraction is<sup>6</sup>

$$\mu_{l,r} = \left[ 1 - \frac{\omega_p^2}{\omega(\omega \pm \omega_b)} \right]^{1/2} . \quad (\text{II.9})$$

Since  $\omega_b \ll \omega$ , Equation (II.1) is a good approximation.

If the wave is propagating perpendicular to the magnetic field lines, the field has no effect when the

electric vector of the wave is parallel to it. The equation in this case is simply Equation (II.6). When the electric vector is perpendicular to the magnetic field lines (extraordinary wave), the index of refraction can be written as<sup>6</sup>

$$\mu_{\text{ex}} = \left[ 1 - \frac{\omega_p^2(\omega^2 - \omega_p^2)}{\omega^2(\omega^2 - \omega_p^2 - \omega_b^2)} \right]^{1/2} \quad (\text{II.10})$$

and since  $\omega_b^2 \ll \omega^2 - \omega_p^2$ , Equation (II.1) is also a good approximation for Equation (II.10).

Finally, it is noted that the wave frequency is well away from the upper hybrid frequency defined by

$$\omega_{\text{uh}} \equiv (\omega_b^2 + \omega_p^2)^{1/2} \quad (\text{II.12})$$

## APPENDIX III. INTERFEROMETER ALIGNMENT PROCEDURE

The purpose of this Appendix is to outline the procedure used in alignment of the Mach-Zehnder interferometer of this thesis. Refer to Figures 8, 11 and 13 of Chapter II when following the steps.

1. Align the HeNe laser beam through the center of the two focus chamber windows.
2. Without moving the HeNe laser, align the N<sub>2</sub> laser such that the HeNe beam is concentric within its window and mirror. This assures that the two beams will take the same path.
3. Using the bolts that attach the gimbal mounts to the focus flanges, adjust BS<sub>1</sub> and M<sub>2</sub> to  $\approx 45^\circ$  angles with respect to the HeNe beam such that they are also centered about the beam.
4. The gimbal mount micrometer adjustment screws can now be used to vertically align the HeNe reference and probe beams with reference to a plumb bob. The purpose of the plumb bob is to keep both the reference and probe beams in one plane (not skew).
5. Use the micrometer adjustment screw of M<sub>1</sub> to shift the reference beam horizontally through BS<sub>2</sub> such that it lines up with the probe beam in a vertical plane at the output of BS<sub>2</sub>. Use the other micrometer adjustment screw of M<sub>1</sub> to coextend the

reference beam with the 8" steel channel used in the detection stage.

6. The flange screw is now used to position  $BS_2$  to  $\approx 45^\circ$  with respect to and centered around the HeNe reference beam. The film detector should now be horizontally shifted such that  $HeNe_{ref}$  is centered within the lens and bandpass filter.
7. Adjust  $M_2$  so that the probe beam and the reference beam coincide on the output surface of  $BS_2$ .
8. Adjust  $BS_2$  so that the beams coincide near the pinhole. Fringes in the HeNe beam should occur. Check near the lens.
9. Readjust  $BS_2$  to obtain horizontal and adequately spaced fringes.

The next step involves setting the path difference between the reference and probe waves to zero. Since the nitrogen laser used in this experiment is a single shot device, a photograph must be used after each adjustment of the translational stage until highly visible fringes are observed. It is suggested that the TS be adjusted in 3 full turn increments ( $\approx 1$  mm steps) until highly visible fringes occur around the edges of the fringe pattern. Then the increments should be reduced to 1 turn until the best possible fringes are observed. By further reducing the number of turns to fractional amounts, the quality of fringes



should be as good as seen in the vacuum (no plasma) fringe pattern shown in Figure 9 of Chapter II. After each adjustment of the translational stage, Steps 7 through 9 must be repeated.

## REFERENCES

1. J. P. Rager, "The Plasma Focus," Invited Paper presented at the Int. School of Fusion Reactor Technology, Vth Course on Unconventional Approaches to Fusion, Erice, 16-25 March 1981.
2. F. Venneri, J. Mandrekas, and G. Gerdin, Proc. of the 4th IEEE Inter. Pulsed Power Conf., New Mexico, 350 (1983).
3. F. Venneri, and G. Gerdin, IEEE Int. Conf. on Plasma Sci., St. Louis, MO, 1984, Conf. Record-Abstracts, IEEE Catalog No. 84CH1958-8, 107 (1984).
4. J. Fanning, Ph.D. dissertation, Electrical and Computer Engineering Deptment, University of Illinois, Urbana-Champaign (1986).
5. W. T. Cathey, Optical Information Processing and Holography, (Wiley and Sons, New York, 1974).
6. M. A. Heald and C. B. Wharton, Plasma Diagnostics With Microwaves, (Wiley and Sons, New York, 1965).
7. D. L. Book, NRL Plasma Formulary, Naval Research Laboratory Publication 0084-4040, Revised 1986.
8. H. G. Heard, Nature 200, 667 (1963).
9. G. Gerdin, "Final Report: Opening Switch Research on a Dense Plasma Focus," U.S. Air Force Grant #AFOSR-84-0391, September, 1986.
10. Melles Griot, Catalog, No. 75-29801, (1975).
11. H. Kogelnik and T. Li, Appl. Opt. 5, 1550 (1966).
12. J. Shmoys, J. of Appl. Phys. 22, 689 (1961).
13. F. A. Jenkins, and H. E. White, Fundamentals of Optics, 4th ed., (McGraw-Hill, New York, 1976).
14. M. L. James, G. M. Smith, and J. C. Welford, Applied Numerical Methods for Digital Computation, 2nd ed., (Harper and Row, New York, 1977).
15. W. L. Barr, J. Opt. Soc. of Amer. 52, 885 (1962).

16. P. E. Young, D. P. Neikirk, P. P. Tong, D. B. Rutledge, and N. C. Luhmann, N. C., Rev. Sci. Instrum. 56, 81 (1985).
17. K. Hirano, K. Shimoda, and F. Hamada, Jap. J. of Appl. Phys. 17, 1619 (1978).
18. S. Czekał, S. Denus, A. Kasperczuk, R. Miklaszewski, M. Paduch, T. Pisarczyk, and Z. Wereszczynski, Proc. 4th Intern. Workshop on Plasma Focus and Z-Pinch Research, (Inst. of Plasma Phys. and Microfusion, Warsaw, 1985) 124.
19. V. A. Gribkov, V. M. Korzhavin, O. N. Krokhin, G. V. Sklizkov, N. V. Filippov, and T. I. Filippova, Sov. Phys. JETP Lett. 15, 232 (1972).
20. K. Boulais, G. Gerdin, and F. Venneri, Bult. Amer. Phys. Soc. 31, 1456 (1986).
21. F. Venneri, H. Krompholz, J. Mandrekas, G. Gerdin, and M. Tanis, Bult. Amer. Phys. Soc. 28, 1171 (1983).
22. G. Gerdin, F. Venneri, and K. Boulais, "A Scaling Law for Macroscopic Stability of the Mather-type Plasma Focus," Submitted for Publication to Plasma Phys. and Controlled Fusion (1987).
23. F. L. Curzon, A. Folkierski, R. Latham, and J. A. Nation, Proc. Roy. Soc. (London) A257, 386 (1960).

Approved for Release by NSA on 09-11-2013 pursuant to E.O. 13526

AIR FORCE OFFICE OF SCIENTIFIC RESEARCH (AFSC)  
 APPROVED FOR RELEASE BY NSA TO DTIC

APPROVED FOR RELEASE BY NSA TO DTIC  
 DISSEMINATION AUTHORITY AFR 190-12

MATTHEW J. KERPER

Chief, Technical Information Division

END

DATE

FILMED

DTIC

10-88